

CHAOS IV: Gas-phase Abundance Trends from the First Four CHAOS Galaxies

Danielle A. Berg^{1,2}, Richard W. Pogge^{1,2}, Evan D. Skillman³, Kevin V. Croxall⁴, John Moustakas⁵, Noah S. J. Rogers³, and Jiayi Sun¹

Department of Astronomy, The Ohio State University, 140 W 18th Avenue, Columbus, OH 43210, USA; berg.249@osu.edu
Center for Cosmology & AstroParticle Physics, The Ohio State University, 191 West Woodruff Avenue, Columbus, OH 43210, USA
Minnesota Institute for Astrophysics, University of Minnesota, 116 Church Street SE, Minneapolis, MN 55455, USA
Expeed Software, 100 W Old Wilson Bridge Road Suite 216, Worthington, OH 43085, USA
Department of Physics & Astronomy, Siena College, 515 Loudon Road, Loudonville, NY 12211, USA
Received 2019 September 25; revised 2020 January 1; accepted 2020 January 14; published 2020 April 20

Abstract

The chemical abundances of spiral galaxies, as probed by H II regions across their disks, are key to understanding the evolution of galaxies over a wide range of environments. We present Large Binocular Telescope/Multi-Object Double Spectrographs spectra of 52 H II regions in NGC 3184 as part of the CHemical Abundances Of Spirals (CHAOS) project. We explore the direct-method gas-phase abundance trends for the first four CHAOS galaxies, using temperature measurements from one or more auroral-line detections in 190 individual H II regions. We find that the dispersion in $T_e - T_e$ relationships is dependent on ionization, as characterized by $F_{\lambda 5007}/F_{\lambda 3727}$, and so we recommend ionization-based temperature priorities for abundance calculations. We confirm our previous results that [N II] and [S III] provide the most robust measures of electron temperature in low-ionization zones, while [O III] provides reliable electron temperatures in high-ionization nebula. We measure relative and absolute abundances for O, N, S, Ar, and Ne. The four CHAOS galaxies marginally conform with a universal O/H gradient, as found by empirical integral field unit studies when plotted relative to effective radius. However, after adjusting for vertical offsets, we find a tight universal N/O gradient of $\alpha_{\rm N/O} = -0.33~{\rm dex}/R_e$ with $\sigma_{\rm tot.} = 0.08$ for $R_g/R_e < 2.0$, where N is dominated by secondary production. Despite this tight universal N/O gradient, the scatter in the N/O-O/H relationship is significant. Interestingly, the scatter is similar when N/O is plotted relative to O/H or S/H. The observable ionic states of S probe lower ionization and excitation energies than O, which might be more appropriate for characterizing abundances in metal-rich H II regions.

Unified Astronomy Thesaurus concepts: Chemical abundances (224); Galaxy abundances (574); Interstellar abundances (832); Metallicity (1031); Spiral galaxies (1560); Galaxy chemical evolution (580); Galaxy evolution (594); Interstellar medium (847)

Supporting material: machine-readable tables

1. Introduction

The history of a galaxy can be traced by the abundances of heavy elements, as they are produced and accumulated as successive generations of stars return their newly synthesized elements to the interstellar medium (ISM). In spiral galaxies, ISM abundance studies are dominated by the disk, where the majority of their star formation occurs, and are typically characterized by negative radial gradients of oxygen and nitrogen abundances (e.g., Pagel & Edmunds 1981; Garnett & Shields 1987; Zaritsky & Kennicutt 1994). The abundance gradients across the disks of spiral galaxies provide essential observational constraints for chemical evolution models of galaxies and support the inside-out growth theory of galaxy disk formation.

Emission lines originating from H II regions provide an excellent probe of the gas-phase abundances and, thus, the radial metallicity gradients in disk galaxies. Further, H II regions, which are ionized by recently formed massive stars that carry the same chemical signature from the gas in which they were formed, allow us to measure the cumulative chemical evolution of the present-day ISM.

Galaxy surveys conducted with integral field unit (IFU) spectrographs are spatially resolving large numbers of low-redshift galaxies (e.g., Sánchez et al. 2012; Bryant et al. 2015; Bundy et al. 2015), and intermediate-redshift galaxies are being targeted using ground-based infrared spectrographs (e.g.,

 $z\sim2-3$ lensed or stacked galaxies; Erb et al. 2010; Steidel et al. 2014; Rigby et al. 2015; Shapley et al. 2015; Berg et al. 2018). In the future, these studies will enable us to answer important questions that impact our understanding of galaxy formation and evolution, such as the importance of metallicity gradients over cosmic time, the magnitude of azimuthal variations, and integrated light versus resolved studies. However, presently, most of these studies must use abundance correlations with strong emission lines to interpret their data (strong-line methods) and so are inherently limited by the large uncertainties associated with the calibrations of these methods (up to 0.7 dex in absolute abundance; Kewley & Ellison 2008; Moustakas et al. 2010). Until we can truly understand the abundances of the local spiral galaxies and improve our calibration toolset, we cannot be completely confident in our measures from IFU studies or of the chemical evolution of galaxies at high redshift.

Many studies have used multi-object spectroscopy to attempt to directly measure the nebular physical conditions and abundances and map out their trends across the disks of spiral galaxies. However, because direct measurements of gas-phase abundances via one of the "direct" methods (i.e., auroral or recombination lines) have long been prohibitively expensive in terms of telescope time, the majority of these studies are limited to first-order trends using a dozen or fewer abundance detections per galaxy. This challenge motivated the CHemical

Abundances Of Spirals (CHAOS; Berg et al. 2015) project: a large database of high-quality H II region spectra over a large range in abundances and physical conditions in nearby spiral galaxies. These spectra provide direct abundances and estimates of temperature stratification and their corresponding corrections to lower absolute abundances, and they allow for calibrations based on observed abundances over expanded parameter space rather than photoionization models.

While the absolute abundance scale of H II regions is still a topic of debate (see, for example, the discussion of the Abundance Discrepancy Factor in Bresolin et al. 2016), the CHAOS survey is building a large sample of direct abundances, observed and analyzed uniformly, allowing us to characterize the possible systematics of the direct method. To date, CHAOS has increased, by more than an order-ofmagnitude, the number of HII regions with high-quality spectrophotometry to facilitate the first detailed direct measurements of the chemical abundances in a sample of nearby disk galaxies. So far, results for individual galaxies have been reported for NGC 628 (M74) in Berg et al. (2015, hereafter, B15), NGC 5194 (M51a) in Croxall et al. (2015, hereafter, C15), and NGC 5457 (M101) in Croxall et al. (2016, hereafter, C16). Here, we present new direct abundances for NGC 3184 and, combined with past results, present the first analyses of a sample of four CHAOS galaxies, totaling 190 H II regions with measured auroral-line-based temperatures.

The paper is organized as follows. In Section 2, we briefly review the CHAOS data, including the spectroscopic observations (Section 2.1), reductions (Section 2.2), and emission-line measurements (Section 2.3). Section 3 details the nebular electron temperature and density measurements, recommended ionization-based temperature priorities, as well as the abundance determinations. Radial abundance trends for the first four CHAOS galaxies are reported in Section 4, beginning with radial O/H and S/H abundances in Sections 4.1 and 4.2, respectively. In Section 4.3, we propose a universal secondary N/O gradient. We discuss secondary drivers of the observed abundance trends in Section 5, namely azimuthal variations (Section 5.1), surface-density relationships (Section 5.2), and effective yields (Section 5.3). Section 6 examines abundance trends with metallicity for the CHAOS sample, where α/O and N/O trends are discussed in Sections 6.1 and 6.2, respectively. Finally, we focus on N/O trends in Section 7. We discuss the production of N/O in spiral galaxies in Section 7.1 and consider sources of scatter in the N/O-O/H relationship in Section 7.2. A summary of our results is provided in Section 8.

2. New CHAOS Spectroscopic Observations of NGC 3184

2.1. Optical Spectroscopy

All CHAOS observations are obtained following a consistent methodology, but here we highlight details specific to new observations of NGC 3184. Optical spectra of NGC 3184 were obtained during 2012 March and 2013 January using the Multi-Object Double Spectrographs (MODS; Pogge et al. 2010) on the Large Binocular Telescope (LBT). The spectra were acquired with the MODS1 unit as the MODS2 spectrograph was not available at the time of the observations. We obtained simultaneous blue and red spectra using the G400L (400 lines mm⁻¹, $R \approx 1850$) and G670L (250 lines mm⁻¹, $R \approx 2300$) gratings, respectively. This setup provided broad spectral coverage extending from 3200 to 10,000 Å. Multiple fields were targeted in order to maximize the

number of H II regions with auroral-line detections, i.e., [S II] $\lambda\lambda4068,4076,$ [O III] $\lambda4363,$ [N II] $\lambda5755,$ [S III] $\lambda6312,$ and [O II] $\lambda\lambda7320,7330.$ Individual field masks, cut to target 17–25 H II regions simultaneously, were observed for six exposures of 1200 s, or a total integration time of 2 hr per field.

Targeted H II regions in NGC 3184, as well as alignment stars, were selected based on archival broadband and H α imaging from the SINGS program (Kennicutt et al. 2003a; Muñoz-Mateos et al. 2009). Slits were cut to be 1" wide by a minimum of \sim 10" long, to cover the extent of individual H II regions, and extended to utilize extra space for the sky. Slits were placed on relatively bright H II regions across the entirety of the disk with the goal of ensuring that both radial and azimuthal trends in the abundances could be investigated. The locations of the slits for each of the three MODS fields observed in NGC 3184 are shown in Figure 1.

We refer to the locations of the observed H II regions in NGC 3184 as offsets, in R.A. and decl., from the center of the galaxy (see Table A1 in Appendix A). The observations were obtained at relatively low airmass (\lesssim 1.2). Furthermore, slits were cut close to the median parallactic angle of the observing window for NGC 3184. The combination of low airmass and matching the parallactic angle minimizes flux lost due to differential atmospheric refraction between 3200 and 10,000 Å (Filippenko 1982).

We report the new observations of NGC 3184 in Appendix A, while details of previously reported observations can be found in B15 for NGC 628, C15 for NGC 5194, and C16 for NGC 5457. The adopted properties of these four galaxies are listed in Table 1. Note that for NGC 628, NGC 5194, and NGC 5457, we report properties of these galaxies as adopted by the original CHAOS studies. It may be of interest to some readers that since the time of the previous CHAOS studies, updated (and likely more accurate) distances have been measured for NGC 628 and NGC 5194 by McQuinn et al. (2017) and for NGC 5457 by Jang & Lee (2017) using the tip of the red giant branch method. While many absolute properties change with galaxy distance, the results presented here are concerned only with relative abundance trends versus R_e or R_{25} , and so they are not affected by the updated distances.

2.2. Spectral Reductions

For a detailed description of the data reduction procedures, we refer the reader to B15. Here, we only note the primary points of our data processing. Spectra were reduced and analyzed using the beta-version of the MODS reduction pipeline⁶, which runs within the XIDL⁷ reduction package. Given that the bright disks of CHAOS galaxies can complicate local sky subtraction, additional sky slits were cut in each mask that provided a basis for clean sky subtraction. Continuum subtraction was performed in each slit by scaling the continuum flux from the sky-slit to the local background continuum level. One-dimensional spectra were then corrected for atmospheric extinction and flux calibrated based on observations of flux-standard stars (Bohlin 2014). At least one flux standard was observed on each night science data were obtained. An example of a flux-calibrated spectrum is shown in Figure 2.

⁶ http://www.astronomy.ohio-state.edu/MODS/Software/modsIDL/

http://www.ucolick.org/~xavier/IDL/

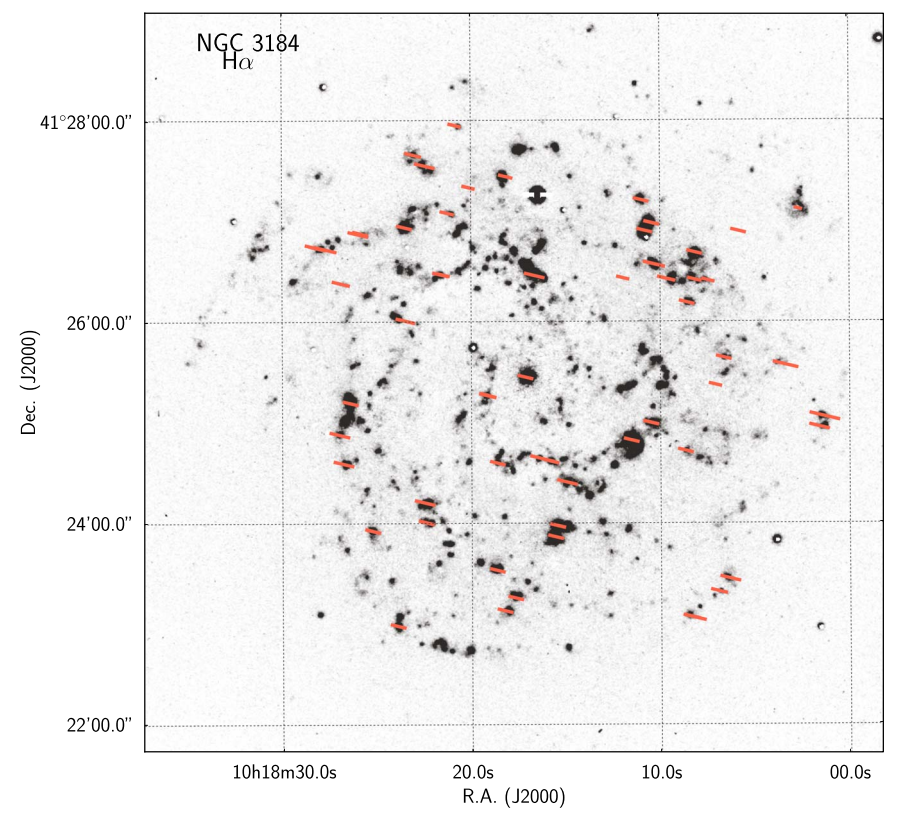


Figure 1. Continuum-subtracted H α SINGS image of NGC 3184 (Muñoz-Mateos et al. 2009). The footprints of CHAOS slits are overlaid in light red, representing the Field 1, 2, and 3 slit positions observed at the LBT. The slit positions targeted H II regions, although not always centered in order to maximize effective usage of mask real estate and obtain background within the slit. See Table 2 for more details.

2.3. Emission-line Measurements

We provide a more detailed description of the adopted continuum modeling and line-fitting procedures applied to the CHAOS observations in B15. Below, we only highlight the fundamental components of this process. We model the underlying continuum of our MODS1 spectra using the STARLIGHT⁸ spectral synthesis code (Fernandes et al. 2005) in conjunction with the models of Bruzual & Charlot (2003). Allowing for an additional nebular continuum, we fit each emission line with a Gaussian profile. We note that we have modeled blended lines (H7, H8, and H11–H14) in the Balmer series based on the measurements of unblended Balmer lines and the tabulated atomic ratios of Hummer & Storey (1987), assuming Case B recombination.

We correct the strength of emission features for line-of-sight reddening using the relative intensities of the four strongest Balmer lines ($\text{H}\alpha/\text{H}\beta$, $\text{H}\gamma/\text{H}\beta$, $\text{H}\delta/\text{H}\beta$). We report the determined values of E(B-V) in Table A2 of Appendix A. We do not apply an ad hoc correction to account for Balmer absorption as the lines were fit simultaneously with the stellar population models. The stellar models contain stellar absorption with an equivalent width of $\approx 1-2\,\text{Å}$ in the $\text{H}\beta$ line. The uncertainty associated with each measurement is determined from measurements of the spectral variance, extracted from the two-dimensional variance image, uncertainty associated with the flux calibration, Poisson noise in the continuum, read noise,

sky noise, flat-fielding calibration error, error in continuum placement, and error in the determination of the reddening. We also include a 2% uncertainty based on the precision of the adopted flux calibration standards (Oke 1990, see discussion in Berg et al. 2015).

A few emission features required extra care, such as the intrinsically faint auroral lines that are critical to this study. As has been done with the previous CHAOS galaxies, we inspected the lines by eye and measured the flux of each auroral line by hand in the extracted spectra to confirm the fit. In cases where these measurements were in disagreement, we adopted the by-hand measurement. This was most common for the [N II] $\lambda 5755$ line, which falls near the wavelength region affected by the dichroic cutoff of MODS and the "red bump" Wolf–Rayet carbon features. Additionally, we have updated our line-fitting code to include the [Fe II] $\lambda 4360$ emission feature, which may significantly contaminate [O III] $\lambda 4363$ line measurements at high metallicities $(12 + \log(O/H) > 8.4$; Curti et al. 2017).

Finally, the [O II] $\lambda\lambda 3726,3729$ doublet is blended for all observations due to the moderate resolution of MODS. However, two components are apparent in the doublet profile for the majority of spectra and are therefore modeled using two Gaussian profiles. The reported [O II] $\lambda 3727$ fluxes represent the total flux in the doublet.

The reddening-corrected emission-line intensities measured from H II regions in NGC 628, NGC 5194, and NGC 5457 have been previously reported in B15, C15, and C16, respectively. For the NGC 3184 observations reported here, the reddening-corrected line intensities are listed in Table A2 of Appendix A.

⁸ www.starlight.ufsc.br

⁹ We note that previous CHAOS papers also report the E(B-V) reddening but had incorrectly labeled this quantity as $c(H\beta)$.

Table 1
Adopted Properties of CHAOS Galaxies

Property	NGC 628	NGC 5194	NGC 5457	NGC 3184
R.A.	01:36:41.75	13:29:52.71	14:03:12.5	10:18:16.86
Decl.	15:47:01.18	47:11:42.62	54:20:56	41:25:26.59
Type	SA(s)c	SA(s)bc pec	SAB(rs)cd	SAB(rs)cd
Redshift	0.00219	0.00154	0.00080	0.00198
Adopted	7.2^{1}	7.9^{2}	7.4^{3}	11.7^{4}
D (Mpc)				
Inclination	5 ⁵	22^{6}	18^{7}	16^{8}
(deg.)				
P.A. (deg.)	12 ⁹	172 ⁷	39^{7}	179 ⁸
m_B (mag)	10.01	9.08	7.99	10.44
$\log M_{\star}(M_{\odot})$	10.0	10.5	10.4	10.2
$v_{\text{flat}} (\text{km s}^{-1})$	200	210	210	200
R_{25} (arcsec)	315.0^{9}	336.6^{9}	864.0^{10}	222.0^{9}
CHAOS-Derived	l Properties:			
R_e (arcsec)	95.4	94.7	197.6	93.2
R_{ϱ} Coverage	2.3	3.4	4.6	2.0
(R_e)				
T_e Regions ^a	45 ¹¹	2812	72 ¹³	30^{14}

Note. Adopted properties for the current sample of CHAOS galaxies: NGC 628, NGC 5194, NGC 5457, and NGC 3184. Rows 1 and 2 give the R.A. and decl. of the optical center in units of hours, minutes, seconds, and degrees, arcminutes, arcseconds, respectively. The R.A.s, decls., galaxy type (Row 3), and redshifts (Row 4) are taken from the NASA/IPAC Extragalactic Database (NED). Adopted distances, inclinations, and position angles are given in Rows 5-7. Rows 8-10 list B-band magnitude (de Vaucouleurs et al. 1991), stellar mass, and v_{flat} of each galaxy. Stellar masses were determined using the integrated 3.6 μ m flux in Dale (2009) and rotation speed is adopted from the simple flat rotation curve reported in Leroy et al. (2013). Rows 11 and 12 give the optical radius at the B_{25} mag arcsec⁻² and the half-light radius, as determined in this work (see Appendix A for details), of the system in arcseconds, respectively. Row 13 provides the radial coverage of the CHAOS observations in units of Re. Finally, the number of H II regions with direct auroral-line temperature measurements from [O III], [N II], or [S III] are tabulated in Row 14.

References. (1) Van Dyk et al. (2006), (2) Baron et al. (2007), (3) Ferrarese et al. (2000), (4) Bose & Kumar (2014), (5) Shostak & van der Kruit (1984), (6) Colombo et al. (2014), (7) Walter et al. (2008), (8) Jiménez-Donaire et al. (2017), (9) Egusa et al. (2009), (10) Kennicutt et al. (2003a), (11) B15, (12) C15, (13) C16, (14) this work.

3. Direct Gas-phase Abundances

3.1. Electron Temperature and Density Determinations

The combined sensitivity and large wavelength coverage of CHAOS observations allows electron temperature and density measurements from multiple ions. The temperature-sensitive auroral-to-nebular line ratios most commonly observed in the CHAOS spectra are [S II] $\lambda\lambda4068,4076/\lambda\lambda6717,6731$; [O III] $\lambda 4363/\lambda \lambda 4959,5007;$ [N II] $\lambda 5755/\lambda \lambda 6548,6584;$ [S III] $\lambda 6312/\lambda \lambda 9069$, 9532; and [O II] $\lambda \lambda 7320,7330/\lambda \lambda 3727,3729$. To account for possible contamination by atmospheric absorption of the red [S III] lines, we follow our practice in B15 of upward correcting the weaker of the two lines by the theoretical ratio of $\lambda 9532/\lambda 9069 = 2.47$. Assuming a threezone ionization structure, these measurements probe the physical conditions throughout the nebula, and allow for the comparison of multiple measures in the low-ionization zone. We use the ratio of the [S II] $\lambda\lambda6717,6731$ emission lines as a sensitive probe of the nebular electron density in typical HII regions $(10^{1.5} < n_e (\text{cm}^{-3}) < 10^{3.5})$. In order to compare the

first four CHAOS galaxies in a uniform, consistent manner, we recalculate the nebular temperatures and densities adopting the atomic data reported in Table 4 of B15 and using the observed temperature- and density-sensitive line ratios with the PYNEB package in PYTHON (Luridiana et al. 2012, 2015).

3.1.1. Temperature Relationships

It is common practice to use temperature–temperature $(T_e - T_e)$ relationships derived from photoionization models to infer the temperatures in unobserved ionization zones. The relationships of Garnett (1992, hereafter, G92) are a typical choice; however, significant updates in atomic data (especially for [S III] and [O II]; see Figure 4 in B15) have occurred since the time of that work and so new relationships are warranted.

In C16, we obtained temperature measurements from one or more auroral lines in 74 H II regions in M101, the largest number in a single galaxy to date. These data used the updated atomic data recommended in B15 and provided a large data set of well-measured temperatures from multiple ions that allowed us to empirically determine new $T_e - T_e$ relationships:

$$T_e[N II] = (0.714 \pm 0.142) \times T_e[O III] + (2.57 \pm 1.25),$$

$$(1)$$

$$T_e[S III] = (1.312 \pm 0.075) \times T_e[N II] - (3.13 \pm 0.58),$$

$$(2)$$

$$T_e[S III] = (1.265 \pm 0.140) \times T_e[O III] - (2.32 \pm 1.35),$$

$$(3)$$

where temperatures are in units of 10^4 K.

Using the combined data from the first four CHAOS galaxies, we compile a sample of 190 individual H II regions with multiple auroral-line measurements. Of these regions, 175 have $T_e[{\rm O\,III}]$, $T_e[{\rm S\,III}]$, or $T_e[{\rm N\,II}]$. In Figure 3, we compare these data to the T_e-T_e relationships of G92 (red dotted-dashed lines) and C16 (black dashed lines). For reference, the line of equality is shown as a dotted black line. We recognize that these are simple T_e-T_e relationships; in the future, we will use the full CHAOS data set to explore more complicated T_e-T_e relationships, for example, accounting for the effects of ionization discussed below.

For each set of variables, we determine the best-fit $T_e - T_e$ relationship using a Bayesian linear regression. Specifically, we use the code python LINMIX, 10 which is an implementation of the linear mixture model algorithm developed by Kelly (2007) to fit data with uncertainties on two variables, including explicit treatment of intrinsic scatter. Intrinsic scatter, $\sigma_{\rm int.}$, is due to real deviations in the physical properties of our sources that are not completely captured by the variables considered. By introducing an additional term representing the intrinsic scatter to the weighting of each data point in the fit, we can determine the median of the normally distributed intrinsic random scatter about the regression. The calculated total and intrinsic scatters, $\sigma_{\rm tot.}$ and $\sigma_{\rm int.}$ respectively, as well as the number of regions used in the fit, are presented in Figure 3.

The top two panels of Figure 3 compare temperature measurements that characterize the low-ionization zone. On the left, we use the 115 regions with both [N II] and [O II] measurements in our sample, and find a best fit of T_e [N II] = $[T_e$ [O II] $-(1.203 \pm 1.144)]/(1.004 \pm 0.150)$. As expected, the overall trend follows a one-to-one relationship within the limits

^a Only regions with $T_e[O III]$, $T_e[S III]$, or $T_e[N II]$ are tallied here.

¹⁰ https://github.com/jmeyers314/linmix

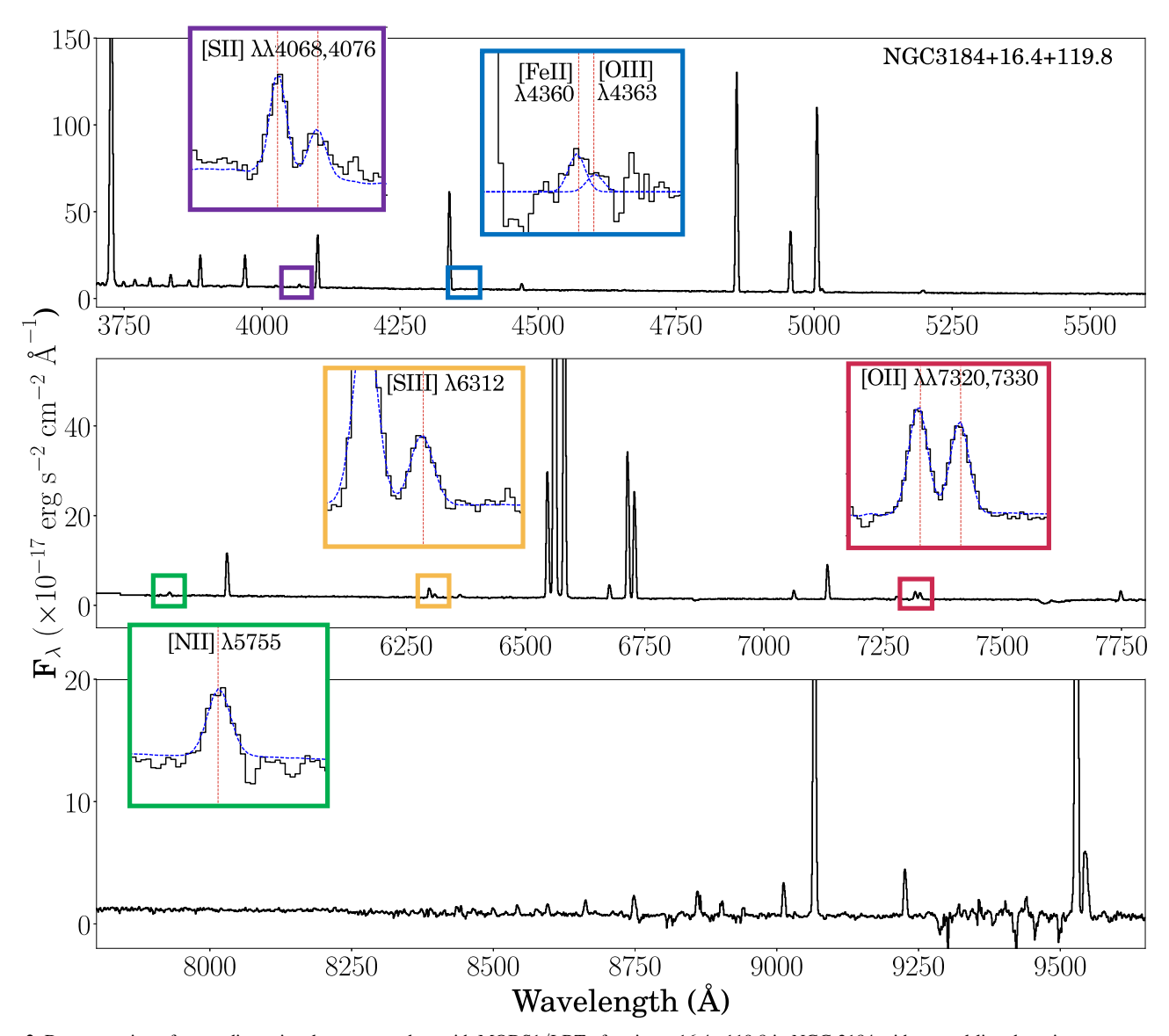


Figure 2. Demonstration of a one-dimensional spectrum taken with MODS1/LBT of region +16.4+119.8 in NGC 3184 with auroral-line detections at a strength of 3σ or greater. The observed spectrum is plotted as a black line, with the model in blue. In the expanded windows, we mark and label the five temperature-sensitive auroral emission-line features used in this paper: [S II] $\lambda\lambda4068,4076$ [O III] $\lambda4636$, [N II] $\lambda5755$, [S III] $\lambda6312$, and [O II] $\lambda\lambda7320,7330$. This spectrum lacks an [O III] $\lambda4363$ detection as the majority of the emission in that region is actually due to a contaminating [Fe II] line at $\lambda4360$ (see blue box). Note that major telluric absorption features are not corrected for (see bottom panel).

of the uncertainties but with both large total ($\sigma_{\rm tot.}=1280~{\rm K}$) and intrinsic ($\sigma_{\rm int.}=1150~{\rm K}$) scatters. While equal temperatures are expected from photoionization models, the data tend to be shifted toward higher $T_e[{\rm O~II}]$. This is true for the majority of the sample, which is clustered within $1000-2000~{\rm K}$ of the equality relationship, but especially for the more extreme outliers that offset up to roughly $5000~{\rm K}$.

We note that dielectronic recombination can contribute to the observed [O II] emission, especially $\lambda\lambda7320,7330$, in more metal-rich nebulae (e.g., Rubin 1986). The magnitude of the effect increases strongly with decreasing temperature (increasing metallicity) but depends on the electron density. To this end, Liu et al. (2001) showed that recombination can play an important role in exciting both the [O II] $\lambda\lambda7320,7330$ and [N II] $\lambda5754$ auroral lines in the higher-density gas of planetary nebulae (>10 3 cm⁻³). These authors showed that this effect leads to overestimated [O II]- and [N II]-derived electron temperature measurements. However, we show below that

 $T_e[{\rm N~II}]$ is well behaved with respect to $T_e[{\rm S~III}]$, which implies that the recombination contribution must be small at the low densities of our nebulae. Thus, our data are consistent with previous reports of systematically larger $T_e[{\rm O~II}]$ than $T_e[{\rm N~II}]$ measurements (e.g., Esteban et al. 2009; Pilyugin et al. 2009; Berg et al. 2015) that cannot be accounted for by recombination processes, and so we do not favor $[{\rm O~II}]$ as a reliable low-ionization zone temperature indicator. We reserve further analysis for the complete CHAOS sample, where we will revisit the reliability of $[{\rm O~II}]$ as a diagnostic and investigate the effects of sky contamination, recombination, and reddening.

In the top right panel of Figure 3, we compare [N II] and [S II] using the [S II] temperatures presented in C16, plus newly derived values for NGC 628, NGC 5194, and NGC 3184, comprising a sample of 106 regions. As expected for two ions that probe similar low-ionization gas, the best fit is consistent with equality as $T_e[N II] = [T_e[S II] - (0.072 \pm 1.392)]/(1.101 \pm 0.180)$. Again, the intrinsic scatter accounts for the majority of the total scatter;

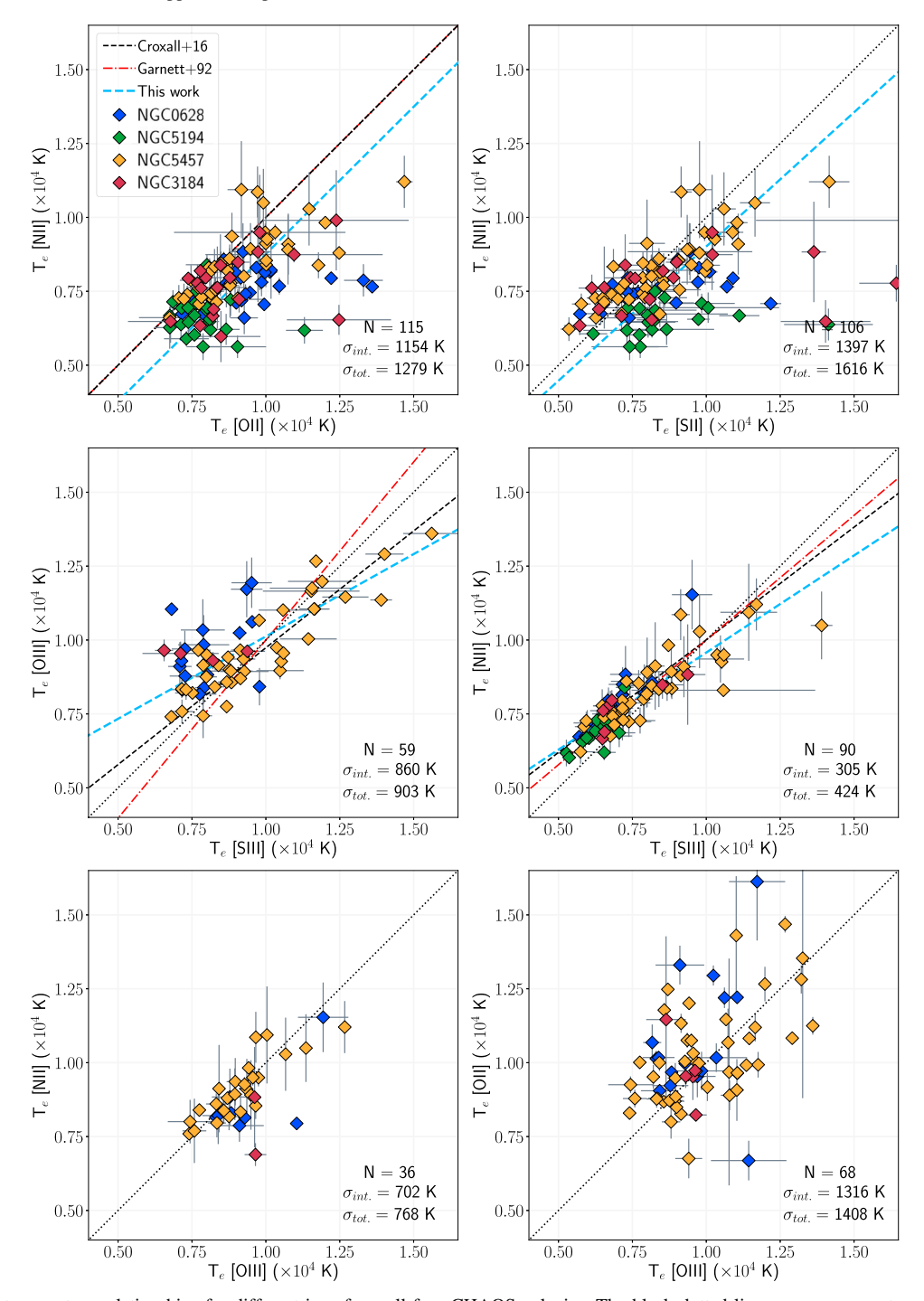


Figure 3. Comparing temperature relationships for different ions from all four CHAOS galaxies. The black dotted lines assume a one-to-one relationship, the red dotted—dashed lines are the photoionization model relationships from Garnett (1992), the black dashed lines are the updated empirical relationships from C16, and the blue dashed lines are the best linear fits to the data from all four CHAOS galaxies. The top panels compare measures of the low-ionization zone temperatures. Top left panel: $T_e[N \text{ II}]$ vs. $T_e[O \text{ II}]$, showing large scatter. Top right panel: $T_e[N \text{ II}]$ vs. $T_e[S \text{ II}]$, offset significantly from one-to-one. The middle panels compare to the intermediate-ionization temperature, $T_e[S \text{ III}]$, revealing the scattered $T_e[O \text{ III}]$ vs. $T_e[S \text{ III}]$ trend (left panel) and the tight correlation between $T_e[N \text{ II}]$ and $T_e[S \text{ III}]$ (right panel). The bottom panels show further comparisons to the high-ionization temperature, $T_e[O \text{ III}]$. The $T_e[N \text{ II}]$ vs. $T_e[O \text{ III}]$ trend (left panel) is relatively well behaved but has few points, whereas $T_e[O \text{ III}]$ vs. $T_e[O \text{ III}]$ (right) is a scatter plot. We adopt the C16 relationships, given in Equations (1)–(3) for this work.

however, the large deviations observed indicate that observational uncertainties still play a large role at high $[S\ II]$ temperatures.

In the middle two panels of Figure 3, we examine the relationship between the intermediate-ionization zone, characterized by [S III], with both the high-ionization zone ([O III]; left panel) and low-ionization zone ([N II]; right panel). In the middle left panel, we find that the best fit to the $T_e[O III] - T_e[S III]$

relationship is in good agreement with C16 but diverges from G92 for the hottest regions observed: $T_e[\text{S III}] = (1.795 \pm 0.067) \times T_e[\text{O III}] - (8.167 \pm 1.122)$. Previous studies have reported large discrepancies between $T_e[\text{O III}]$ and $T_e[\text{S III}]$ and significant scatter in their relationship (e.g., Hägele et al. 2006; Pérez-Montero et al. 2006; Binette et al. 2012; Berg et al. 2015). The $T_e[\text{O III}] - T_e[\text{S III}]$ relationship for our sample of 59

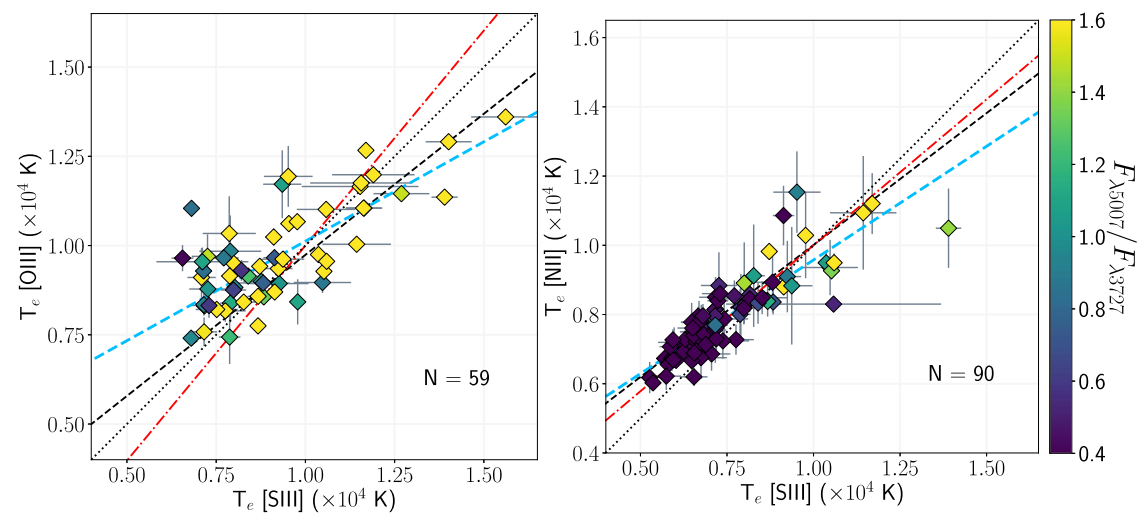


Figure 4. T_e [O III] vs. T_e [S III] (left panel) and T_e [N II] vs. T_e [S III] (right panel) for all four CHAOS galaxies color-coded by the reddening-corrected [O III] λ 5007/[O II] λ 3727 flux ratios. The tight correlation between T_e [N II] and T_e [S III] seen for the dark blue / purple points promotes the use of these low- and intermediate-ionization zone temperatures for low-ionization H II regions (low $F_{\lambda5007}/F_{\lambda3727}$). However, comparing the high-ionization yellow points in the two plots suggests it is better to use the high-ionization zone temperature, T_e [O III], for H II regions with high $F_{\lambda5007}/F_{\lambda3727}$.

regions is no exception, with a significant scatter of $\sigma_{\rm tot.} = 900$ K that can be attributed almost entirely to intrinsic scatter ($\sigma_{\rm int.} = 860$ K). Given the large number of outliers presented in both our sample and the literature, we reiterate and stress the finding of B15 that $T_e[{\rm O\,III}]$ alone is less reliable than $T_e[{\rm S\,III}]$ or $T_e[{\rm N\,II}]$ for abundance calculations in metal-rich H II regions.

Curti et al. (2017) cautioned of the potential contamination of the temperature-sensitive [O III] $\lambda 4363$ line by the neighboring [Fe II] $\lambda 4360$ line. This effect is especially prominent at abundances of $12 + \log(O/H) > 8.4$, where the [Fe II] line increases in strength and the [O III] $\lambda 4363$ line becomes faint due to the decreasing H II region temperature. Because Curti et al. (2017) used stacks of integrated galaxy light spectra in their study, the source of the [Fe II] $\lambda 4360$ emission is difficult to trace; however, as a precaution, we have added the Fe II emission feature to our line-fitting code so that the [Fe II] $\lambda 4360$ and [O III] $\lambda 4363$ lines are simultaneously fit and deblended, and we have inspected the fits by eye (see Section 2.2). In fact, we do not measure $T_e[O III]$ in any very metal-rich H II regions in CHAOS and so do not find any significant [Fe II] contamination affecting our $T_e[O III]$ measurements. For instance, [Fe II] $\lambda 4360$ emission is seen in the blue inset window of the spectrum shown in Figure 2. However, [O III] $\lambda 4363$ was not strong enough to be identified as a detection and so the high-ionization zone temperature was inferred from $T_e[S III]$ and not affected by the [Fe II] contamination.

In the middle right panel of Figure 3, we plot $T_e[{\rm N\,II}]$ versus $T_e[{\rm S\,III}]$. Similar to the trend reported in B15, we find a very tight correlation, especially for the coolest, most metal-rich regions typical of CHAOS (with $T_e < 10^4\,{\rm K}$). The best-fit line (blue) to the 90 regions is $T_e[{\rm S\,III}] = (1.522 \pm 0.042) \times T_e[{\rm N\,II}] - (4.576 \pm 0.463)$, in agreement with the relationship of C16 (black dashed line) and about which the dispersion is quite small: $\sigma_{\rm tot.} = 420\,{\rm K}$. The C16 relationship is also very similar to the G92 relationship, where differences (seen in both bottom panels) are likely due to changes in the adopted [S\,III] atomic data.

Finally, we compare the low- and high-ionization zones in the bottom two panels of Figure 3. On the left, the relationship between the low-ionization zone $T_e[{\rm N\,II}]$ and the high-ionization zone $T_e[{\rm O\,III}]$ is reasonably well behaved, but it has too few data points to analyze further. On the other hand, the $T_e[{\rm O\,III}]$ - $T_e[{\rm O\,III}]$ plot shows a cloud of scattered points that is difficult to characterize.

Significant [O III] $\lambda4363$, [N II] $\lambda5755$, and/or [S III] $\lambda6312$ detections are measured in 30 regions in NGC 3184, resulting in direct oxygen abundance measurements. The electron temperatures and densities characterizing each H II region observed in NGC 3184 are reported in Table A3 in Appendix A.

3.1.2. Ionization-based Temperature Priorities

CHAOS has proven highly successful at measuring significant detections of both [N II] $\lambda 5755$ and [S III] $\lambda 6312$, demonstrating the utility of these lines in metal-rich H II regions. Given the robust $T_e[\text{N II}] - T_e[\text{S III}]$ relationship demonstrated for the 90 H II regions with simultaneous detections, our results further endorse the recommendation of B15 to prioritize these two temperature indicators. However, it is interesting that the $T_e[\text{N II}] - T_e[\text{S III}]$ relation shows a notable increase in dispersion for $T_e > 10^4 \, \text{K}$, whereas the dispersion in the $T_e[\text{O III}] - T_e[\text{S III}]$ relationship seems to settle down in that same T_e regime.

Recently, Yates et al. (2020) measured a large range of $T_e[O\ III]/T_e[O\ II]$ ratios spanning significant temperature (and, due to its inverse dependence, metallicity) parameter space from a sample of 130 H II regions and integrated-light galaxies. They postulate that deviations from equal temperatures are rooted in the ionization structure of the nebulae, where O^{++} -dominated nebulae have cooler [O III] temperatures and O^+ -dominated nebulae have cooler [O III] temperatures. Because the relative flux of the [O III] $\lambda 5007$ and [O II] $\lambda 3727$ emission lines is dependent on the number of oxygen ions in the O^{++} relative to O^+ state, we can use the [O III] $\lambda 5007/[O\ II]$ $\lambda 3727$ ratio as a proxy for O^{++}/O^+ or the ionization structure.

In Figure 4, we reproduce the $T_e[O III] - T_e[S III]$ and $T_e[N II] - T_e[S III]$ relationships from Figure 3 but with the

Ionization-Based Temperature Priorities:

		— Ionization Zone: –	
Criteria:	Low	Intermediate	High
O ₃₂ > _ 1.25	1. T _e [NII] 2. T _e [SIII] + Eqn. 2 3. T _e [OIII] + Eqn. 1	1. T _e [SIII] 2. T _e [OIII] + Eqn. 3 3. T _e [NII] + Eqn. 2	1. T _e [OIII] 2. T _e [SIII] + Eqn. 3 3. T _e [NII] + Eqn. 1
O ₃₂ < _	 T_e[NII] T_e[SIII] + Eqn. 2 T_e[OIII] + Eqn. 1 	1. T _e [SIII] 2. T _e [NII] + Eqn. 2 3. T _e [OIII] + Eqn. 3	1. T _e [SIII] + Eqn. 3 2. T _e [NII] + Eqn. 1 3. T _e [OIII]

Figure 5. Updated temperature prioritization for different ionization zones from the CHAOS data. The priorities are to be used to select the first measured ion temperature from each ordered list and are split into two separate decision trees based on the $O_{32} = F_{\lambda 5007}/F_{\lambda 3727}$ ratio, which is used to determine the average ionization of an H II region.

points color-coded by their reddening-corrected [O III] $\lambda 5007/$ [O II] $\lambda 3727$ flux ratios. As expected, low-ionization H II regions (low $F_{\lambda 5007}/F_{\lambda 3727}$; dark blue/purple points) show the tightest correlation between the low- and intermediate-ionization zone temperatures (T_e [N II] versus T_e [S III]) and high-ionization H II regions (high $F_{\lambda 5007}/F_{\lambda 3727}$; yellow points) show the tightest correlation between high- and intermediate-ionization zone temperatures (T_e [O III] versus T_e [S III]). Motivated by these dispersion-ionization correlations, we recommend simple, yet improved, ionization-based temperature priorities below.

While few $T_e[O III]$ detections were found in the first CHAOS paper examining NGC 628, many more detections were added with the addition of NGC 5457, revealing the utility of $T_e[O III]$ at high T_e and high ionization (high $F_{\lambda 5007}/F_{\lambda 3727}$). Therefore, we prefer a $T_e[O\ III]$ measurement for high-ionization nebulae that are dominated by the O⁺⁺ zone and a $T_e[N II]$ measurement for low-ionization nebulae that are predominantly O^+ , where $T_{\rho}[S III]$ is used in the absence of a [N II] $\lambda 5755$ detection. In order to apply this rubric, we define a high- (low-) ionization nebula criterion of $F_{\lambda 5007}/F_{\lambda 3727} > (<)$ 1.25. This division was chosen based on a statistical analysis of the $T_e[{\rm O\,III}]$ -based oxygen abundance dispersion with $F_{\lambda 5007}/F_{\lambda 3727}$ using data from the C16 study of M101 and the Rosolowsky & Simon (2008) study of M33, where dispersion was minimized for $F_{\lambda 5007}/F_{\lambda 3727} > 1.25$. The details of this analysis will be presented in D. A. Berg et al. (2020, in preparation).

3.2. Abundance Determinations

We calculate absolute and relative abundances using the PYNEB package in PYTHON, assuming a five-level atom model (De Robertis et al. 1987), the atomic data reported in Table 4 of B15, and the temperatures determined from the [O III], [S III], and/or [N II] measured temperatures in conjunction with T_e-T_e scaling relationships. We showed in Section 3.1 that our electron temperature results for the first four CHAOS galaxies are consistent with the C16 T_e-T_e relationships; therefore, we use Equations (1)–(3) to determine the temperatures of unmeasured ionization zones. Further, the dispersion in our measured T_e-T_e relationships correlates with the average ionization of the nebulae, as represented by the $O_{32}=F_{\lambda5007}/F_{\lambda3727}$ ratio.

We adopt the ionization-based temperature prioritization depicted in Figure 5. Specifically, if all three ionic temperatures are measured and the average ionization of the nebula is relatively high ($O_{32} > 1.25$), we prioritize $T_e[N II]$ for the low-ionization zone, $T_e[S III]$ for the intermediate-ionization zone,

and $T_e[{\rm O\ III}]$ for the high-ionization zone. If, instead, the average ionization of the H II region is relatively low $({\rm O}_{32}<1.25)$, we adopt the measured low- and intermediate-ionization zone temperatures as before but instead use $T_e[{\rm S\ III}]$ in combination with Equation (3) to infer the high-ionization zone temperature. The justification of this choice is the large dispersions for high-ionization points in the T_e-T_e relations shown in Figure 4, with the result that we have less confidence in $\lambda 4363$ in this regime (see discussion in Section 4.2). In the absence of a measurement of the appropriate ionization-zone temperature, temperatures should be inferred from the next preferred ion measured (following the ordering in Figure 5) in combination with the T_e-T_e relationships from Equations (1)–(3).

While the ionization-based temperature prioritizations presented here offer an improvement to temperature-based abundance determinations, we note two caveats. First, it is best to have independent measurements of the temperature in each ionization zone to reduce the reliability on relationships from photoionization modeling. Second, there are inherent, systematic uncertainties remaining due to the nominal assumption that H II region structures can be simply divided into three 1D ionization zones when the reality is much more complicated.

3.2.1. Oxygen Abundances

We adopt the ionization-based temperature prioritization recommended in Figure 5 in order to determine the abundances of the first four CHAOS galaxies in a uniform, homogeneous manner. Ionic abundances relative to hydrogen are calculated using:

$$\frac{N(X^{i})}{N(\mathbf{H}^{+})} = \frac{I_{\lambda(i)}}{I_{\mathbf{H}\beta}} \frac{j_{\mathbf{H}\beta}}{j_{\lambda(i)}},\tag{4}$$

where the emissivity coefficient, $j_{\lambda(i)}$, is sensitive to the adopted temperature.

The total oxygen abundance is calculated as the sum of the $^{+}/\mathrm{H}^{+}$ ion fractions. While emission from O^{+3} O^+/H^+ and O^{+-} is negligible in typical star-forming regions, some oxygen might be in O⁰ phase for the moderate-to-low ionization parameters characteristic of the CHAOS data $(-2.5 < \log$ U < -4.0; see, for example, Figure 5 in Berg et al. 2019). In the current work, we can estimate the typical contribution to the oxygen abundance by O^0 emission using the [OI] $\lambda 6300$ feature, which can be distinguished from the [O I] λ 6300 night sky line at the distances of our sample and the resolution of MODS. For our sample, the average $I([O I]\lambda 6300)/I(H\beta) =$ 0.022, corresponding to an $O^0/(O^0 + O^+ + O^{++})$ fraction of 3%. This means that, on average, the oxygen abundance may be underestimated by only $\Delta O/H < 0.02$ dex due to missing O⁰/H⁺ contributes. Given that possible contributions from O⁰ are typically less significant than the uncertainties on the oxygen abundance measurements, O⁰/H⁺ is not included in our oxygen abundance determinations, consistent with previously published CHAOS data.

The total oxygen abundances for our NGC 3184 sample are reported in Table A3 of Appendix A, noting that neither O⁰ nor contributions from dust (also typically <0.1 dex; Peimbert & Peimbert 2010; Peña-Guerrero et al. 2012) are included. Additionally, given that the abundances reported in previous CHAOS works were not derived with a methodology

consistent with Figure 5, we re-derive the abundances for NGC 628, NGC 5194, and NGC 5457 in order to compare our sample in a uniform manner. Since both NGC 628 and NGC 5194 were analyzed following the methodology laid out in B15 and both had very few [O III] λ 4363 detections, their results were not significantly modified. C16's study of NGC 5457, on the other hand, generally prioritized [O III]-derived temperatures for the purpose of comparing to T_e [O III]-based abundances in the literature. The total and relative abundances for NGC 628, NGC 5194, and NGC 5457 used in this work are report in Table B1 in Appendix B.

3.2.2. Nitrogen Abundances

We also observe significant N, S, Ar, and Ne emission lines in our spectra that allow us to determine their relative abundances. However, when emission lines from prominent ionization stages are absent in the optical, their abundance determinations require an ionization correction factor (ICF) to account for the unobserved ionic species. For nitrogen, we employ the common assumption that $N/O = N^+/O^+$, such that the $ICF(N) = (O^{++} \ O^{++})/O^+$ (Peimbert 1967). While the O^+ ionization zone overlaps both N^+ and N^{++} , $N/O = N^+/O^+$ benefits from comparing two ions in the same temperature zone, and Nava et al. (2006) found this assumption valid within a precision of roughly 10%. We report the ionic, total, and relative N abundances for NGC 3184 in Table A3 in Appendix A. We also list the ICF, where the uncertainty is solely a propagation of the emission-line uncertainties.

3.2.3. Sulfur Abundances

For sulfur, both S⁺ (10.36–22.34 eV) and S⁺⁺ (22.34–34.79 eV) span the O⁺ zone (13.62–35.12 eV), as the transitions from S⁺⁺ to S⁺³ and O⁺ to O⁺⁺ are nearly coincident. We note that the low-ionization energy of S⁺ means that [S II] emission can originate from outside the H II regions ($E \le 13.59$ eV), and therefore, caution must be used when interpreting these lines. While we do not currently correct for such diffuse ionized gas in CHAOS, the high-ionization of our nebulae ensure that this gas only constitutes a small fraction.

In high-ionization nebulae, $S^{\tilde{+}3}$ (34.79–47.22 eV) lies in the O^{++} zone (35.12–54.94 eV). To account for the unseen S^{+3} ionization state, we employ the ICF from Thuan et al. (1995) for high-ionization H II regions characterized for $O^+/O \leqslant 0.4$, where the total O is assumed to be $O = O^+ + O^{++}$. However, because the metal-rich H II regions of CHAOS are typically cooler and of moderate ionization, we follow the recommendation of C16 and adopt ICF(S) = O/O^{++} (or simply $S/O = (S^+ + S^{++})/O^+$) for $O^+/O > 0.4$ (see, also, Peimbert & Costero 1969). The resulting ICFs and ionic, total, and relative S abundances for NGC 3184 are tabulated in Table A3 in Appendix A. The uncertainty on the ICF(S) is a propagation of the emission-line uncertainties for $O^+/O > 0.4$ and 10% of the ICF(S) in the case of $O^+/O \leqslant 0.4$ (see Thuan et al. 1995).

3.2.4. Argon Abundances

In the case of argon, only the Ar^{++} ionization state is observed in the majority of CHAOS optical spectra, but the ionization potentials of O^+ (13.62–35.12 eV) and O^{++} (35.12–54.94 ev) encompass portions of Ar^+ (15.76–27.63 eV), Ar^{++} (27.63–40.74 eV), and Ar^{+3} (40.74–59.81 eV). While ratios of sulfur and oxygen ions relative to Ar^{++} have both been

used individually in the past to trace unseen argon ions, C16 found that the low-ionization regions of the CHAOS NGC 5457 sample are not well represented by either. Instead, C16 corrected for the decrease in $\mathrm{Ar^{++}/S^{++}}$ seen in low-ionization nebula by adopting a linear correction to $\mathrm{Ar^{++}/S^{++}}$: $\mathrm{log}(\mathrm{Ar^{++}/S^{++}}) = -1.049 \times (\mathrm{O^{+}/O}) -0.022$, for $\mathrm{O^{+}/O} \geqslant 0.6$. For higher-ionization nebulae, $\mathrm{Ar^{++}/S^{++}}$ was uncorrelated with $\mathrm{O^{+}/O}$ and so a constant value of $\mathrm{log}(\mathrm{Ar^{++}/S^{++}}) = -0.65$ was assumed, similar to Kennicutt et al. (2003b).

The $\log(Ar^{++}/S^{++})$ correction from C16 is shown in the top panel of Figure 6. The previously reported trend of decreasing Ar^{++}/S^{++} with increasing O^+/O is reproduced, but with more dispersion in the updated ionic abundances, especially for NGC 5457—the data it was derived for. We find that all four CHAOS galaxies follow just as well the Ar^{++}/O^{++} -based ICF of Thuan et al. (1995) over the full range in O^+/O probed by the sample. Given that three of the galaxies seem to be systematically offset from the Ar^{++}/S^{++} relation, we choose to apply the ICF(Ar) from Thuan et al. (1995), which has an uncertainty of 10%, to all four CHAOS galaxies. The differences between the updated ion fractions and those measured in C16 support the finding by Yates et al. (2020) and this work that ionization plays an important role in the temperature and metallicity determinations of an H II region. We list the resulting Ar abundances in Table A3 of Appendix A.

3.2.5. Neon Abundances

Neon is similar to argon in that only one ionization state is typically observed, Ne $^{++}$ (40.96–63.45 eV). Therefore, we use the ICF suggested by Peimbert & Costero (1969) and Crockett et al. (2006) to correct for the unobserved Ne $^+$ ions (21.57–40.96 eV): ICF(Ne) = $\rm O/O^{++}$, where standard propagation of errors is used to determine the uncertainty. Then, Ne/O = Ne $^{++}/\rm O^{++}$. Just as C16 reported a bifurcation in the Ne $^{++}/\rm O^{++}$ values of NGC 5457, we see a similar downward dispersion for low-ionization (O $^+/\rm O>0.5$) in the bottom panel of Figure 6 for our four-galaxy sample (see, also, Kennicutt et al. 2003a). Interestingly, we also note an upturn to high Ne $^{++}/\rm O^{++}$ values for some low-ionization nebulae.

The unseen Ne⁺ (21.56–40.96 eV) partially overlaps with both the O⁺ and O⁺⁺ ionization zones. This means that a significant fraction of Ne likely lies in the Ne⁺ state, especially for the moderate-ionization nebulae observed by CHAOS. This results in underestimated total Ne abundances in low- to moderate-ionization nebulae, a well-known issue with the classical ICF(Ne) (Torres-Peimbert & Peimbert 1977; Peimbert et al. 1992). García-Rojas et al. (2013) observed a similar trend in the Ne/Ar ratios of planetary nebulae, where low-ionization targets appeared Ne-poor and Ar-rich. Interestingly, many of the low Ne⁺⁺/O⁺⁺ CHAOS points also exhibit the lowest values of log(Ar/Ne), which are plotted as light blue circles in Figure 6.

Using the average Ar/Ne ratio of the CHAOS sample as a guide, we apply a Ne/Ar correction that is normalized to the average value for low-ionization regions $(O^+/O > 0.5)$ and update the Ne/O values (see Section 6.1). Overall, this correction seems to pull the regions with low-ionization Ne/O abundances up, while regions with suspiciously low Ar/O abundances in NGC 5457 are adversely affected. The resulting Ne abundances are reported in Table A3 of Appendix A. While this updated ICF (Ne) is clearly not perfect, these relationships are illuminating and

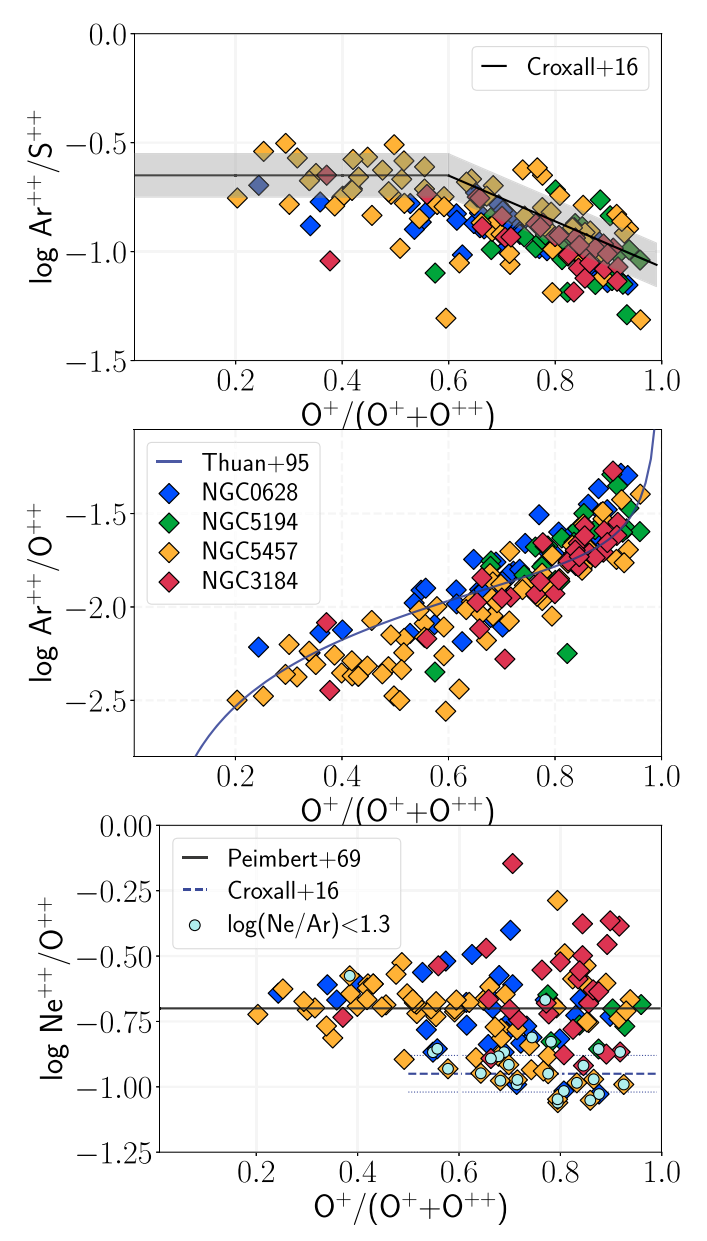


Figure 6. Three of the ICFs considered in this work vs. low-ionization fraction of oxygen, $O+/(O^{++}O^{++})$. In the top panel, we plot the Ar^{++}/S^{++} ICF relationship introduced by C16. We note that NGC 3184 seems to deviate from the relationship to lower Ar^{++}/S^{++} values with decreasing ionization. In the middle panel, we plot the Ar^{++}/O^{++} ratio and corresponding ICF(Ar) from Thuan et al. (1995). The NGC 3184 observations align well with this relationship. In the bottom panel, we plot the Ne^{++}/O^{++} ratio, revealing two populations at low ionization (see also C16). We also consider regions with low $\log(Ne/Ar)$ ratios (<1.3; light blue circles), which largely correspond to the Ne^{++}/O^{++} points.

suggest that a more sophisticated ICF is needed to fully correct the total Ne abundance. A more in depth discussion of the analysis of the CHAOS ICFs can be found in C16.

4. Radial Abundance Trends

4.1. Radial Oxygen Abundance Gradients

In the past, studies of radial abundance trends have used both a variety of methods to characterize abundance and to normalize the galactocentric radius to show significant variations in the

gradients of different galaxies (e.g., Zaritsky & Kennicutt 1994; Moustakas et al. 2010). However, many of these studies have relied on abundance measurements in just a handful of HII regions per galaxy. More recently, abundance trends have been studied in large numbers of H II regions using IFU spectroscopy of individual galaxies. Using empirical oxygen abundances determined from CALIFA IFU spectra, Sánchez et al. (2014) found a universal O/H gradient with a characteristic slope of $\alpha_{\rm O/H} = -0.10 \pm 0.09 \, {\rm dex}/R_e \, {\rm over} \, 0.3 < R_g/R_e < 2.0 \, {\rm for} \, 306$ galaxies, whereas Sánchez-Menguiano et al. (2016) report a shallower slope of $\alpha_{\rm O/H} = -0.075 \ {\rm dex}/R_e$, with $\sigma = 0.016 \ {\rm dex}$ for 122 face-on spiral galaxies. However, the recent study of 102 spiral galaxies using VLT/MUSE IFU spectra by Sánchez-Menguiano et al. (2018) found a distribution of slopes with an average of $\alpha_{\rm O/H} = -0.10 \pm 0.03$ dex/ R_e . These authors find that radial gradients are steepest when the presence of an inner drop or an outer flattening is also detected in the radial profile and point to radial motions in shaping the abundance profiles.

While IFU studies have greatly expanded our understanding of abundance gradients, they have thus far relied on strong-line abundance calibrations and, therefore, have systematic uncertainties (e.g., see reviews from Kewley & Ellison 2008; Maiolino & Mannucci 2019). CHAOS now allows us to compare radial abundance trends using large numbers of direct abundance measurements in H II regions. We display the O/H abundances derived in Section 3.2.1 for the four CHAOS galaxies in Figure 7 as a function of galactocentric radius. Because the locations of individual H II regions are known with high precision relative to one another, we consider only the uncertainties associated with oxygen abundance here. We plot the galactocentric radius relative to the isophotal (R_{25}) and effective (R_e) radii of each galaxy in the top and middle panels of Figure 7, respectively. Because there is no visual evidence for an outer disk flattening in the O/H gradient in the coverage of the CHAOS sample, we characterize the O/H gradient in each galaxy with a single, Bayesian linear regression using the python LINMIX code (solid lines). Parameters of the resulting fits are given in Table 2.

Comparing the individual O/H gradients in Figure 7, there are apparent differences in both the O/H versus R_g/R_{25} and O/H versus R_g/R_e gradients in the top and middle panels, respectively. While the gradients align more closely when plotted versus the effective radius (R_e), the gradients of individual galaxies are still uniquely distinct. The four CHAOS galaxies have a range of slopes of $-0.20 < \alpha_{\rm O/H}$ (dex/ R_e) < -0.07. Because the high-quality direct abundances of the CHAOS sample allow us to better constrain the unique gradient of an individual galaxy, we are seeing tangible gradient differences, even among just four galaxies, but within the dispersion seen for the large CALIFA samples of strong-line abundances. In this sense, the CHAOS data are demonstrating that O/H versus R_g/R_e gradients are *not* uniformly behaved.

NGC 5194 presents the largest deviation from the typical CHAOS slope, where its nearly flat slope has been attributed to interactions with its companion, NGC 5195, resulting in radial migration and mixing of the interstellar gas (see discussion in C15). However, even when we only consider the three noninteracting spiral galaxies in our sample, we find tangible differences in the O/H abundance gradients and dispersions of individual CHAOS galaxies. The varying coefficients of the best-fit gradients characterizing the CHAOS galaxies (tabulated

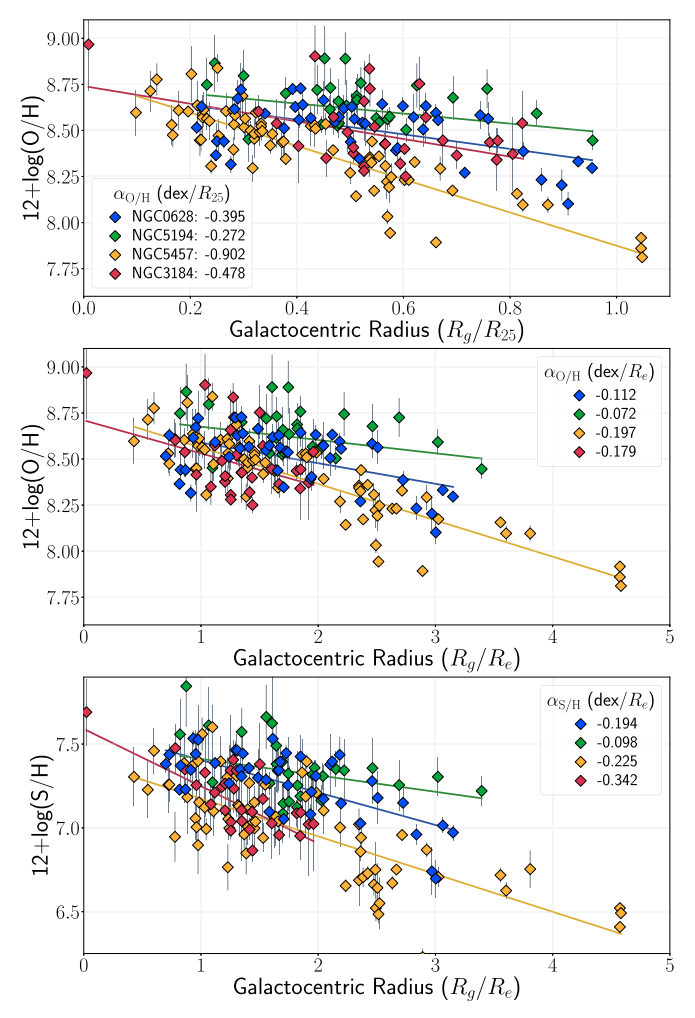


Figure 7. Abundance trends plotted vs. galactocentric radius for the first four CHAOS galaxies: the O/H gradient normalized to the R_{25} radius of each galaxy (top panel), the O/H gradient normalized to each galaxy's effective radius, R_e (middle panel), and the S/H gradient normalized to R_e (bottom). We note that the O/H gradients appear to be no more ordered when plotted relative to R_e , as originally proposed by Sánchez et al. (2014), as they show individual differences in their slopes and dispersions regardless of the radial normalization. Interestingly, S/H gradients show a similar ordering as O/H. See Table 1 for properties of the CHAOS galaxies.

in Table 2) show that detailed direct abundance measurements reveal a range in the chemical evolution of individual galaxies.

4.2. Radial Sulfur Abundance Gradients

Sulfur abundances can be an extremely useful tool, particularly in the absence of oxygen abundance information. Notably, sulfur abundances only require a limited wavelength coverage of $\sim\!\lambda4850-\lambda9100$ (but better if coverage extends to $\sim\!\lambda9600$) to ensure measurement of all the necessary inputs to a direct abundance: (i) reddening correction (from $H\alpha/H\beta$ and the Paschen lines), (ii) density (from [S II] $\lambda6717/\lambda6731$), (iii) temperature (from [S III] $\lambda6312/\lambda9069$), (iv) S⁺ (from [S II] $\lambda\lambda6717,6731$), and (v) S⁺⁺ (from [S III] $\lambda\lambda9069,9532$). Surveys with limited blue-wavelength coverage (e.g., MUSE; Bacon et al. 2010) may therefore be able to take advantage of sulfur's utility and measure direct abundance trends in the absence of the blue oxygen lines.

Prompted by the importance of S as a temperature indicator, and the expectation of alpha elements that S and O abundances

should trace one another, we explore the S/H gradients of the CHAOS galaxies in the bottom panel of Figure 7. As before, we fit Bayesian linear regression models and report the results in Table 2. The S/H and O/H gradients of our galaxies are all consistent within the uncertainties, with the interesting exception of NGC 628. These fits suggest that S/H abundances provide an alternative direct measurement of a galaxy's metallicity gradient. S/H abundances may also be easier to measure in moderate- to metal-rich H II regions where [S III] λ 6312 is significantly detected more often than [O III] λ 4363. However, it is important to note that S/H abundances have the disadvantage of requiring an ICF for the unseen S⁺³ and, thus, are generally considered inferior to O/H abundances. Typically, in the CHAOS sample, the correction for S⁺³ is less than 20%, but it can get as high as 80%, so caution is warranted.

Why does sulfur seem to behave so well for the CHAOS sample? While the dominant observable ionic states of O in the CHAOS spectra, O⁺ and O⁺⁺, probe the full ionization range of HII region nebulae, our data largely consist of moderateionization nebulae. Our regions have O⁺/O ionization fractions that are typical of the more metal-rich H II regions in spiral galaxies, and this combination produces regions that both exhibit more moderate ionization and have cooler temperatures. Given this, it is perhaps not surprising that $T_e[S III]$ characterizes the CHAOS data so well. At the typically higher metallicities of the CHAOS regions, the nebula are generally lower-excitation and so have large S^{++} fractions (i.e., S^{++} is the dominant ionization zone). To be quantitative, given the excitation energy of [S III] $\lambda 6312$ (3.37 eV), a temperature of $T_e \sim 7000$ K is required for 1% of the electrons to excite [S III]. This temperature is well matched to the majority of our HII regions, which have temperature measurements of 6000 K $< T_e < 8000$ K. On the other hand, the excitation energy of [O III] $\lambda 4363$ (5.35 eV) requires a much hotter nebular temperature of $T_e \sim 11,000 \text{ K}$ for 1% of electrons to excite [O III]. In these typically moderateionization nebula, not only is O^{++} a sub-dominant ion, but the relatively low electron temperature of the gas will rarely excite to the upper level of O^{++} from which $\lambda 4363$ is emitted. In contrast, the observable ionic states of S in the CHAOS spectra (S^+, S^{++}) probe the lower-ionization zones (\$\frac{35}{eV}\$) that are dominant in the majority of metal-rich H II regions.

4.3. Radial N/O Abundance Gradients: A Universal N/O Relationship

The N/O abundances for the four CHAOS galaxies are presented in Figure 8. Galactocentric radii are normalized to the isophotal radius, R_{25} , of each galaxy in the top panel and to the effective radius, R_e , in the bottom panel. Once again, we analyze gradients of galaxies by comparing their individual Bayesian linear regression fits (solid lines). Interestingly, when trends in N/O versus R_g/R_{25} are considered as a single, linear relationship as was done with O/H in Section 4.2, all four galaxies appear to have similar gradients, only offset from one another. Additionally, as noted in previous CHAOS papers, the N/O relationships are more tightly ordered with radius than the O/H gradients, presented by smaller dispersions. On the other hand, when the N/O trends are normalized by their effective radius (bottom panel), three of the four galaxies (NGC 628, NGC 5457, and NGC 3184) shift to lie nearly on top of one another, while NGC 5194 emerges as an outlier once again.

We further investigate the similarities of the CHAOS N/O gradients by comparing them over the same radial extent.

Table 2
Linear Fits to CHAOS Gradients

у	х	Galaxy	# Reg.	Equation	$\sigma_{ m int.}$	$\sigma_{\rm tot.}$
$12 + \log(O/H) \text{ (dex)}$	$R_g (R_{25}^{-1})$	NGC 0628	45	$y = (8.71 \pm 0.06) - (0.40 \pm 0.11) \times x$	0.12	0.13
		NGC 5194	28	$y = (8.75 \pm 0.09) - (0.27 \pm 0.15) \times x$	0.07	0.10
		NGC 5457	72	$y = (8.78 \pm 0.04) - (0.90 \pm 0.07) \times x$	0.10	0.11
		NGC 3184	30	$y = (8.74 \pm 0.16) - (0.48 \pm 0.28) \times x$	0.14	0.16
	$R_g (R_e^{-1})$	NGC 0628	45	$y = (8.70 \pm 0.06) - (0.11 \pm 0.03) \times x$	0.12	0.13
		NGC 5194	28	$y = (8.67 \pm 0.08) - (0.07 \pm 0.04) \times x$	0.07	0.10
		NGC 5457	72	$y = (8.75 \pm 0.03) - (0.20 \pm 0.02) \times x$	0.10	0.11
		NGC 3184	30	$y = (8.71 \pm 0.15) - (0.18 \pm 0.10) \times x$	0.14	0.16
$12 + \log(S/H)$ (dex)	$R_g (R_e^{-1})$	NGC 0628	45	$y = (7.60 \pm 0.06) - (0.19 \pm 0.03) \times x$	0.12	0.13
		NGC 5194	28	$y = (7.51 \pm 0.11) - (0.10 \pm 0.05) \times x$	0.07	0.12
		NGC 5457	72	$y = (7.40 \pm 0.05) - (0.23 \pm 0.03) \times x$	0.18	0.19
		NGC 3184	30	$y = (7.59 \pm 0.15) - (0.34 \pm 0.11) \times x$	0.11	0.13
log(N/O) (dex)	$R_g (R_{25}^{-1})$	NGC 0628	59	$y = (-0.64 \pm 0.04) - (0.61 \pm 0.06) \times x$	0.10	0.11
		NGC 5194	28	$y = (-0.34 \pm 0.09) - (0.44 \pm 0.16) \times x$	0.05	0.08
		NGC 5457	72	$y = (-0.73 \pm 0.03) - (0.81 \pm 0.06) \times x$	0.07	0.10
		NGC 3184	30	$y = (-0.30 \pm 0.13) - (0.83 \pm 0.22) \times x$	0.04	0.08
	$R_g (R_e^{-1})$	NGC 0628	59	$y = (-0.65 \pm 0.03) - (0.18 \pm 0.02) \times x$	0.10	0.11
		NGC 5194	28	$y = (-0.34 \pm 0.09) - (0.12 \pm 0.04) \times x$	0.05	0.08
		NGC 5457	72	$y = (-0.74 \pm 0.03) - (0.18 \pm 0.01) \times x$	0.08	0.10
		NGC 3184	30	$y = (-0.30 \pm 0.12) - (0.35 \pm 0.09) \times x$	0.05	0.08
$log(N/O)_{prim.}$ (dex)		NGC 0628	11	y = -1.28		0.13
		NGC 5194	4	y = -0.71		0.03
		NGC 5457	15	y = -1.38		0.13
		NGC 3184	0	y = -1.15		
$log(N/O)_{sec.}$ (dex)	$R_g (R_e^{-1})$	NGC 0628	38	$y = (-0.43 \pm 0.05) - (0.34 \pm 0.04) \times x$	0.06	0.07
		NGC 5194	20	$y = (-0.27 \pm 0.18) - (0.17 \pm 0.11) \times x$	0.07	0.09
		NGC 5457	45	$y = (-0.58 \pm 0.07) - (0.30 \pm 0.05) \times x$	0.06	0.08
		NGC 3184	30	$y = (-0.30 \pm 0.12) - (0.35 \pm 0.09) \times x$	0.05	0.08
Scaled	p (p=1)	411.5	122	(0.15 0.00) (0.26 0.00)	0.05	0.00
$log(N/O)_{sec.}$ (dex)	$R_g (R_e^{-1})$	All Four	133	$y = (-0.15 \pm 0.03) - (0.36 \pm 0.02) \times x$	0.05	0.09
		NonInter.	113	$y = (-0.16 \pm 0.03) - (0.34 \pm 0.02) \times x$	0.05	0.08

Note. Linear fits to trends in abundance versus radius for the four CHAOS galaxies. The fits are determined using the Bayesian linear mixture model implemented in the LINMIX python code, which fits data with uncertainties on two variables, including explicit treatment of intrinsic scatter. The y and x variables are given in the first two columns, with the number of associated H II regions used in the fit listed in Column 4. The resulting best fit is given in Column 5, with uncertainties on both the slope and y-intercept. Columns 6 and 7 list the intrinsic and total uncertainties, σ_{tot} , and σ_{int} . Note that the primary $\log(N/O)$ value given for NGC 3184 is italicized to indicate that this quantity is an estimated value from the extrapolated secondary fit, and not a measurement.

Limited by the coverage of NGC 3184, we refit the N/O gradient of the $R_g/R_e < 2.0$ inner disks of the CHAOS galaxies with a Bayesian linear regression model and plot them as solid lines in the top left-hand panel of Figure 9. Now, three of the four galaxies have trends that run parallel to one another: all have very tight trends with slopes of $\alpha_{\rm N/O} = -0.3~{\rm dex}/R_e$ and dispersions of $\sigma < 0.06~{\rm dex}$ (see Table 2). Given that the inner disk radial gradients decline more steeply for N/O than O/H, these trends are indicative of secondary nitrogen.

In order to isolate the secondary N/O trend of the CHAOS sample, we remove the offset between galaxies by subtracting their individual *y*-intercept offsets. The resulting scaled N/O versus O/H relationships are shown in the bottom left-hand panel of Figure 9, where a tight secondary N/O relationship emerges that characterizes the entire CHAOS sample well. Given the relatively flat gradient of NGC 5194 in the top left-hand panel of Figure 9, we fit the secondary N/O relationship excluding NGC 5194 (denoted by the semi-transparent green points) in the bottom left-hand panel of Figure 9. The Bayesian

linear regression reports a slope of $\alpha_{\rm N/O} = -0.33~{\rm dex}/R_e$, with a very small total dispersion of $\sigma = 0.08~{\rm dex}$.

It is remarkable that a simple shift produces such a tight secondary N/O gradient for these three galaxies and indicates that a physical origin may be responsible. A common interpretation of N/O trends owes vertical offsets to differences in individual star formation histories (SFHs) that set the primary N/O plateau (e.g., Henry et al. 2000). Given the limited disk coverage of the CHAOS sample, it is difficult to determine the primary N/O plateau that is expected at large radii (low metallicity). However, we can explore the existing data in the outer disk as an illustrative exercise. Using NGC 5457 as our best and largest data set for exploring radial trends, we note that the N/O trend is approximately flat for $R_g/R_e > 2.5$, and so we adopt $2.0 < R_g/R_e < 2.5$ as the transition from primary to secondary N production (grayshaded band). In the upper right-hand panel of Figure 9, we fit a weighted average to the N/O values for $R_g/R_e > 2.5$. For NGC 3184, no N/O measurements exist for $R_g/R_e > 2.5$, and

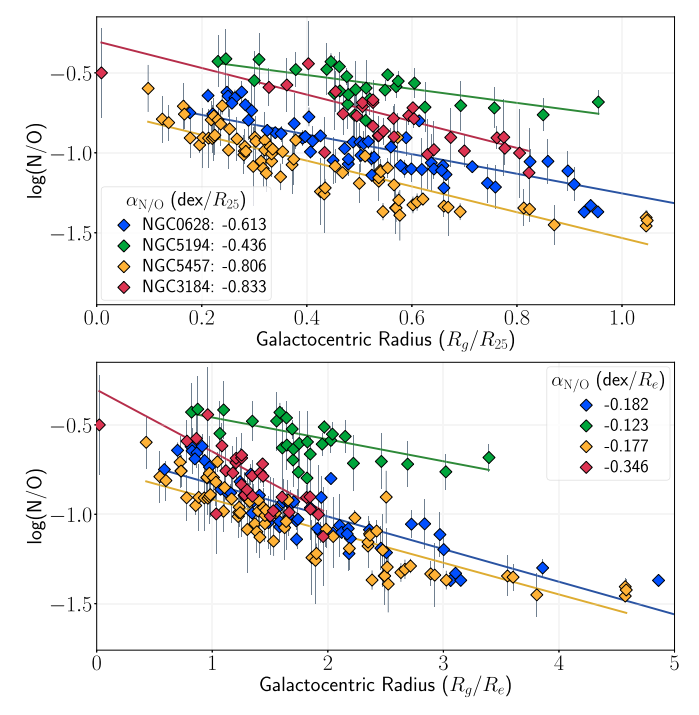


Figure 8. N/O abundance plotted vs. galactocentric radius for CHAOS galaxy sample presented here. Top panel: similar to Figure 6; the N/O trend is normalized to the R_{25} radius for each galaxy. Bottom panel: the N/O gradient relative to effective radius, R_e . NGC 5194 appears as a clear outlier when plotted in this way.

so a (toy-model) plateau was assumed based on the value of the extrapolated secondary relationship at the transition radius.

In the bottom right-hand Figure 9, we apply a second scaling method. We normalize the individual N/O relationships by their corresponding plateaus and once again see that a tight secondary N/O relationship emerges that characterizes the inner disk of the CHAOS sample well. Fitting a Bayesian linear regression to the three noninteracting galaxies, we find a slope of $\alpha_{\rm N/O} = -0.34~{\rm dex}/R_e$ and $\sigma = 0.08$, equal to the slope determined using a y-intercept offset. Once again, we find remarkable consistency of the N/O gradient slopes, regardless of the offset method used, suggesting a universal N/O gradient. The agreement between the bottom two panels of Figure 9 may be indicative of a break near $2.0 < R_g/R_e < 2.5$ and a transition to a flatter gradient for $R_g/R_e > 2.5$. We currently do not have sufficient data coverage of the outer CHAOS disks, but more radially extended data sets will be able to test this break/plateau prediction. Coefficients for the secondary N/O fits are tabulated in Table 2.

If the slope of N/O versus radius is simply dependent on metallicity, then a universal N/O gradient like the one depicted in Figure 9 can be interpreted as resulting directly from the nucleosynthetic yields of the stars producing it. In yield models, the integrated N yield is dominated by intermediate-mass stars and increases with increasing metallicity, while the oxygen yields from massive stars decrease with increasing metallicity. Further, the small observed scatter about this relationship could result from the fact that we are observing regions of star formation with differing average burst ages, and the majority of N is produced around 250 Myr after the burst onset, whereas the massive stars producing oxygen have mainsequence lifetimes of only a few Myr (see discussion in Section 7).

5. Secondary Drivers of Abundance Trends

Even with the precise abundance gradients of spiral galaxies afforded by the CHAOS project, many open questions remain regarding metallicity gradients in disk galaxies. Here, we explore possible environmental effects through azimuthal variations and surface-density profiles.

5.1. Azimuthal Variations

Beyond simple gradients in spiral galaxies, other patterns in the spatial distribution of metals in the ISM may be key to understanding the redistribution of recently synthesized products. While some processes happen on relatively short timescales, such as local oxygen production from massive stars (<30 Myr; Pipino & Matteucci 2009) and H II region mixing on subkiloparsec scales (<100 Myr), the timescale for differential rotation to chemically homogenize an annulus of the ISM is much longer (~1 Gyr; see, e.g., Kreckel et al. 2018). Further, the fate of metals after they are produced is unclear, as the spatial and temporal scales on which oxygen enriches the ISM are poorly known. Therefore, azimuthal inhomogeneities are expected and can inform us about asymmetric processes occurring in the disk.

Ho et al. (2017) studied the azimuthal variations in the oxygen abundance gradient of the nearby, strongly barred, spiral galaxy NGC 1365 as part of the TYPHOON program, finding O/H to be lower, on average, by 0.2 dex downstream from the spiral arms. Given the strong correlation with spiral pattern, these authors find that the observed abundance variations are due to the mixing and dilution processes driven by the spiral density waves. On the other hand, the TYPHOON program has also reported a much smaller magnitude of 0.06 dex azimuthal variations for the unbarred spiral galaxy NGC 2997 (Ho et al. 2018).

We test for azimuthal variations in the CHAOS sample by examining the offset in direct abundance from each galaxy's average gradient for O/H and N/O as a function of both radius and position angle within the disk. We find no evidence of systematic azimuthal variations in the direct abundance CHAOS sample of unbarred spiral galaxies explored here. However, while CHAOS observations span broad radial and azimuthal coverage, region selection is biased to the highest surface-brightness H II regions and so may not include the faint inter-arm coverage needed to unveil these subtle trends.

5.2. Surface-density Relationships

A fundamental relationship of global galaxy evolution is the luminosity—metallicity relationship, which includes spiral disk galaxies (e.g., Garnett & Shields 1987; Vila-Costas & Edmunds 1993; Zaritsky & Kennicutt 1994). This relationship typically refers to the total or average metallicity of a galaxy, but what does this mean for the abundance gradients in individual spiral galaxies? While several recent studies support a characteristic oxygen abundance gradient for the main disk of spiral galaxies (e.g., Sánchez et al. 2014; Sánchez-Menguiano et al. 2018), Belfiore et al. (2017) reported an increasing oxygen abundance slope (dex/ R_e) with stellar mass for Sloan Digital Sky Survey-IV MaNGA (Bundy et al. 2015) galaxies with $M_{\star} < 10^{10.5} M_{\odot}$. However, in a study of 49 local starforming galaxies, Ho et al. (2015) found that metallicity gradients expressed in terms of the isophotal radius (R_{25}) did not correlate with either stellar mass or luminosity but rather

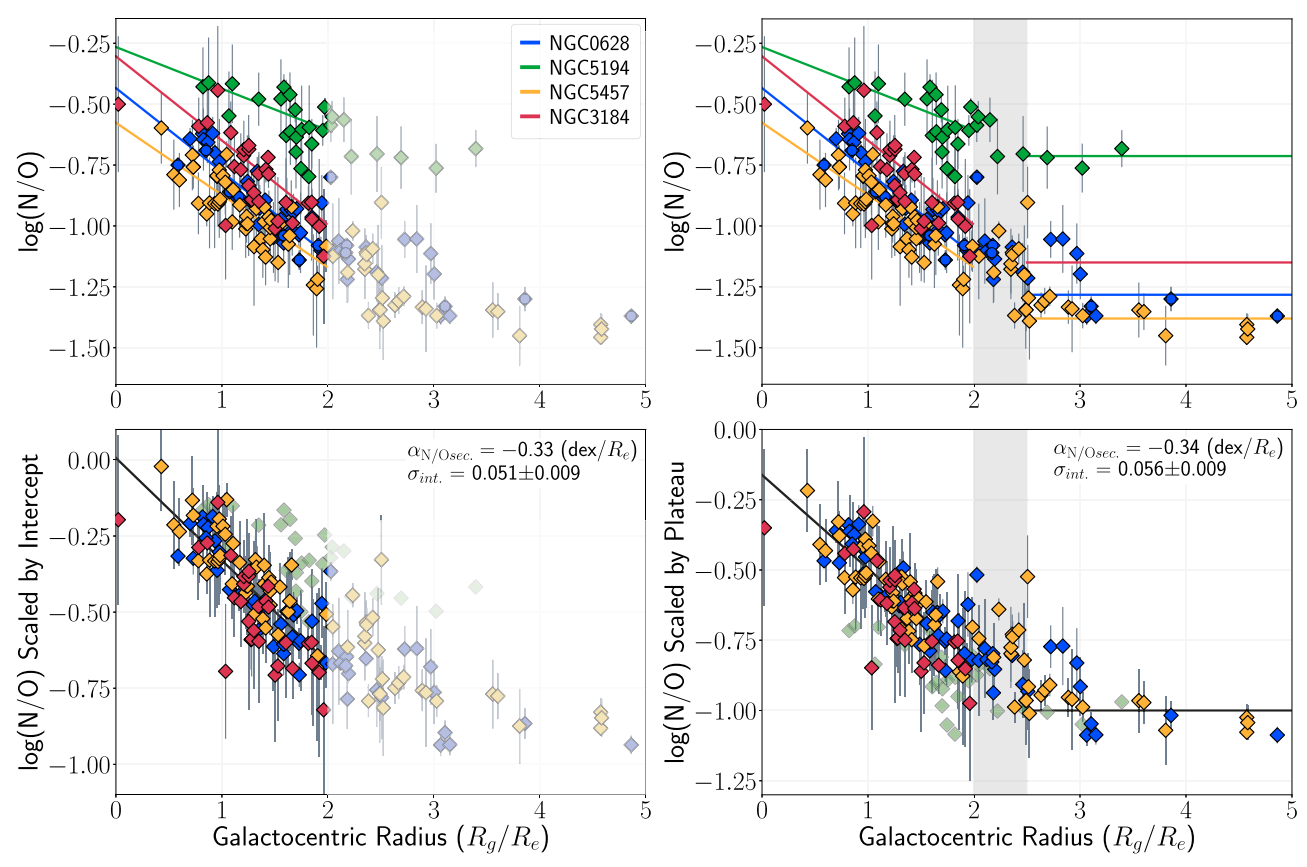


Figure 9. Top left panel: N/O vs. galactocentric radius of the CHAOS sample with separate fits to N/O for inner disks ($R_e/R_g < 2.0$). Bottom left panel: N/O trends of each galaxy are offset by the *y*-intercept of their fits above, producing a remarkably tight N/O gradient for the three noninteracting galaxies. Top right panel: Considering the full gradient, data in the outer disk ($R_e/R_g > 2.5$) appears to form a flatter trend and so we shade the potential transition gray. As an illustrative exercise, a variance-weighted average plateau is fit for $R_e/R_g > 2.5$ for each galaxy (and assumed for NGC 3184 based on the extrapolated fit for $R_g/R_e < 2.25$). Bottom right panel: N/O trends are normalized by the average outer disk N/O value of each galaxy, again revealing a universal N/O gradient for $R_e/R_g < 2.0$. If these trends are physical, then the outer flat trend may be the primary N plateau set by the galaxy's SFH, and the inner gradient may be a primary+secondary N trend that transitions near $2.0 < R_e/R_g < 2.5$. Data sets with larger radial coverage are needed to test this prediction.

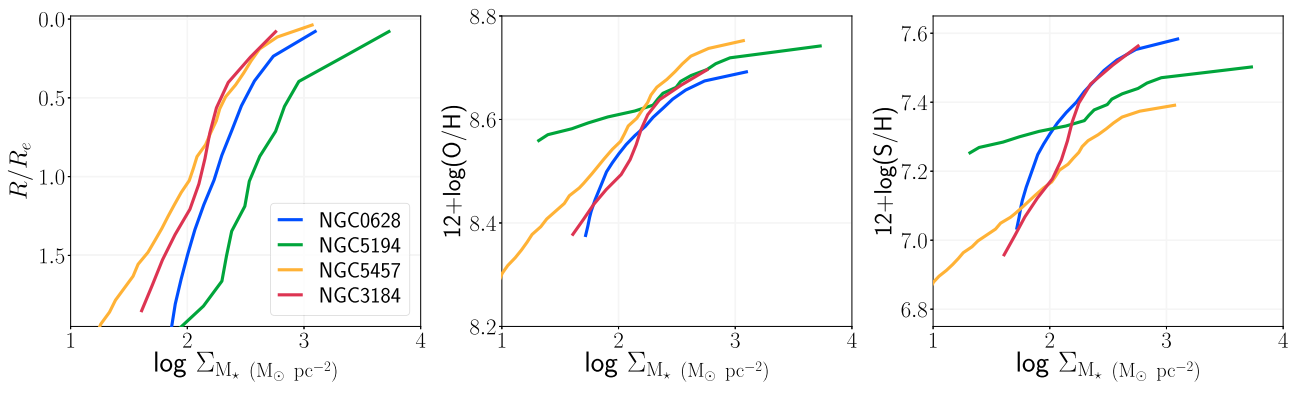


Figure 10. Stellar-mass surface-density trends for the four CHAOS galaxies relative to galactocentric radius (left panel), oxygen abundance (middle panel), and sulfur abundance (right panel). While NGC 5194 has abnormally flat abundance trends, the oxygen abundance of the three noninteracting galaxies closely correlates with stellar-mass surface density.

increase with decreasing total stellar mass when expressed in terms of dex kpc⁻¹ (see, also, Pilyugin et al. 2019). Alternatively, Pilyugin et al. (2019) concluded in their study of MaNGA galaxies that oxygen abundance is governed by a galaxy's rotational velocity. Despite these works, no clear evidence has emerged to conclusively determine the dependence of abundance gradients on basic galaxy properties or halo properties (e.g., rotational velocity).

Locally, the oxygen abundance trends of spiral galaxies have also been observed to correlate with stellar-mass surface density (e.g., McCall 1982; Edmunds & Pagel 1984; Ryder 1995; Garnett et al. 1997). In Figure 10, we examine the stellar-mass surface-density profiles for the CHAOS galaxies (see Appendix C for details). The left panel shows the typical trend of decreasing stellar-mass surface density as you move further out in the disk but with NGC 5194 having a

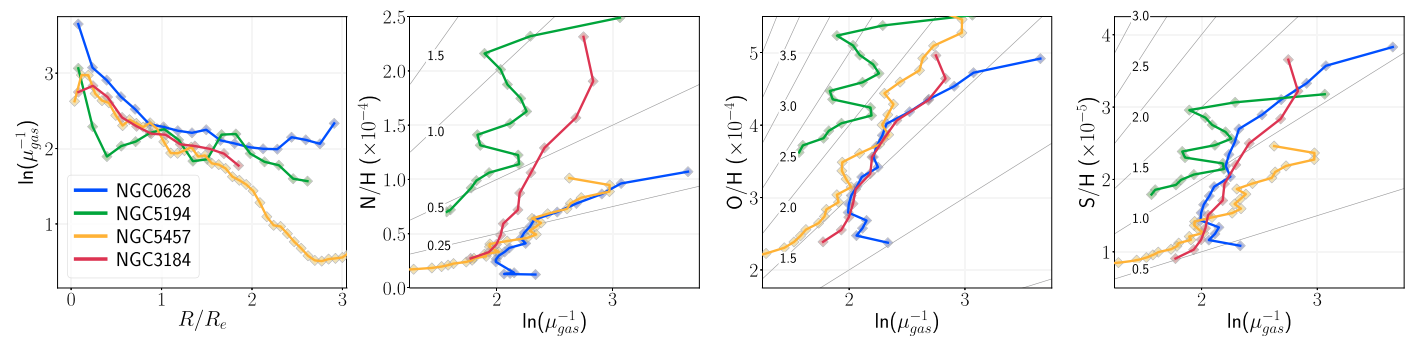


Figure 11. Trends of the logarithm of the inverse of the gas fraction for the CHAOS sample. The radially averaged profiles are similar for all four galaxies (first panel), whereas abundance trends for N/H (second panel), O/H (third panel), and S/H (last panel) show more significant variations. For the abundance vs. inverse gas fraction trends, lines of constant elemental effective yield are drawn, where the yield labels are in that same units as the y-axis ($\times 10^{-4}$, $\times 10^{-4}$, and $\times 10^{-5}$ for N/H, O/H, and S/H, respectively).

slightly elevated density of stars compared to the others. In the middle and right panels, we plot the local surface mass—metallicity relationship for O/H and S/H, respectively. Similar to the global relationship (see, e.g., Tremonti et al. 2004), local metallicity measurements also increase with mass surface density and plateau at high mass values. This local trend is especially tight for the three noninteracting CHAOS galaxies.

The metallicity-surface-density relationships in Figure 10 may reflect fundamental similarities in the evolution of nonbarred, noninteracting spiral galaxies. For example, Ryder (1995) argues for a galaxy evolution model that includes selfregulating star formation, where energy injected into the ISM by newly formed stars inhibits further star formation. These models were able to successfully reproduce the observed correlations between surface brightness and star formation rate (SFR; Dopita & Ryder 1994) and surface mass density (e.g., Phillipps & Edmunds 1991; Ryder 1995; Garnett et al. 1997). The current work supports these ideas that stellar-mass, gasmass, and SFR surface densities are fundamental and interdependent parameters that govern the chemical evolution of spiral galaxies. A more thorough investigation of the dependence of metallicity on local properties will be conducted in the future with the entire CHAOS sample.

5.3. Effective Yields

In a simple closed-box model, assuming instantaneous recycling of stellar nucleosynthetic products and no gas flows, chemical evolution is solely a function of the gas fraction, $\mu_{\rm gas}$: $Z = y \cdot \ln(\mu^{-1})$, where Z is the metallicity and y is the metal yield. Inverting this equation, one can measure the effective yield, $y_{\rm eff}$, given the observed metallicity, $Z_{\rm obs}$, and gas fraction:

$$y_{\rm eff} = \frac{Z_{\rm obs}}{\ln(\mu_{\rm gas}^{-1})}.$$
 (5)

In Figure 11, we plot the radially averaged inverse gas fraction trends for the CHAOS sample (see Appendix C for the sources of the gas distributions). While the inverse gas fractions steadily decrease with increasing radius for all four galaxies (left panel), plotting abundance versus inverse gas fractions reveals different effective yield trends (three right panels). Nonetheless, the trends appear to be the most ordered for O/H and S/H, with similar slopes among the three noninteracting galaxies. The less-ordered trends for N/H may then be revealing the effects of varying gas flows in each galaxy and

the time effects of production in lower-mass stars. Further, this picture is consistent with the result from theoretical models based on stochastically forced diffusion that most scatter in observed abundance gradients (\sim 0.1 dex) is due to stellar feedback and gas velocity dispersion (Krumholz & Ting 2018).

Following Equation (5), these plots of abundance versus the inverse gas fraction trace the effective yield of the relevant element. The true yield is a function of stellar nucleosynthesis, but the effective yield (slope of Z–ln($\mu_{\rm gas}^{-1}$) plots) will be altered from this value by gas inflows and outflows. In this context, the similar slopes in O/H and S/H versus ln($\mu_{\rm gas}^{-1}$) are indicative of a closed-box effective yield of both oxygen and sulfur, whereas the O/H and S/H trends of NGC 5194 diverge as expected for gas flows associated with interacting galaxies. According to Figure 11, the CHAOS galaxies generally follow slopes of $(0.5-1.25) \times 10^{-5}$ for sulfur and $(1.5-2.0) \times 10^{-4}$ for oxygen, which corresponds to $y_{eff}(O) = 0.006-0.008$ assuming Z = $0.02~\rm{Z}_{\odot}~\rm{and}~12 + \log(O/H)_{\odot} = 8.69$ (Asplund et al. 2009). These $y_{\text{eff}}(O)$ values are consistent with the range of effective oxygen yields measured for spiral galaxies by Garnett (2002), spanning 0.0033-0.017. We note that the effective yield values (Garnett 2002) found for NGC 628 and NGC 5194 are higher than our own, but this difference is largely accounted for by the offset in the measured abundance scales for these two galaxies.

6. Abundance Trends with Metallicity

6.1. Alpha/O Abundances

Next, we turn our focus from abundance gradients to relative abundance trends with O/H metallicity. In Figure 12, we plot the relative abundances of α -elements. In descending panel order, we plot S/O, Ar/O, and Ne/O as a function of O/H (left side), where diamond points are color-coded according to galaxy.

Stellar nucleosynthetic yields (e.g., Woosley & Weaver 1995) indicate that α -elements are predominantly produced on relatively short timescales by core-collapse supernovae (SNe; massive stars) explosions. The α -element ratios in Figure 12 are, therefore, expected to be constant, so we plot the variance-weighted mean α/O ratios of the CHAOS observations as black dashed lines in each panel. The average values are denoted in the upper left corners and can be compared to the solar values from Asplund et al. (2009; blue dotted line). The average CHAOS α/O values are generally greater than solar, but individual galaxies also show slight shifts from one another.

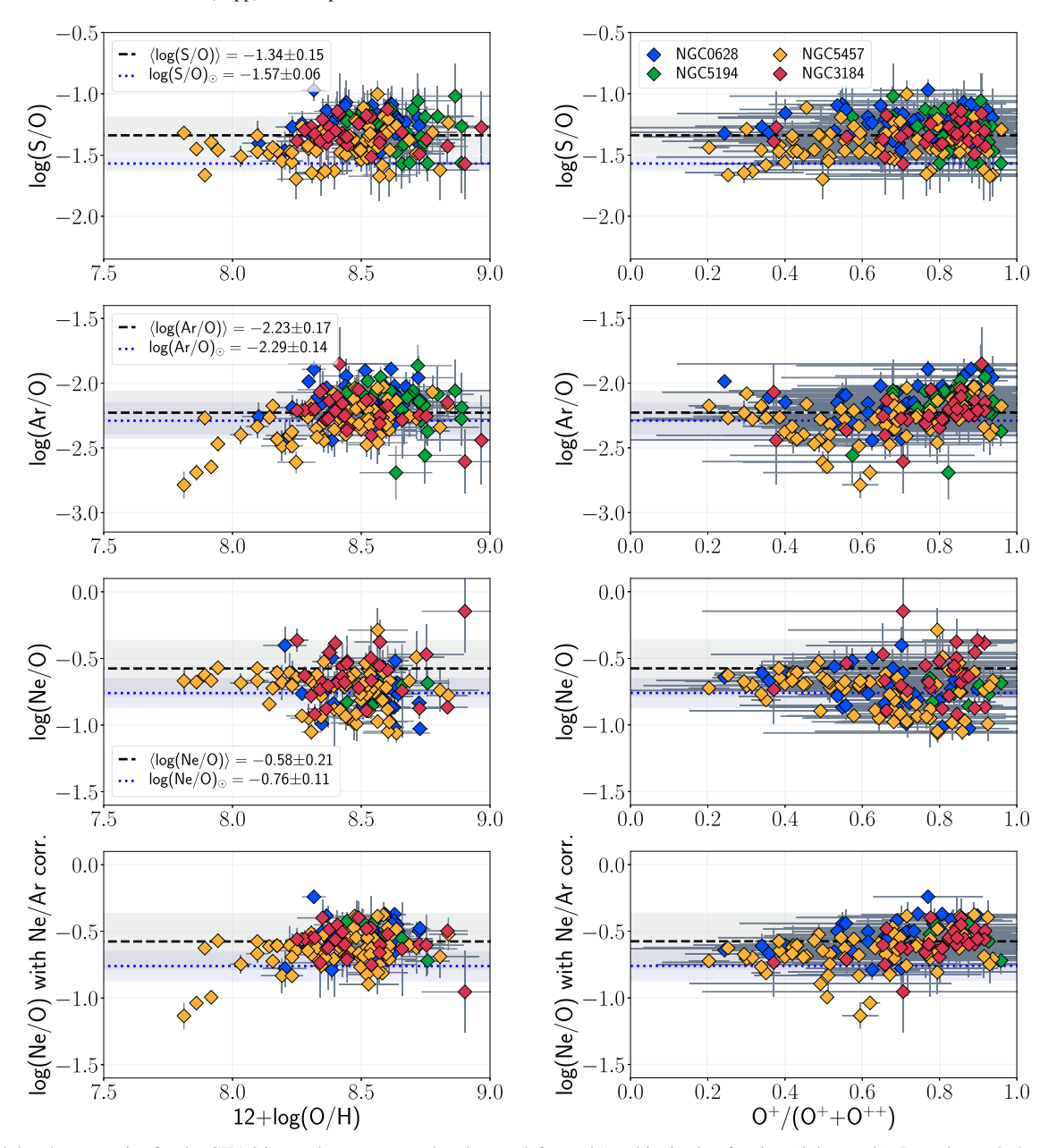


Figure 12. Alpha-element ratios for the CHAOS sample vs. oxygen abundances (left panels) and ionization fraction (right panels). In each panel, the solar value and uncertainty from Asplund et al. (2009) is labeled and plotted as a blue dotted line and blue shaded band, respectively. The weighted average and uncertainty of the CHAOS data are also given and denoted by a black dashed line and black shaded band, respectively. The top two rows show the S/O and Ar/O ratios, both with relatively flat distributions. The Ar/O abundances for NGC 5457 were corrected by C16 using the Ar^{++}/S^{++} relation shown in Figure 6; however, NGC 3184 uses the ICF(Ar) from Thuan et al. (1995). The bottom two rows show the Ne/O ratio using the standard Ne⁺⁺/O⁺⁺ ICF (third row) and when it is further corrected for offsets in the Ne/Ar ratio (bottom row).

Relative to the constant relationship assumed in each panel of Figure 12, the CHAOS observations visually show significant scatter and may also deviate in a systematic way. C16 discovered a significant population of low-ionization (high O⁺/O) H II regions in NGC 5457 with low Ne/O values. A deeper exploration of the α /O ratios in that work revealed a lack of previous observations in the low-ionization regime and challenges in finding an appropriate ICF to use.

Similar to C16, in Section 3.2.5, we found a large dispersion in the Ne^{++}/O^{++} ratios of the CHAOS galaxies for low-ionization H II regions. Additionally, many of these regions also exhibit exceptionally low values of log(Ar/Ne) (see Figure 6). This motivated us to apply a correction to the Ne/O

abundances based on the offset in Ne/Ar from the average CHAOS value for low-ionization H II regions (${\rm O^+/O} > 0.5$). The updated Ne/O values, plotted in the bottom panel of Figure 12, show a smaller dispersion around the mean sample value but with a few significant NGC 5457 outliers. While the proposed correction removes the bifurcation in Ne/O at low ionization, it seems to over-correct the Ne/O abundance for the nebulae with discordantly low Ar/O abundances.

Following C16, we further examine the α/O dependence on ionization by plotting our α/O ratios for the four CHAOS galaxies versus O^+/O in the right column of Figure 12. For both Ar and S, there seems to be a small residual systematic dependence on ionization that is not adequately corrected for

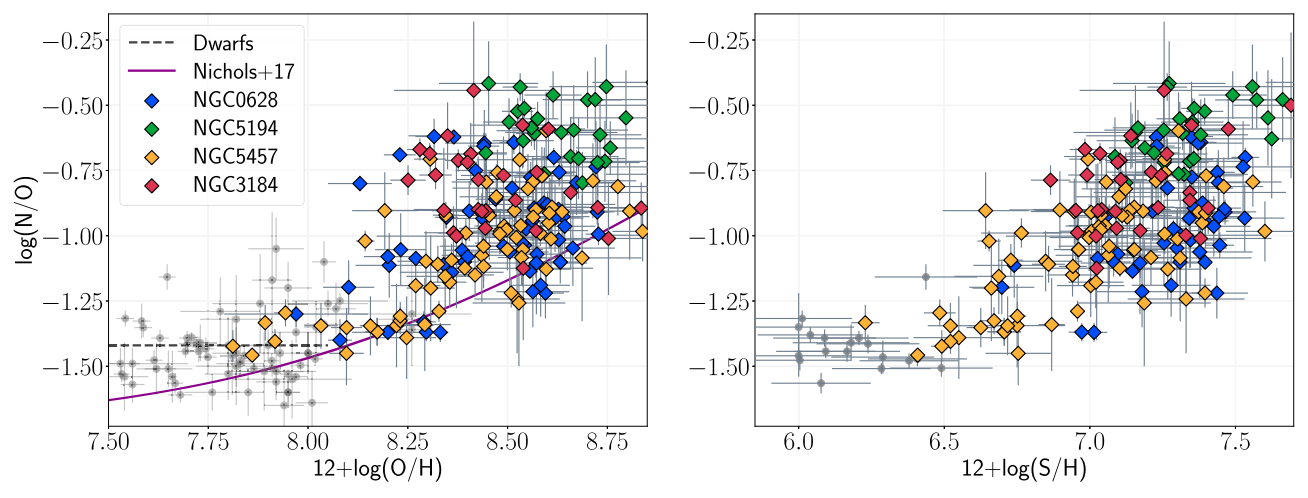


Figure 13. N/O vs. O/H (left panel) and S/H (right panel) for the CHAOS galaxies (diamonds) and local dwarf galaxies (gray circles). At low O/H or S/H, N is dominated by primary production and N/O is low (the gray dashed line is the average primary N/O plateau of dwarfs). At larger O/H or S/H, secondary N production begins to increase N/O. This is demonstrated by the empirical trend of stellar abundances (purple line); however, individual H II regions show a large dispersion.

by C16 or other traditional ICFs. In this case, the high-ionization H II regions (${\rm O^+/O}$ < 0.5) have S/O and Ar/O ratios that are generally under- and over-predicted, respectively, relative to the average, while the low-ionization H II regions (${\rm O^+/O}$ > 0.5) seem to be evenly dispersed about the mean. In general, no simple corrections to the ICFs are yet apparent. Instead, we will derive new ICFs for the CHAOS data using updated photoionization models in a future paper.

6.2. N/O versus Metallicity

Historically, N/O enrichment has been studied as a function of total oxygen abundance owing to the relative ease of integrated-light galaxy observations. In this context, the observed scaling of nitrogen with oxygen has long been understood as a combination of primary nitrogen plus a linearly increasing fraction of secondary nitrogen that comes to dominate the total N/O relationship at intermediate metallicities (e.g., Vila-Costas & Edmunds 1993; van Zee & Haynes 2006; Berg et al. 2012). Note that the scatter of the N/O-O/H relationship reported in previous studies is often significantly larger than that of the CHAOS N/O radial gradients (e.g., van Zee & Haynes 2006; Berg et al. 2012).

In Figure 13, we plot the N/O versus O/H values (left panel) and the N/O versus S/H value (right panel) for the CHAOS galaxies. For comparison, we also plot the empirical stellar N/ O-O/H relationship from Nicholls et al. (2017) and measured abundances for nearby metal-poor dwarf galaxies from Berg et al. (2019), which should compose a primary N plateau at low O/H and S/H values. Despite the tight N/O radial gradients observed for individual CHAOS galaxies (see Figure 9), large dispersion is seen in N/O when plotted versus O/H, similar to previous N/O-O/H studies. Guided by the stellar relationship (purple line), our data do follow the general trend of low N/O due to primary nitrogen at low oxygen abundances, followed by increasing N/O, presumably as secondary nitrogen becomes prominent, at larger O/H (12 + $\log(O/H) \gtrsim 8.2$). A similar trend is seen for N/O-S/H. Yet, individual galaxies in our sample clearly occupy different regions on the N/O versus O/ H and N/O versus S/H plots. Interestingly, the collective trend of the four galaxies appears to produce a stronger correlation between N/O with S/H than O/H. However, significant scatter

is seen for each galaxy, and the dispersions for the N/O-S/H and N/O-O/H relationships are consistent for each galaxy.

7. Understanding the Universal N/O Gradient

We now return to the universal N/O slope we found for the inner disks of CHAOS galaxies in Section 4.3. To understand the source of this trend, we must first understand how O and N are produced in these galaxies. Despite the ease at which both O and N emission are observed, discovering the origin of N is far more complex than O. Oxygen is primarily synthesized on short timescales by core-collapse SNe explosions of massive stars $(M \ge 9 M_{\odot})$; e.g., Heger et al. 2003). Nitrogen, on the other hand, is produced mainly by the CN branch of the CNO cycle, which can occur in the H-burning layer of both massive stars and intermediate-mass stars $(1M_{\odot} < M < 9M_{\odot})$. The slowest step of the CNO cycle is the conversion of ¹⁴N to ¹⁵O, which results in a pile up of ¹⁴N that can then be dredged-up by a convective layer. In metal-poor gas, the seed O and C needed for the CNO cycle may come from a He-burning phase. This path to N production is independent of the initial metal content of the star and so is referred to as "primary" nucleosynthesis. In more enriched gas at higher metallicities, the CNO cycle increases N production proportional to the initial metal composition (O and C) of the star. This type of N production is "secondary" nitrogen owing to its dependence on the metallicity of the star in which it was synthesized.

7.1. Offsets between Individual Galaxies

A schematic of nitrogen production for the CHAOS galaxies is shown in Figure 14. The radial gradient fits to the N/O, O/H, and S/H relationships are combined to produce the plotted N/O versus O/H relationship (middle panel) and N/O versus S/H (right panel) for each galaxy. The progressively increasing N/O values at smaller galactocentric distance correspond to increasing O/H abundance, as is expected for secondary N production. This results in parallel secondary N/O slopes for the N/O–S/H trends in Figure 14 and similar slopes in the N/O–O/H relationship for the three noninteracting galaxies. However, the individual relationships are distinct in two ways. First, each galaxy has a different primary plateau level,

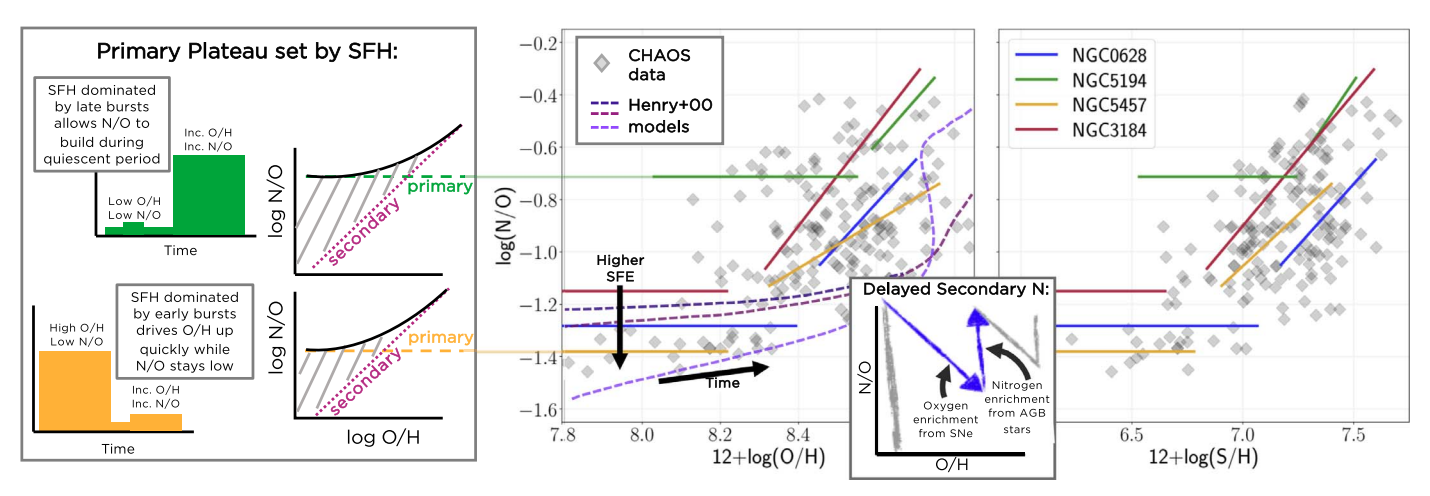


Figure 14. Schematic of how a galaxy's SFH affects its overall N/O-O/H relationship. Right panels: average N/O vs. O/H and S/H trends for the CHAOS sample. Secondary N slopes relative to S/H are similar for all four galaxies; however, the trends are offset from one another both vertically and horizontally. Left panel: two simple SFHs and their resulting N/O-O/H trends are shown. On top, an SFH with low SFE at early times allows N/O to build up, raising the primary plateau and shifting the transition to secondary dominance to the right. On the bottom, an SFH with high SFR at early times produces significant oxygen ahead of nitrogen production, setting a lower primary N/O plateau and O/H transition to secondary N. In addition to these differences, the lower-right inset plot shows that the N/O ratios of individual H II regions are sensitive to time since the onset of the most recent burst, driving scatter from the average relationships.

indicating large variations in their SFHs. Second, each galaxy has a different O/H transition value for when secondary N becomes important and turns the N/O curve upwards.

Henry et al. (2000) found that chemical evolution models differing only by their assumed star formation efficiencies (SFEs) produced a range of primary N/O plateaus. We illustrate the effect of varying the SFE by over-plotting the Henry et al. (2000) constant SFR models, where efficiency has been varied by a factor of 25, on our N/O versus O/H data in Figure 14. For low SFRs, the buildup of oxygen is slow and on the order of the lag time before intermediate-mass stars begin ejecting nitrogen. This allows a high N/O plateau to be established at low oxygen abundances (darkest purple curve). On the other hand, high SFRs early in the SFH form a large number of massive stars that produce greater levels of oxygen ahead of N enrichment, establishing a lower plateau (lightest purple curve) and shifting the entire N/O-O/H trend in Figure 14 to the right toward greater O/H. In between these scenarios, continuous star formation with roughly 250 Myr between bursts will result in N and O increasing in lockstep, dependent on the elemental yields. The coupling of the N/O plateau with galaxy SFH is also reported by cosmological hydrodynamical simulations of individual regions within spatially resolved galaxies (Vincenzo & Kobayashi 2018). In these simulations, asymptotic giant branch (AGB) stars contribute significant N at low O/H, but the exact value of the primary N/O plateau will vary from galaxy to galaxy according to the relative contributions from SNe and AGB stars, as determined by their galaxy formation time and SFH.

On the left-hand side of Figure 14, we extend the highest N/O plateau from NGC 5194 (green) and the lowest N/O plateau from NGC 5457 (yellow). Based on the above discussion, for the low N/O plateau of NGC 5457, we can put forth an SFH scenario in which the SFE was high early in the galaxy's evolution, allowing oxygen to build up from many bursts of star formation before nitrogen was returned from longer-lived intermediate-mass stars. Due to the higher level of nucleosynthetic products from massive stars, contributions from secondary nitrogen production may dominate over primary nitrogen production at relatively low O/H and S/H values. On

the other hand, the high N/O plateau of NGC 5194 could be due to an SFH in which low SFE at early times allows nitrogen production, although delayed, to keep pace with oxygen and sulfur production and enrich the ISM. Here, we assume low SFE to mean either constant, low SFRs or long quiescent periods between bursts. In this scenario, primary nitrogen production is the dominant mechanism until the galaxy reaches relatively high O/H. Note, however, that this is a very simplistic model where N/O is changing monotonically, in a hierarchical galaxy-building scenario that may not be true.

In summary, the primary N/O plateau sensitively probes the SFH of a galaxy, rather than being set by the ratio of N to O yields, and explains the large range of plateau levels observed for spiral galaxies. When this offset is accounted for, the N/O plateau then informs the primary N production yields, and the universal N/O gradient (see Figure 13) is a direct probe of the secondary N yields of intermediate-mass stars.

7.2. The Scatter in the N/O-O/H Relationship

In Figure 13, we plotted the N/O-O/H trend of the CHAOS galaxies and found large observed scatter in N/O for a given O/H. Given the tight correlations measured for the CHAOS N/O radial gradients (see Table 2), this scatter seems to be real. Previous works have suggested that some of this scatter may be due to the time-dependent nature of N/O production (i.e., a N/O "clock"; Garnett 1990; Pilyugin 1999; Henry et al. 2006). A directly observable effect of an aging ionizing stellar population is an increasing fraction of low- to high-ionization gas in the H II region (see, for example, how the shape of the ionizing continuum changes with age in Chisholm et al. 2019).

In Figure 15, we reproduce the N/O-O/H and N/O-S/H trends, color-coded by the O⁺/O ratio, or low-ionization fraction. Interestingly, the overall trend of increasing N/O seems to be ordered by ionization or age. In the bottom panels of Figure 15, we scale N/O (as was done in Section 4.3) by shifting the vertical offsets in order to remove differences in individual primary N/O plateaus and SFHs; yet, the overall trend of increasing N/O ordered by ionization remains. Nearly all of the CHAOS points now have N/O abundances that are lower relative to the scaled average stellar relationship of

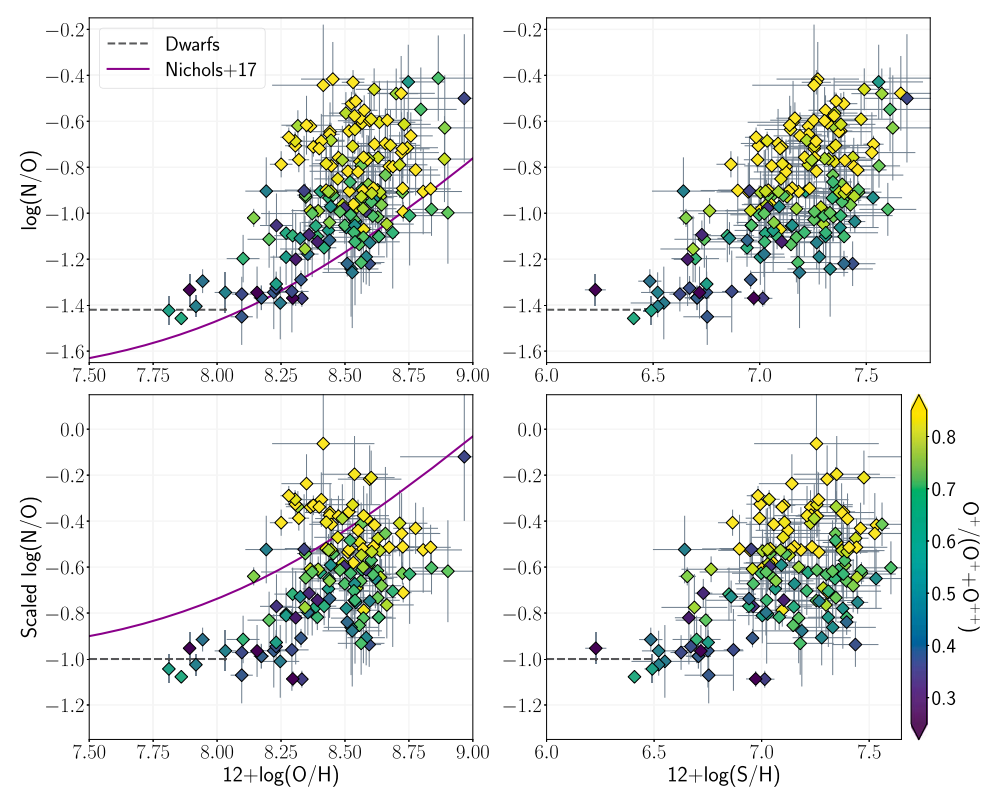


Figure 15. Top panels: N/O relationships for the CHAOS sample relative to O/H (left panel) and S/H (right panel). Bottom panels: scaled N/O trends relative to O/H (left panel) and S/H (right panel), where the differences in the SFHs of individual galaxies are removed by vertically shifting their primary N/O plateaus to align with log(N/O) = -1.0. For reference, the empirical stellar N/O-O/H trend from Nicholls et al. (2017) and metal-poor N/O plateau for local dwarfs (Berg et al. 2019) are also plotted. All plots are color-coded by the O⁺/O ratio, or low-ionization fraction, and show a persistent trend of increasing N/O with O⁺/O regardless of the N/O normalization.

Nicholls et al. (2017), suggesting that the physics of a recent burst of star formation has the effect of shifting the N/O abundances downward, as expected for a recent injection of newly synthesized oxygen. The regions with the lowest N/O also have high ionization. However, the standard N/O clock assumes regions with high N/O ratios have experienced a burst of star formation followed by a long quiescent period that allowed their gas to be enriched with N from slow-evolving stars after a few 100 Myr. Given the fact that typical H II regions are younger than $\sim \! \! 10 \, \mathrm{Myr}$, the simple delayed-release N clock hypothesis fails to explain our observed spread in N/O at a given O/H.

Alternatively, Coziol et al. (1999) suggested that high N/O ratios in starburst nucleus galaxies could result if N production occurs from a different, older population of intermediate-mass stars, such as would result from a sequence of bursts of star formation. Similarly, Berg et al. (2019) used chemical evolution models of dwarf galaxies to show that N/O was elevated in regions experiencing an extended duration of star formation (continuous star formation) up to 0.4 Gyr. Then, the overall effect of observing a large sample of H II regions with a range of luminosity-weighted average stellar population ages may be to produce the vertical spread in N/O at a given O/H seen in Figure 15.

Perhaps another reason for the increased scatter of the N/O–O/H trends relative to the N/O– R_g relationships is the possibility that N production is (or behaves as) a secondary function of the carbon abundance, rather than the typically assumed oxygen abundance (Henry et al. 2000). Recently,

Groh et al. (2019) investigated grids of stellar models at very low metallicities and found that the ratio between nitrogen and carbon abundances (N/C) remains generally unchanged for nonrotating stellar models during their main-sequence phase. However, the N/C production can increase by as much as $10-20\times$ in rotating models at the end of the main sequence. Thus, variations in stellar rotation speeds of different burst populations could result in significant effects on setting the low-metallicity stage. Additionally, Berg et al. (2019) showed that differential outflows of ISM gas can affect the primary C/O and N/O ratios. Since O and S are produced on different timescales than N, newly synthesized O and S may be preferentially lost in SNe winds, and these outflows may have a greater probability of escaping in the outer parts of the disk.

At higher metallicities, where the effects of stellar winds become more important, other authors have suggested that Wolf–Rayet stars can expel significant amounts of N resulting in local regions of N/O enrichment. For the CHAOS sample, however, we do not find any correlation in the N/O dispersion with the Wolf–Rayet features sometimes seen in the optical spectra.

Another hypothesis is that the dispersion in N/O could be explained if we are consistently underestimating the O/H abundance in low-ionization nebula. We have tested this hypothesis by looking at the offset in O/H abundance from the radial gradients relative to the secondary N/O radial gradient offsets and find some evidence of an anticorrelation, but it cannot explain all of the dispersion observed in N/O.

In summary, while we have observed a universal N/O gradient for the CHAOS galaxies that seems to be tied to the nucleosynthetic yields of N, we also observe a large dispersion when plotted relative to O/H. We have discussed several possible scenarios that could contribute to the N/O-O/H scatter, including extended star formation periods, differential outflows, and a secondary dependence on carbon abundance, but the importance of these contributions has not yet been determined. At this time, the source of the scatter in the N/O-O/H relationship remains an open question but with several promising possibilities for future study.

8. Conclusions

This work is the fourth paper in a series presenting the ongoing results of CHAOS (Berg et al. 2015), a project that is building a large database of direct abundance measurements spanning a large range in physical conditions in H II regions across the disks of nearby spiral galaxies. Previous results for NGCC 628, NGC 5194, and NGC 5457 have been reported individually in Papers I–III. Here, we present new LBT/MODS spectra of 52 H II regions in NGC 3184 to amass a high-quality, coherent sample of 175 direct abundances from the first four CHAOS galaxies.

Taking advantage of the direct T_e measurements from one or more auroral-line detections in 190 individual H II regions, we confirm our previous results that $T_e[S \text{ III}]$ and $T_e[N \text{ II}]$ provide robust measures of electron temperature in the metal-rich H II regions typical of spiral galaxies. Specifically, the $T_e[S \text{ III}] - T_e[N \text{ II}]$ trend, which characterizes the intermediate- to low-ionization zone temperatures, is especially tight for low-ionization H II regions (low $F_{\lambda 5007}/F_{\lambda 3727}$) with temperatures of $T_e \lesssim 8 \times 10^3 \text{ K}$. Unsurprisingly, we also find that the $T_e[O \text{ III}] - T_e[S \text{ III}]$ relationship is tightly correlated for high-ionization H II regions (high $F_{\lambda 5007}/F_{\lambda 3727}$). Given the observed dichotomy in temperature dispersions with ionization of the nebulae, we recommend new ionization-based temperature priorities and apply them to abundance determinations for the four CHAOS galaxies.

Prioritizing temperatures derived from [O III], [S III], or [N II] depending on the average ionization of the observed nebula, we measure the relative and absolute abundance trends of O, N, S, Ar, and Ne for the CHAOS sample. While the average α/O abundances of the CHAOS sample are consistent within the uncertainties of flat trends, we find evidence of systematic offsets that further depend on ionization and will likely require more sophisticated ICFs to correct. For O/H, we examine gradients normalized to both the isophotal radius (R_{25}) and the effective radius (R_e). In contrast to some recent empirical abundance studies, we do not find a universal direct O/H gradient when radius is plotted relative to R_e , but rather, we measure unique slopes ranging from -0.07 to -0.20 dex/ R_e .

Similarly, we examine the N/O gradient of our sample using both R_{25} and R_e . While each galaxy in our sample has a unique zero-point offset, interpreted here as different primary N/O plateaus set by differences in their SFHs, the secondary N/O slopes all appear to be the same. We, therefore, determine the first measurement of a universal N/O gradient of $\alpha_{\rm N/O} = -0.33~{\rm dex}/R_e$ for $R_g/R_e < 2.0$, where N is dominated by

secondary production and which can be used to constrain stellar vields.

As expected for two alpha elements, we find similar gradients for S/H and O/H for the CHAOS galaxies. These trends suggest that S/H can serve as a useful direct abundance diagnostic in the absence of O/H, such as data sets lacking the blue-wavelength coverage of [O III] $\lambda 4363$. However, direct S/H abundances will generally be significantly more uncertain than direct O/H abundances owing to the often large sulfur ICF uncertainties. Given that the observable ionic states of S probe lower ionization and excitation energies than O, S/H might be more appropriate for characterizing abundances in the moderate-to metal-rich H II regions of spiral galaxies. Further work is needed to better constrain S ICFs and quantify their uncertainties in order to improve S/H abundance determinations.

D.A.B. is supported by the United States National Science Foundation grant AST-1715284. We are grateful to the referee for detailed comments and thoughtful suggestions that greatly improved the scope and clarity of this paper.

This paper uses data taken with the MODS spectrographs built with funding from NSF grant AST-9987045 and the NSF Telescope System Instrumentation Program (TSIP), with additional funds from the Ohio Board of Regents and the Ohio State University Office of Research. This paper made use of the modsIDL spectral data reduction pipeline developed by K.V.C. in part with funds provided by NSF grant AST-1108693. This work was based in part on observations made with the Large Binocular Telescope (LBT). The LBT is an international collaboration among institutions in the United States, Italy, and Germany. The LBT Corporation partners are: the University of Arizona on behalf of the Arizona university system; the Istituto Nazionale di Astrofisica, Italy; the LBT Beteiligungsgesellschaft, Germany, representing the Max Planck Society, the Astrophysical Institute Potsdam, and Heidelberg University; the Ohio State University; and the Research Corporation, on behalf of the University of Notre Dame, the University of Minnesota, and the University of Virginia.

We are grateful to D. Fanning, J. X. Prochaska, J. Hennawi, C. Markwardt, M. Williams, and others who have developed the IDL libraries of which we have made use: coyote graphics, XIDL, idlutils, MPFIT, MPFITXY, and impro.

This research has made use of the NASA/IPAC Extragalactic Database (NED), which is operated by the Jet Propulsion Laboratory, California Institute of Technology, under contract with the National Aeronautics and Space Administration.

Appendix A CHAOS IV: NGC 3184 Measurements

In Tables A1–A3, we present details for the CHAOS optical MODS/LBT spectroscopic observations of NGC 3184 used in this work, the measured emission-line intensities, and the calculated ionic and total abundances.

Table A1
NGC 3184 MODS/LBT Observations

Н П	R.A.	Decl.	R_g	R/R_{25}	R_g	Offset		Aurora	l-line Dete	ections		Wolf
Region	(2000)	(2000)	(arcsec)	7 23	(kpc)	(arcsec)	[O III]	[N II]	[S III]	[O II]	[S II]	Rayet
Total Detections:							5	20	16	36	42	6
NGC 3184+2.7-0.5	10:18:17.0	41:25:26.52	2.10	0.009	0.12	+2.7, -0.5		1		1		
NGC 3184+24.4-11.6	10:18:19.0	41:25:15.42	27.11	0.122	1.54	+24.4, -11.6						
NGC 3184+27.0-10.7	10:18:19.2	41:25:16.27	29.29	0.132	1.66	+27.0, -10.7						
NGC 3184-2.7-47.5	10:18:16.6	41:24:39.55	47.18	0.213	2.68	-2.7, -47.5					✓	
NGC 3184-6.4-48.7	10:18:16.2	41:24:38.34	48.81	0.220	2.77	-6.4, -48.7						
NGC 3184-11.3-50.1	10:18:15.8	41:24:36.94	51.22	0.231	2.91	-11.3, -50.1				✓	✓	
NGC 3184-1.1+60.6	10:18:16.7	41:26:27.58	61.02	0.275	3.46	-1.1, +60.6					✓	
NGC 3184-19.4-62.1	10:18:15.1	41:24:24.89	65.15	0.293	3.70	-19.4, -62.1					✓	
NGC 3184-59.5-37.7	10:18:11.5	41:24:49.33	72.86	0.328	4.13	-59.5, -37.7		✓		✓	1	1
NGC 3184-70.7-27.1	10:18:10.5	41:24:59.91	78.94	0.356	4.48	-70.7, -27.1						
NGC 3184-70.7-27.1	10:18:10.5	41:24:59.91	78.94	0.356	4.48	-70.7, -27.1						
NGC 3184+51.2+60.4	10:18:21.4	41:26:27.44	80.47	0.362	4.56	+51.2, +60.4		✓		✓	/	
NGC 3184+78.4+34.5	10:18:23.8	41:26:01.51	88.11	0.397	5.00	+78.4, +34.5						
NGC 3184-15.0-88.4	10:18:15.5	41:23:58.57	89.56	0.403	5.08	-15.0, -88.4			✓			
NGC 3184-14.9-95.5	10:18:15.5	41:23:51.54	96.45	0.434	5.47	-14.9, -95.5		✓		✓	1	
NGC 3184+62.1-75.3	10:18:22.3	41:24:11.72	98.37	0.443	5.58	+62.1, -75.3					✓	
NGC 3184-71.1+67.7	10:18:10.5	41:26:34.64	100.99	0.455	5.73	-71.1, +67.7			✓	✓	✓	
NGC 3184-82.5+57.7	10:18:09.5	41:26:24.66	104.12	0.469	5.91	-82.5, +57.7		✓		✓	✓	
NGC 3184-90.9-43.7	10:18:08.7	41:24:43.30	104.69	0.472	5.94	-90.9, -43.7					/	
NGC 3184+62.1-86.8	10:18:22.3	41:24:00.14	107.41	0.484	6.09	+62.1, -86.8					/	
NGC 3184-94.2+43.8	10:18:08.4	41:26:10.74	108.04	0.487	6.13	-94.2 + 43.8				1	/	
NGC 3184+48.9+97.3	10:18:21.1	41:27:04.27	109.86	0.495	6.23	+48.9+97.3		1	/	1	/	
NGC 3184+107.7-15.4	10:18:26.4	41:25:11.53	112.32	0.506	6.37	+107.7, -15.4			/	/	/	
NGC 3184-67.3+87.1	10:18:10.8	41:26:54.10	112.44	0.506	6.38	-67.3, +87.1		1	/	1	/	1
NGC 3184-96.3+58.2	10:18:08.2	41:26:25.15	116.55	0.525	6.61	-96.3, +58.2					/	
NGC 3184+19.6-115.5	10:18:18.5	41:23:31.55	116.69	0.526	6.62	+19.6, -115.5		/		1	/	
NGC 3184+18.8-115.7	10:18:18.5	41:23:31.27	116.82	0.526	6.63	+18.8, -115.7		/		/	/	
NGC 3184+18.8-115.7	10:18:18.5	41:23:31.27	116.82	0.526	6.63	+18.8, -115.7		1		/	/	
NGC 3184+75.7+89.1	10:18:23.5	41:26:56.14	118.91	0.536	6.74	+75.7, +89.1		/	/	/	1	1
NGC 3184-72.8+91.3	10:18:10.3	41:26:58.26	119.27	0.537	6.77	-72.8, +91.3	1	1	/	/	/	/
NGC 3184-114.2+11.4	10:18:06.6	41:25:38.38	120.11	0.541	6.81	-114.2, +11.4					/	
NGC 3184+16.4+119.8	10:18:18.3	41:27:26.77	121.30	0.546	6.88	+16.4, +119.8		1	/	1	1	
NGC 3184+116.2-33.6	10:18:27.1	41:24:53.32	124.67	0.562	7.07	+116.2, -33.6				/	/	
NGC 3184-106.3+57.0	10:18:07.3	41:26:24.02	125.21	0.564	7.10	-106.3, +57.0				/	/	
NGC 3184+110.6-52.0	10:18:26.6	41:24:34.99	125.42	0.565	7.11	+110.6, -52.0			/	/	/	
NGC 3184-64.+105.8	10:18:11.1	41:27:12.74	125.68	0.566	7.13	-64.1, +105.8				/	/	
NGC 3184-96.7+74.3	10:18:08.2	41:26:41.26	125.74	0.566	7.13	-96.7, +74.3		/		1	/	
NGC 3184+8.2-132.1	10:18:17.5	41:23:14.87	131.95	0.594	7.48	+8.2, -132.1		/		/	/	
NGC 3184+94.9-91.5	10:18:25.2	41:23:55.46	133.75	0.602	7.59	+94.9, -91.5			/	/		/
NGC 3184+100.6+84.2	10:18:25.7	41:26:51.22	134.12	0.604	7.61	+100.6, +84.2		1	·	1	/	•
NGC 3184+14.9-139.6	10:18:18.1	41:23:07.40	139.95	0.630	7.94	+14.9, -139.6	/	•	1	/	/	/
NGC 3184+63.8+126.0	10:18:22.5	41:27:32.95	142.48	0.642	8.08	+63.8, +126.0	·		1	/	/	•
NGC 3184+123.8+76.5	10:18:27.8	41:26:43.47	149.52	0.674	8.48	+123.8, +76.5			1	/	/	
NGC 3184+70.7+132.5	10:18:23.1	41:27:39.49	151.65	0.683	8.60	+70.7, +132.5			•	/	/	
NGC 3184-145.8+8.7	10:18:03.8	41:25:35.64	152.62	0.687	8.66	-145.8, +8.7				•	•	
NGC 3184+41.9+148.8	10:18:20.5	41:27:55.80	155.31	0.700	8.81	+41.9, +148.8		1	1	/	/	
NGC 3184+80.0-148.2	10:18:23.9	41:22:58.76	169.18	0.762	9.60	+80.0, -148.2	1	-	/	/	/	
NGC 3184-117.5-120.0	10:18:25.9	41:23:26.93	171.67	0.702	9.74	-117.5, -120.0	•		•	1	√	
NGC 3184-110.6-127.6	10:18:07.0	41:23:19.41	172.10	0.775	9.76	-110.6, -127.6		1		1	<i>'</i>	
NGC 3184-93.3-142.3	10:18:08.5	41:23:04.68	172.45	0.777	9.78	-93.3, -142.3	/	•		/	/	
NGC 3184-169.8-22.2	10:18:01.7	41:25:04.72	178.74	0.805	10.14	-169.8, -22.2	•	/		/	√	
NGC 3184-172.5 -30.2	10:18:01.7	41:24:56.73	182.69	0.803	10.14	-109.6, -22.2 -172.5, -30.2	1	/	/	/	/	
	10.10.01.3	T1.27.30.73	102.07	0.023	10.50	112.3,-30.2	•					

Note. Observing logs for HII regions observed in NGC 3184 using MODS on the LBT on the UT dates of 2012 March 24 and 2013 January 6. Each field was observed over an integrated exposure time of 1200 s on clear nights, with, on average, ~ 1.100 seeing and airmasses less than 1.3. Slit ID, composed of the galaxy name and the offset in R.A. and decl., in arcseconds, from the central position listed in Table 1 is listed in Column 1. The R.A. and decl. of the individual HII regions are given in units of hours, minutes, and seconds, and degrees, arcminutes, and arcseconds, respectively, in columns 2 and 3. The de-projected distances of HII regions from the center of the galaxy in arcseconds, fraction of R_{25} , and in kiloparsecs are listed in the Columns 4–6. Columns 7–11 highlight which regions have [O III] $\lambda 4363$, [N II] $\lambda 5755$, [S III] $\lambda 6312$, [O II] $\lambda \lambda 7320$, 7330, and [S II] $\lambda \lambda 4068,4076$ auroral-line detections at the 3σ significance level. Finally, column 12 indicates which HII regions have Wolf–Rayet feature detections.

(This table is available in machine-readable form.)

 Table A2

 Emission-line Intensities and Equivalent Widths for LBT Observations of H II Regions in NGC 3184

			$I(\lambda)/$				
Ion	+2.7-0.5	+24.4-11.6	+27.0-10.7	-2.7-47.5	-6.4-48.7	-11.3-50.1	-1.1+60.6
H14 λ3721	0.015 ± 0.001	0.018 ± 0.004	0.024 ± 0.002	0.016 ± 0.002	0.019 ± 0.001	0.021 ± 0.001	0.009 ± 0.001
[O II] $\lambda 3727$	0.374 ± 0.007	0.844 ± 0.019	0.839 ± 0.014	0.745 ± 0.137	0.672 ± 0.014	0.678 ± 0.011	0.566 ± 0.010
H13 λ 3734	0.018 ± 0.001	0.022 ± 0.004	0.029 ± 0.003	0.020 ± 0.003	0.024 ± 0.002	0.026 ± 0.001	0.011 ± 0.001
H12 λ 3750	0.003 ± 0.005	0.021 ± 0.004	0.030 ± 0.008	0.050 ± 0.007	0.024 ± 0.005	0.043 ± 0.002	0.005 ± 0.002
H11 λ 3770	0.053 ± 0.004	0.040 ± 0.007	0.076 ± 0.006	0.050 ± 0.005	0.031 ± 0.002	0.048 ± 0.001	•••
H10 λ 3797	0.039 ± 0.003	0.048 ± 0.010	0.062 ± 0.006	0.043 ± 0.006	0.051 ± 0.003	0.056 ± 0.003	0.025 ± 0.002
He I λ 3819	0.012 ± 0.002	0.036 ± 0.007	0.017 ± 0.006	0.040 ± 0.007	0.005 ± 0.002	0.010 ± 0.001	•••
H9 $\lambda 3835$	0.073 ± 0.001	0.085 ± 0.002	0.099 ± 0.006	0.057 ± 0.011	0.071 ± 0.005	0.073 ± 0.002	0.026 ± 0.003
[Ne III] $\lambda 3868$	0.024 ± 0.003	0.011 ± 0.005	•••	0.044 ± 0.008	0.008 ± 0.002	0.003 ± 0.002	0.011 ± 0.002
He I $\lambda 3888$	0.090 ± 0.004	0.032 ± 0.004	0.013 ± 0.006	0.046 ± 0.015	0.025 ± 0.003	0.037 ± 0.002	0.033 ± 0.002
H8 $\lambda 3889$	0.076 ± 0.005	0.089 ± 0.018	0.118 ± 0.011	0.081 ± 0.012	0.098 ± 0.006	0.108 ± 0.006	0.049 ± 0.003
He I $\lambda 3964$	0.004 ± 0.005	0.009 ± 0.006	•••	0.013 ± 0.012	0.002 ± 0.004	0.003 ± 0.002	•••
[Ne III] $\lambda 3967$	0.072 ± 0.005	0.030 ± 0.005	0.007 ± 0.005	0.056 ± 0.013	•••	0.025 ± 0.002	0.031 ± 0.004
H7 $\lambda 3970$	0.114 ± 0.007	0.129 ± 0.026	0.173 ± 0.017	0.119 ± 0.018	0.144 ± 0.009	0.161 ± 0.009	0.074 ± 0.005
[Ne III] $\lambda 4011$	•••	0.007 ± 0.006	•••	0.007 ± 0.004	0.002 ± 0.002	0.005 ± 0.003	0.003 ± 0.001
He I $\lambda 4026$	0.005 ± 0.002	•••	•••	0.034 ± 0.003	0.012 ± 0.002	0.014 ± 0.001	•••
[S II] λ4068	0.003 ± 0.003	0.005 ± 0.002	•••	0.023 ± 0.005	0.008 ± 0.003	0.012 ± 0.002	0.014 ± 0.002
[S II] $\lambda 4076$	0.005 ± 0.005	0.007 ± 0.003	•••	0.017 ± 0.001	0.010 ± 0.001	0.016 ± 0.003	0.010 ± 0.002
H $\delta \lambda 4101$	0.314 ± 0.006	0.234 ± 0.007	0.214 ± 0.006	0.241 ± 0.007	0.238 ± 0.007	0.289 ± 0.004	0.188 ± 0.007
He I λ 4120	0.018 ± 0.005	•••	0.007 ± 0.004	0.009 ± 0.003	0.001 ± 0.001	0.002 ± 0.001	•••
He I λ 4143	0.001 ± 0.003	•••	•••	0.005 ± 0.004	•••	0.006 ± 0.001	•••
H $\gamma \lambda 4340$	0.476 ± 0.007	0.452 ± 0.012	0.434 ± 0.011	0.437 ± 0.011	0.436 ± 0.013	0.483 ± 0.007	0.409 ± 0.009
[O III] $\lambda 4363$	•••	•••	•••	0.010 ± 0.004	0.006 ± 0.004	•••	0.003 ± 0.003
He I λ4387		0.004 ± 0.001	0.004 ± 0.004		0.003 ± 0.001	0.004 ± 0.001	
He I λ4471	0.014 ± 0.002	0.004 ± 0.003	0.021 ± 0.004	0.032 ± 0.002	0.018 ± 0.002	0.016 ± 0.001	0.001 ± 0.001
[Fe III] λ4658	0.008 ± 0.001	0.023 ± 0.003			0.001 ± 0.001	•••	0.009 ± 0.001
He II $\lambda 4686$	0.011 ± 0.001	0.014 ± 0.001	0.006 ± 0.004	0.006 ± 0.003	0.003 ± 0.001		0.003 ± 0.001
$H\beta \lambda 4861$	1.000 ± 0.006	1.000 ± 0.021	1.000 ± 0.018	1.000 ± 0.020	1.000 ± 0.014	1.000 ± 0.008	1.000 ± 0.012
He I λ4921	0.009 ± 0.002	0.015 ± 0.012	0.018 ± 0.010	0.004 ± 0.011		0.007 ± 0.004	0.001 ± 0.004
[O III] λ4959	0.050 ± 0.002	0.033 ± 0.012	0.027 ± 0.011	0.031 ± 0.012	0.008 ± 0.007	0.016 ± 0.004	0.025 ± 0.004
[O III] λ5007	0.133 ± 0.002	0.075 ± 0.013	0.050 ± 0.010	0.121 ± 0.011	0.034 ± 0.006	0.054 ± 0.004	0.058 ± 0.004
He I $\lambda 5015$	0.009 ± 0.002	0.003 ± 0.011	0.014 ± 0.009	0.014 ± 0.011	0.011 ± 0.006	0.008 ± 0.004	0.004 ± 0.004
[N II] λ5755 He I λ5876	0.002 ± 0.001	0.004 ± 0.008	0.008 ± 0.007	0.071 0.007	0.047 0.004	0.007 ± 0.003 0.075 ± 0.003	0.001 ± 0.002
	0.068 ± 0.001	$\begin{array}{c} 0.132 \pm 0.009 \\ 0.032 \pm 0.007 \end{array}$	0.080 ± 0.007	0.071 ± 0.007 0.010 ± 0.005	0.047 ± 0.004 0.019 ± 0.003		0.036 ± 0.002
[O 1] $\lambda 6300$	0.030 ± 0.001 0.002 ± 0.001	0.032 ± 0.007	$\begin{array}{c} 0.017 \pm 0.005 \\ 0.011 \pm 0.005 \end{array}$	0.010 ± 0.003	0.019 ± 0.003	0.023 ± 0.003 0.003 ± 0.002	$\begin{array}{c} 0.006 \pm 0.002 \\ 0.002 \pm 0.002 \end{array}$
[S III] λ6312 [O 1] λ6363	0.002 ± 0.001 0.002 ± 0.001		0.011 ± 0.005 0.022 ± 0.005	0.006 ± 0.005	0.009 ± 0.003	0.003 ± 0.002 0.008 ± 0.002	0.002 ± 0.002
[N II] λ6548	0.002 ± 0.001 0.272 ± 0.012	0.409 ± 0.017	0.022 ± 0.003 0.350 ± 0.009	0.368 ± 0.003	0.303 ± 0.003 0.303 ± 0.008	0.320 ± 0.002	0.269 ± 0.006
$H\alpha \lambda 6563$	3.123 ± 0.070	3.020 ± 0.017	0.350 ± 0.009 2.950 ± 0.065	2.929 ± 0.091	2.993 ± 0.008	3.179 ± 0.049	2.795 ± 0.000
N II] λ6584	0.850 ± 0.020	1.245 ± 0.039	1.119 ± 0.026	1.164 ± 0.035	0.951 ± 0.026	1.000 ± 0.016	0.847 ± 0.020
He I $\lambda 6678$	0.030 ± 0.020 0.016 ± 0.001	0.023 ± 0.001	0.018 ± 0.002	0.021 ± 0.001	0.931 ± 0.020 0.020 ± 0.001	0.018 ± 0.001	0.047 ± 0.020 0.012 ± 0.001
[S II] $\lambda 6717$	0.302 ± 0.008	0.301 ± 0.009	0.018 ± 0.002 0.295 ± 0.007	0.283 ± 0.010	0.352 ± 0.001	0.359 ± 0.007	0.317 ± 0.008
[S II] λ6731	0.262 ± 0.006 0.262 ± 0.006	0.220 ± 0.007	0.218 ± 0.007	0.207 ± 0.007	0.332 ± 0.010 0.247 ± 0.007	0.257 ± 0.007 0.257 ± 0.004	0.228 ± 0.005
He I $\lambda 7065$	0.002 ± 0.000 0.009 ± 0.001	0.009 ± 0.003	0.006 ± 0.003	0.012 ± 0.004	0.002 ± 0.001	0.006 ± 0.002	0.006 ± 0.002
[Ar III] $\lambda 7135$	0.009 ± 0.001 0.010 ± 0.001	0.009 ± 0.003 0.019 ± 0.002	0.000 ± 0.004 0.019 ± 0.004	0.012 ± 0.004 0.027 ± 0.004	0.002 ± 0.001 0.004 ± 0.001	0.000 ± 0.002 0.011 ± 0.002	0.000 ± 0.002 0.010 ± 0.002
[O II] $\lambda 7320$	0.010 ± 0.001 0.004 ± 0.001	0.015 ± 0.002 0.015 ± 0.010	0.017 ± 0.004 0.002 ± 0.004	0.027 ± 0.004 0.010 ± 0.005	0.004 ± 0.001 0.005 ± 0.001	0.0011 ± 0.002 0.004 ± 0.002	0.010 ± 0.002 0.006 ± 0.002
[O II] $\lambda 7320$		0.015 ± 0.010 0.015 ± 0.010	0.002 ± 0.004 0.014 ± 0.004	0.002 ± 0.003	0.003 ± 0.001 0.001 ± 0.001	0.009 ± 0.002	0.003 ± 0.002 0.003 ± 0.002
[Ar III] $\lambda 7751$	0.011 ± 0.001	0.013 ± 0.010 0.013 ± 0.003	0.003 ± 0.001	0.002 ± 0.004 0.004 ± 0.002	0.001 ± 0.001 0.008 ± 0.002		0.005 ± 0.002 0.005 ± 0.003
P13 λ8665		0.003 ± 0.005 0.001 ± 0.005	0.003 ± 0.001 0.011 ± 0.013	0.001 ± 0.002 0.012 ± 0.015	0.006 ± 0.002 0.006 ± 0.007	•••	0.003 ± 0.009 0.012 ± 0.009
P12 λ8750	0.019 ± 0.005	0.051 ± 0.008	0.025 ± 0.018	0.012 ± 0.013 0.023 ± 0.021	0.003 ± 0.007 0.013 ± 0.008	2.520 ± 0.022	0.012 ± 0.005 0.027 ± 0.012
P11 λ8862	0.015 ± 0.005 0.025 ± 0.005		0.025 ± 0.016 0.001 ± 0.015	0.025 ± 0.021 0.025 ± 0.019	0.013 ± 0.008 0.011 ± 0.008		0.027 ± 0.012 0.015 ± 0.010
P10 λ9015	0.023 ± 0.003 0.044 ± 0.002	0.014 ± 0.004	0.001 ± 0.013 0.017 ± 0.004	0.029 ± 0.019 0.019 ± 0.006	0.011 ± 0.003 0.018 ± 0.003	0.017 ± 0.003	0.020 ± 0.003
[S III] λ9069	0.044 ± 0.002 0.097 ± 0.002	0.014 ± 0.004 0.111 ± 0.005	0.017 ± 0.004 0.089 ± 0.004	0.015 ± 0.006 0.155 ± 0.006	0.018 ± 0.003 0.088 ± 0.004	0.017 ± 0.003 0.118 ± 0.004	0.020 ± 0.003 0.079 ± 0.003
P9 λ9229	0.028 ± 0.002	0.014 ± 0.003	0.009 ± 0.004 0.022 ± 0.004	0.027 ± 0.005	0.000 ± 0.004 0.019 ± 0.004	0.023 ± 0.003	0.079 ± 0.003 0.022 ± 0.003
[S III] λ9532	0.261 ± 0.004	0.247 ± 0.009	0.259 ± 0.008	0.431 ± 0.012	0.223 ± 0.007	0.316 ± 0.008	0.206 ± 0.005
P8 λ9546	0.020 ± 0.003	0.076 ± 0.008	0.037 ± 0.008	0.081 ± 0.012 0.081 ± 0.011	0.076 ± 0.007	0.099 ± 0.007	0.041 ± 0.006
E(B-V)	0.161 ± 0.013	0.698 ± 0.020	0.594 ± 0.016	0.522 ± 0.020	0.463 ± 0.018	0.238 ± 0.010	0.205 ± 0.019
$F_{H\beta}$	119.73 ± 0.40	39.25 ± 0.55	44.83 ± 0.62	32.25 ± 0.42	43.70 ± 0.41	47.51 ± 0.20	31.11 ± 0.31
- <i>πρ</i>	117.7.0 ± 0.10	27.20 ± 0.00	± 0.02	22.22 ± 0.12	± 0.11	± 0.20	

Note. Reddening-corrected emission-line intensities relative to H β . The last two rows list the E(B-V) reddening and H β line flux, given in units of 10^{-16} ergs s⁻¹ cm⁻². Note that previous CHAOS papers incorrectly reported the E(B-V) quantities as $C_{H\beta}$, whereas the values listed here are actually E(B-V). (This table is available in its entirety in machine-readable form.)

Table A3
Ionic and Total Abundances for LBT Observations of NGC 3184

Property	+2.7-0.5	-59.5-37.7	+51.2+60.4	-15.0-88.4	-14.9-95.5	-71.1+67.7
$T_e[SII]$ (K)		5700 ± 400	8200 ± 400		14000 ± 400	7600 ± 400
$T_e[NII](K)$	6000 ± 1700	6300 ± 1700	6500 ± 1700		6500 ± 1700	
$T_e[OII](K)$	8500 ± 400	7800 ± 400	12500 ± 400		6800 ± 400	7600 ± 400
$T_e[SIII]$ (K)	•••	•••	•••	6400 ± 600		6800 ± 600
T_e [O III] (K)						
$n_{e,m} \; (\text{cm}^{-3})$	210 ± 10	60 ± 10	50 ± 10	29500 ± 0	30 ± 10	40 ± 10
$T_{e,\text{low}}$ (K)	6000 ± 900	6300 ± 300	6500 ± 500	7300 ± 1000	6500 ± 700	7600 ± 500
$T_{e,\text{int.}}$ (K)	4700 ± 1100	5200 ± 400	5400 ± 700	6400 ± 1300	5400 ± 900	6800 ± 600
$T_{e, \text{high}}$ (K)	4800 ± 1200	5300 ± 400	5600 ± 700	6900 ± 1000	5500 ± 1000	7200 ± 500
$n_{e,U} \; (\text{cm}^{-3})$	100 ± 10	60 ± 10	50 ± 10	100 ± 10	30 ± 10	40 ± 10
O^+/H^+ (10 ⁻⁵)	34.9 ± 26.8	33.4 ± 8.9	29.1 ± 11.6	23.6 ± 15.1	56.4 ± 32.0	19.1 ± 5.6
O^{+2}/H^+ (10 ⁻⁵)	57.7 ± 67.3	6.6 ± 2.9	5.4 ± 3.3	2.4 ± 1.4	23.5 ± 19.7	3.2 ± 0.9
$12 + \log(O/H)$	8.967 ± 0.251	8.602 ± 0.092	8.537 ± 0.130	8.415 ± 0.200	8.902 ± 0.167	8.350 ± 0.098
$N^{+}/H^{+}(10^{-6})$	110.4 ± 52.5	85.7 ± 13.7	77.2 ± 18.7	85.2 ± 45.6	56.6 ± 19.7	46.2 ± 8.2
N ICF	2.651 ± 2.904	1.198 ± 0.426	1.185 ± 0.629	1.100 ± 0.955	1.417 ± 1.044	1.169 ± 0.453
log(N/H)	8.466 ± 0.341	8.012 ± 0.143	7.961 ± 0.200	7.972 ± 0.305	7.904 ± 0.259	7.733 ± 0.154
log(N/O)	-0.500 ± 0.279	-0.591 ± 0.118	-0.576 ± 0.166	-0.443 ± 0.264	-0.998 ± 0.222	-0.617 ± 0.128
$S^+/H^+ (10^{-7})$	86.6 ± 39.9	54.9 ± 8.5	47.7 ± 11.1	41.3 ± 15.9	44.4 ± 15.0	31.0 ± 5.3
$S^{+2}/H^+ (10^{-7})$	227.1 ± 173.5	194.6 ± 44.4	140.8 ± 46.3	122.1 ± 60.9	106.3 ± 52.9	87.2 ± 19.7
S ICF	1.564 ± 0.156	1.198 ± 0.426	1.185 ± 0.629	1.100 ± 0.955	1.417 ± 1.044	1.169 ± 0.453
log(S/H)	7.691 ± 0.198	7.476 ± 0.146	7.349 ± 0.201	7.255 ± 0.290	7.330 ± 0.261	7.141 ± 0.154
log(S/O)	-1.276 ± 0.295	-1.127 ± 0.165	-1.188 ± 0.226	-1.160 ± 0.325	-1.573 ± 0.289	-1.209 ± 0.174
$Ne^{+2}/H^+ (10^{-6})$	1184.8 ± 1518.8	17.1 ± 8.8	17.1 ± 13.3		167.9 ± 166.8	6.7 ± 2.2
Ne ICF	1.627 ± 2.256	2.116 ± 3.016	2.178 ± 4.486	2.890 ± 9.186	1.601 ± 3.266	2.273 ± 2.590
log(Ne/H)	9.279 ± 0.463	8.015 ± 0.235	8.039 ± 0.312	•••	8.756 ± 0.377	7.670 ± 0.175
log(Ne/O)	0.313 ± 0.394	-0.587 ± 0.182	-0.498 ± 0.239		-0.146 ± 0.308	-0.680 ± 0.141
$Ar^{+2}/H^+ (10^{-7})$	20.6 ± 18.6	12.7 ± 3.5	11.8 ± 4.9	12.7 ± 9.0	12.4 ± 7.5	8.8 ± 2.3
Ar ICF	1.627 ± 0.163	2.116 ± 0.212	2.178 ± 0.218	2.890 ± 0.289	1.601 ± 0.160	2.273 ± 0.227
log(Ar/H)	6.525 ± 0.281	6.430 ± 0.113	6.411 ± 0.154	6.564 ± 0.235	6.296 ± 0.207	6.299 ± 0.108
log(Ar/O)	-2.441 ± 0.343	-2.173 ± 0.139	-2.127 ± 0.190	-1.852 ± 0.284	-2.606 ± 0.248	-2.051 ± 0.140

Note. Electron temperatures and ionic and total abundances for objects with an [O III] $\lambda4363$, [N II] $\lambda5755$, or [S III] $\lambda6312$ line signal-to-noise ratio of 3σ or greater. Electron temperatures for different ionization zones were calculated using the [O III] $(\lambda4959 + \lambda5007)/\lambda4363$, [N II] $(\lambda6548 + \lambda6584)/\lambda5755$, or the [S III] $(\lambda9069 + \lambda9532)/\lambda6312$ diagnostic line ratios, following the T_e prioritization presented in this work.

(This table is available in its entirety in machine-readable form.)

Appendix B Re-derived Relative and Total Abundances for CHAOS Galaxies

The gradients for NGC 5457 presented in C16 focused on abundances derived using $T_e[{\rm O\,III}]$ for the purpose of comparing to previously reported trends in the literature that also used $T_e[{\rm O\,III}]$ measurements. In contrast, NGC 628 and NGC 5194 used the T_e prioritization rules recommended

by B15. Here, in Tables B1–B3, we present recalculated ionic and total abundances for all three previously studied CHAOS galaxies: NGC 628, NGC 5194, and NGC 5457. These updated values adopt the ionization-based temperature selection criteria proposed in this work in order to form a uniform, coherent sample of 190 CHAOS H II regions with direct electron temperature measurements. This is the largest sample of its kind to date.

$H\alpha$ Region	$12 + \log(O/H)$	log(N/O)	log(S/O)	log(Ar/O)	log(Ne/O)
NGC 628-35.9+57.7	8.52 ± 0.04	-0.64 ± 0.05	-1.14 ± 0.07	-1.90 ± 0.06	
NGC 628+49.8+48.7	8.64 ± 0.04	-0.76 ± 0.05	-1.20 ± 0.07	-2.03 ± 0.06	-1.02 ± 0.03
NGC 628-73.1-27.3	8.37 ± 0.02	-0.62 ± 0.02	-1.14 ± 0.03	-2.03 ± 0.05	-0.73 ± 0.04
NGC 628-76.2+22.9	8.40 ± 0.08	-0.63 ± 0.11	-1.02 ± 0.15	-1.92 ± 0.13	
NGC 628-36.8-73.4	8.43 ± 0.04	-0.65 ± 0.05	-1.21 ± 0.07	-2.15 ± 0.06	
NGC 628+68.5+53.4	8.32 ± 0.05	-0.62 ± 0.07	-0.97 ± 0.08	-1.89 ± 0.07	-0.67 ± 0.04
NGC 628+81.6-32.3	8.62 ± 0.03	-0.70 ± 0.04	-1.08 ± 0.06	-1.89 ± 0.06	
NGC 628-68.5+61.7	8.67 ± 0.09	-0.78 ± 0.12	-1.22 ± 0.16	-2.02 ± 0.11	
NGC 628+76.9-49.6	8.74 ± 0.14	-0.74 ± 0.17	-1.21 ± 0.23	-1.96 ± 0.16	
NGC 628-13.1+107.5	8.59 ± 0.01	-0.87 ± 0.02	-1.20 ± 0.03	-2.02 ± 0.04	-0.81 ± 0.01
NGC 628+53.5-104.0	8.47 ± 0.13	-0.78 ± 0.17	-1.23 ± 0.23	-2.09 ± 0.18	
NGC 628-35.7+119.6	8.73 ± 0.03	-0.91 ± 0.05	-1.26 ± 0.06	-2.15 ± 0.05	-0.83 ± 0.02
NGC 628-20.3+124.6	8.63 ± 0.01	-0.90 ± 0.02	-1.17 ± 0.03	-2.07 ± 0.04	-0.87 ± 0.01
NGC 628-59.6-111.6	8.58 ± 0.04	-0.78 ± 0.06	-1.23 ± 0.08	-2.07 ± 0.06	-0.73 ± 0.03
NGC 628+61.2+113.5	8.73 ± 0.03	-0.99 ± 0.04	-1.42 ± 0.06	-2.13 ± 0.05	-1.03 ± 0.03
NGC 628+42.6-120.7	8.62 ± 0.06	-0.92 ± 0.08	-1.18 ± 0.10	-2.10 ± 0.07	-0.68 ± 0.04
NGC 628+131.9+18.5	8.56 ± 0.02	-0.89 ± 0.03	-1.20 ± 0.03	-2.19 ± 0.05	-0.65 ± 0.02
NGC 628+125.4-62.4	8.64 ± 0.11	-1.04 ± 0.15	-1.36 ± 0.19	-2.16 ± 0.15	
NGC 628-130.9+71.8	8.55 ± 0.02	-0.97 ± 0.03	-1.26 ± 0.04	-2.13 ± 0.05	-0.82 ± 0.02
NGC 628+131.7-70.2	8.57 ± 0.05	-1.07 ± 0.07	-1.48 ± 0.09	-2.24 ± 0.08	-0.67 ± 0.07
NGC 628+151.0+22.3	8.61 ± 0.07	-0.93 ± 0.12	-1.09 ± 0.14	-2.10 ± 0.10	-0.87 ± 0.09
NGC 628-157.9-0.3	8.45 ± 0.09	-0.94 ± 0.14	-1.11 ± 0.16	-2.03 ± 0.12	
NGC 628-24.5-155.6	8.62 ± 0.06	-1.01 ± 0.09	-1.29 ± 0.12	-2.17 ± 0.10	-0.75 ± 0.10
NGC 628-129.8+94.7	8.57 ± 0.05	-0.95 ± 0.08	-1.17 ± 0.10	-2.19 ± 0.07	-0.61 ± 0.03
NGC 628+140.3+82.0	8.35 ± 0.03	-0.93 ± 0.04	-1.29 ± 0.06	-2.16 ± 0.06	-0.99 ± 0.04
NGC 628-42.8-158.2	8.54 ± 0.03	-1.03 ± 0.05	-1.09 ± 0.06	-2.15 ± 0.05	-0.78 ± 0.02
NGC 628+147.9-71.8	8.55 ± 0.11	-1.03 ± 0.15	-1.29 ± 0.20	-2.19 ± 0.15	-0.75 ± 0.19
NGC 628+163.5+64.4	8.65 ± 0.08	-0.97 ± 0.12	-1.22 ± 0.15	-2.15 ± 0.10	-0.77 ± 0.06
NGC 628-4.5+185.6	8.39 ± 0.03	-1.10 ± 0.06	-1.31 ± 0.07	-2.21 ± 0.05	-0.84 ± 0.02
NGC 628+176.7-50.0	8.41 ± 0.08	-0.91 ± 0.12	-1.19 ± 0.16	-2.15 ± 0.12	-0.68 ± 0.13
NGC 628-76.2-171.8	8.63 ± 0.05	-1.10 ± 0.08	-1.32 ± 0.10	-2.30 ± 0.09	-0.52 ± 0.09
NGC 628+31.6-191.1	8.55 ± 0.13	-1.09 ± 0.20	-1.38 ± 0.23	-2.25 ± 0.14	-0.79 ± 0.06
NGC 628-200.6-4.2	8.53 ± 0.13 8.53 ± 0.10	-1.07 ± 0.20 -1.07 ± 0.17	-1.15 ± 0.19	-2.11 ± 0.12	-0.75 ± 0.00 -0.85 ± 0.11
NGC 628-184.7+83.4	8.63 ± 0.10 8.63 ± 0.01	-1.07 ± 0.17 -1.10 ± 0.02	-1.13 ± 0.17 -1.24 ± 0.03	-2.11 ± 0.12 -2.20 ± 0.04	-0.70 ± 0.01
NGC 628-206.5-25.7	8.60 ± 0.05	-1.10 ± 0.02 -1.22 ± 0.11	-1.24 ± 0.03 -1.16 ± 0.12	-2.20 ± 0.04 -2.14 ± 0.10	-0.70 ± 0.01 -0.61 ± 0.09
NGC 628-90.1+190.2	8.56 ± 0.01	-1.22 ± 0.11 -1.14 ± 0.01	-1.10 ± 0.12 -1.41 ± 0.02	-2.14 ± 0.10 -2.24 ± 0.04	-0.01 ± 0.09 -0.79 ± 0.01
NGC 628-168.2+150.8	8.27 ± 0.01	-1.14 ± 0.01 -1.09 ± 0.02	-1.41 ± 0.02 -1.24 ± 0.02	-2.24 ± 0.04 -2.23 ± 0.04	-0.79 ± 0.01 -0.76 ± 0.02
NGC 628+232.7+6.6	8.58 ± 0.07	-1.09 ± 0.02 -1.19 ± 0.12	-1.24 ± 0.02 -1.30 ± 0.15	-2.23 ± 0.04 -2.31 ± 0.12	-0.76 ± 0.02 -0.56 ± 0.13
NGC 628+237.6+3.0	8.58 ± 0.10	-1.23 ± 0.16	-1.39 ± 0.20	-2.36 ± 0.16	-0.57 ± 0.16
NGC 628+254.3-42.8	8.39 ± 0.04	-1.05 ± 0.07	-1.24 ± 0.09	-2.44 ± 0.08	-0.49 ± 0.07
NGC 628+252.1-92.1	8.24 ± 0.06	-1.05 ± 0.14	-1.26 ± 0.09	-2.17 ± 0.10	-0.61 ± 0.10
NGC 628+261.9-99.7	8.21 ± 0.09	-1.12 ± 0.13	-1.47 ± 0.17	-2.43 ± 0.13	-0.40 ± 0.14
NGC 628+265.2-102.2	8.10 ± 0.07	-1.20 ± 0.11	-1.41 ± 0.13	-2.26 ± 0.11	
NGC 628+289.9-17.4	8.33 ± 0.02	-1.37 ± 0.04	-1.32 ± 0.05	-2.11 ± 0.05	-0.67 ± 0.04
NGC 628+298.4+12.3	8.30 ± 0.02	-1.37 ± 0.04	-1.32 ± 0.05	-1.99 ± 0.05	-0.64 ± 0.03

(This table is available in machine-readable form.)

$H\alpha$ Region	$12 + \log(O/H)$	log(N/O)	log(S/O)	log(Ar/O)	log(Ne/O)
NGC 5194-4.3+63.3	8.73 ± 0.14	-0.43 ± 0.16	-1.19 ± 0.24	-2.56 ± 0.21	•••
NGC 5194-33.2+58.0	8.89 ± 0.16	-0.42 ± 0.19	-1.02 ± 0.28	-2.06 ± 0.24	•••
NGC 5194-62.2+50.3	8.79 ± 0.13	-0.55 ± 0.17	-1.19 ± 0.24	-2.08 ± 0.20	
NGC 5194+75.5-28.7	8.47 ± 0.12	-0.42 ± 0.15	-1.18 ± 0.21	-2.04 ± 0.17	•••
NGC 5194+96.1+16.8	8.70 ± 0.09	-0.48 ± 0.11	-1.13 ± 0.16	-2.06 ± 0.14	
NGC 5194+91.0+69.0	8.72 ± 0.13	-0.48 ± 0.16	-1.07 ± 0.21	-1.87 ± 0.15	•••
NGC 5194-86.5-79.4	8.54 ± 0.04	-0.43 ± 0.05	-1.27 ± 0.08	-2.24 ± 0.08	•••
NGC 5194-22.5+122.8	8.77 ± 0.15	-0.58 ± 0.20	-1.25 ± 0.27	-2.15 ± 0.22	•••
NGC 5194+112.7+37.7	8.61 ± 0.08	-0.46 ± 0.10	-1.12 ± 0.14	-2.06 ± 0.12	•••
NGC 5194+76.6+96.3	8.77 ± 0.10	-0.63 ± 0.14	-1.36 ± 0.18	-2.30 ± 0.16	•••
NGC 5194-97.0-78.4	8.52 ± 0.03	-0.52 ± 0.05	-1.13 ± 0.07	-1.98 ± 0.06	

Table B2 (Continued)

$H\alpha$ Region	$12 + \log(O/H)$	log(N/O)	log(S/O)	log(Ar/O)	log(Ne/O)
NGC 5194-3.0+131.9	8.64 ± 0.11	-0.69 ± 0.14	-1.55 ± 0.19	-2.19 ± 0.14	-0.70 ± 0.12
NGC 5194-57.2+118.2	8.53 ± 0.08	-0.63 ± 0.10	-1.38 ± 0.14	-2.17 ± 0.11	-0.76 ± 0.11
NGC 5194-78.9+107.4	8.87 ± 0.15	-0.76 ± 0.19	-1.56 ± 0.25	-2.27 ± 0.21	
NGC 5194-82.0-102.7	8.59 ± 0.12	-0.59 ± 0.15	-1.47 ± 0.21	-2.68 ± 0.18	
NGC 5194-66.6+122.9	8.69 ± 0.09	-0.80 ± 0.12	-1.56 ± 0.16	-2.09 ± 0.13	
NGC 5194+56.8+126.5	8.68 ± 0.14	-0.60 ± 0.17	-1.42 ± 0.23	-2.28 ± 0.20	
NGC 5194+30.8+139.0	8.75 ± 0.09	-0.66 ± 0.10	-1.57 ± 0.15	-2.37 ± 0.11	-0.69 ± 0.10
NGC 5194+104.1-105.5	8.56 ± 0.04	-0.60 ± 0.06	-1.24 ± 0.08	-2.04 ± 0.07	
NGC 5194+98.1-113.8	8.54 ± 0.03	-0.51 ± 0.04	-1.19 ± 0.05	-2.10 ± 0.05	-0.86 ± 0.04
NGC 5194+71.2+135.9	8.56 ± 0.05	-0.59 ± 0.06	-1.41 ± 0.09	-2.24 ± 0.08	-0.78 ± 0.08
NGC 5194+83.4-133.1	8.57 ± 0.06	-0.55 ± 0.07	-1.26 ± 0.10	-1.95 ± 0.08	
NGC 5194+109.9-121.4	8.51 ± 0.07	-0.57 ± 0.09	-1.16 ± 0.12	-2.08 ± 0.10	-0.70 ± 0.10
NGC 5194+112.2-126.6	8.75 ± 0.12	-0.72 ± 0.16	-1.40 ± 0.22	-2.17 ± 0.18	
NGC 5194+150.6+99.0	8.67 ± 0.11	-0.70 ± 0.15	-1.31 ± 0.19	-2.11 ± 0.14	
NGC 5194-159.5-116.4	8.73 ± 0.09	-0.72 ± 0.11	-1.47 ± 0.16	-2.14 ± 0.12	
NGC 5194-135.4-181.4	8.61 ± 0.07	-0.77 ± 0.10	-1.30 ± 0.13	-2.18 ± 0.10	-0.65 ± 0.08
NGC 5194+114.5+230.8	8.46 ± 0.06	-0.69 ± 0.08	-1.25 ± 0.11	-2.08 ± 0.08	-0.83 ± 0.06

(This table is available in machine-readable form.)

$ \begin{array}{c} \mathrm{NGC} 5457 + 47.9 + 103.2 \\ \mathrm{NGC} 5457 + 12.0 + 139.0 \\ \mathrm{NGS} 5457 + 12.0 + 139.0 \\ \mathrm{NGS} 5457 + 13.9 + 30.6 \\ \mathrm{NGS} 5457 + 13.9 + 30.6 \\ \mathrm{NGC} 5457 + 13.9 + 30.6 \\ \mathrm{NGC} 5457 + 13.9 + 30.6 \\ \mathrm{NGC} 5457 + 13.4 + 58.8 \\ \mathrm{NGC} 5457 + 134.4 + 19.7 \\ \mathrm{NGC} 5457 + 134.4 + 19.7 \\ \mathrm{NGC} 5457 + 149.7 \\ \mathrm{NGC} 5457 + 1$	$H\alpha$ Region	$12 + \log(O/H)$	log(N/O)	log(S/O)	log(Ar/O)	log(Ne/O)
$ \begin{array}{c} \mathrm{NGC} 5457 + 479 - 103.2 \\ \mathrm{NGC} 5457 + 12.0 + 139.0 \\ \mathrm{NGC} 5457 + 12.0 + 139.0 \\ \mathrm{NGC} 5457 + 13.9 + 30.6 \\ \mathrm{NGC} 5457 + 13.4 + 58.8 \\ \mathrm{NGC} 5457 + 13.4 + 50.8 \\ \mathrm{NGC} 5457 + 14.4 + 0.7 \\ \mathrm{NGC} 5457 + 14$	NGC 5457-75.0+29.3	8.65 ± 0.14	-0.62 ± 0.16	-1.34 ± 0.22	-2.21 ± 0.16	
$ \begin{array}{c} \mathrm{NGC} \ 5457 + 12.0 + 139.0 \\ \mathrm{NGC} \ 5457 + 138.9 + 30.6 \\ \mathrm{NGC} \ 5457 + 134.4 + 58.8 \\ \mathrm{8.62} \pm 0.10 \\ \mathrm{O-91} \pm 0.13 \\ \mathrm{O-92} \pm 0.05 \\ \mathrm{O-191} \pm 0.13 \\ \mathrm{O-92} \pm 0.05 \\ \mathrm{O-122} \pm 0.05 \\ \mathrm{O-2.12} \pm 0.05 \\ \mathrm{O-2.25} \pm 0.05 \\ $	NGC 5457+22.1-102.1	8.73 ± 0.11	-0.80 ± 0.15	-1.49 ± 0.20	-2.28 ± 0.16	-0.49 ± 0.20
$ \begin{array}{c} \mathrm{NGC} \ 5457 + 138.9 + 30.6 \\ \mathrm{NGC} \ 5457 + 138.4 + 58.8 \\ \mathrm{NGC} \ 5457 + 134.4 + 58.8 \\ \mathrm{NGC} \ 5457 + 104.4 + 64.9 \\ \mathrm{NGC} \ 5457 + 104.4 + 9.9 \\ \mathrm{NGC} \ 5457 + 104.4 + 9.9 \\ \mathrm{NGC} \ 5457 + 104.4 + 9.9 \\ \mathrm{NGC} \ 5457 + 104.4 + 9.7 \\ \mathrm{NGC} \ 5457 + 104.4 + 9.0 \\ \mathrm{NGC} \ 5457 + 104.4 + 104.4 \\ \mathrm{NGC} \ 5457 + 1$	NGC 5457+47.9-103.2	8.79 ± 0.09	-0.82 ± 0.11	-1.32 ± 0.15	-2.07 ± 0.13	
$ \begin{array}{c} \mathrm{NGC} \; 5457 + 134.4 + 58.8 \\ \mathrm{NGC} \; 5457 + 164.6 + 9.9 \\ \mathrm{NGO} \; 50.03 \\ \mathrm{NGC} \; 5457 + 164.6 + 9.9 \\ \mathrm{NGC} \; 5457 + 80.3 + 149.7 \\ \mathrm{NGC} \; 5457 + 80.3 + 149.7 \\ \mathrm{NGC} \; 5457 + 80.3 + 149.7 \\ \mathrm{NGC} \; 5457 + 162.2 \\ \mathrm{NGC} \; 5457 + 162.2 \\ \mathrm{NGC} \; 5457 + 162.2 \\ \mathrm{NGC} \; 5457 + 166.4 + 86.3 \\ \mathrm{NGE} \; 5457 + 102.2 \\ \mathrm{NGC} \; 5457 + 166.4 + 86.3 \\ \mathrm{NGE} \; 5457 + 102.2 \\ \mathrm{NGC} \; 5457 + 102.2 \\ NGC$	NGC 5457-12.0+139.0	8.53 ± 0.13	-0.71 ± 0.17	-1.28 ± 0.22	-2.21 ± 0.18	-0.58 ± 0.21
$ \begin{array}{c} \mathrm{NGC} \ 5457 + 164.6 + 9.9 \\ \mathrm{NGC} \ 5457 + 80.140.7 \\ \mathrm{NGC} \ 5457 + 80.3 + 149.7 \\ \mathrm{NGC} \ 5457 + 166.4 + 86.3 \\ \mathrm{NGC} \ 5457 + 177.2 + 24.2 \\ \mathrm{NGC} \ 5457 + 179.9 + 89.6 \\ \mathrm{NS} \ 85.8 \pm 0.08 \\ \mathrm{NGC} \ 5457 + 10.11 \\ \mathrm{NGC} \ 5457 + 133.1 + 126.8 \\ \mathrm{NS} \ 85.8 \pm 0.08 \\ \mathrm{NGC} \ 5457 + 133.1 + 126.8 \\ \mathrm{NS} \ 85.8 \pm 0.08 \\ \mathrm{NGC} \ 5457 + 133.1 + 126.8 \\ \mathrm{NGC} \ 5457 + 120.2 + 146.9 \\ \mathrm{NGC} \ 5457 + 130.2 + 157.4 \\ \mathrm{NGC} \ 5457 + 120.2 + 146.8 \\ \mathrm{NS} \ 70.00 \\ \mathrm{NGC} \ 5457 + 120.2 + 146.8 \\ \mathrm{NS} \ 70.00 \\ \mathrm{NGC} \ 5457 + 120.2 + 146.8 \\ \mathrm{NS} \ 70.00 \\ \mathrm{NGC} \ 5457 + 120.2 + 161.7 \\ \mathrm{NGC} \ 5457 + 120.2 + 120.11 \\ \mathrm{NGC} \ 5457 + 120.2 + 1$	NGC 5457+138.9+30.6	8.50 ± 0.07	-0.77 ± 0.09	-1.24 ± 0.11	-2.05 ± 0.08	-0.61 ± 0.06
$\begin{array}{c} \text{NGC } 5457 + 89.3 + 149.7 \\ \text{NGC } 5457 - 70.2 + 162.2 \\ \text{NGC } 5457 - 70.2 + 162.2 \\ \text{NGC } 5457 - 70.2 + 162.2 \\ \text{NGC } 5457 - 166.4 + 86.3 \\ \text{NGC } 5457 - 170.2 + 120.10 \\ \text{NGC } 5457 - 120.2 + 146.9 \\ \text{NGC } 5457 - 120.2 + 146.9 \\ \text{NGC } 5457 - 120.2 + 146.9 \\ \text{NGC } 5457 - 120.2 + 161.7 \\ \text{NGC } 5457 - 120.2 + 120.10 \\ \text{NGC } 5457 - 120.2 + 1$	NGC 5457+134.4-58.8	8.62 ± 0.10	-0.91 ± 0.13	-1.66 ± 0.17	-2.36 ± 0.13	-0.66 ± 0.10
$\begin{array}{c} \mathrm{NGC} \ 5457-70.2+162.2 \\ \mathrm{NGC} \ 5457+166.4+86.3 \\ \mathrm{NGC} \ 5457+166.4+86.3 \\ \mathrm{NGC} \ 5457+166.4+86.3 \\ \mathrm{NGC} \ 5457+177.2+2.8 \\ \mathrm{NGC} \ 5457+177.2+2.8 \\ \mathrm{NGC} \ 5457+177.2+2.8 \\ \mathrm{NGC} \ 5457+177.2+2.8 \\ \mathrm{NGC} \ 5457+159.9+89.6 \\ \mathrm{NGS} \ 5457+25.2+10.0 \\ \mathrm{NGC} \ 5457+159.9+89.6 \\ \mathrm{NGC} \ 5457+133.1+126.8 \\ \mathrm{NGC} \ 5457+133.1+126.8 \\ \mathrm{NGC} \ 5457+133.1+126.8 \\ \mathrm{NGC} \ 5457+177.2+76.1 \\ \mathrm{NGC} \ 5457+177.2+76.1 \\ \mathrm{NGC} \ 5457+120.2+146.9 \\ \mathrm{NSC} \ 5457+120.2+161.7 \\ \mathrm{NGC} \ 5457+130.2+157.4 \\ \mathrm{NSC} \ 5457+120.2+161.7 \\ \mathrm{NGC} \ 5457+145.1+146.8 \\ \mathrm{NS} \ 8.87 \pm 0.08 \\ \mathrm{NS} \ 1-0.00 \pm 0.12 \\ \mathrm{NSC} \ 5457+145.1+146.8 \\ \mathrm{NS} \ 8.7 \pm 0.08 \\ \mathrm{NS} \ 1-0.00 \pm 0.12 \\ \mathrm{NSC} \ 5457+145.1+146.8 \\ \mathrm{NS} \ 1-0.00 \pm 0.12 \\ \mathrm{NSC} \ 5457+120.2+16.1 \\ \mathrm{NSC} \ 5457+20.2+16.1 \\ \mathrm{NSC} \ 5457+20.1 \\ \mathrm{NSC} \ 5457+20.0 \\$	NGC 5457+164.6+9.9	8.60 ± 0.03	-0.95 ± 0.05	-1.22 ± 0.05	-2.12 ± 0.05	-0.88 ± 0.01
$\begin{array}{c ccccccccccccccccccccccccccccccccccc$	NGC 5457+89.3+149.7	8.83 ± 0.16	-0.92 ± 0.22	-1.64 ± 0.26	-2.35 ± 0.19	-0.74 ± 0.16
$\begin{array}{c ccccccccccccccccccccccccccccccccccc$	NGC 5457-70.2+162.2	8.62 ± 0.13	-0.90 ± 0.18	-1.24 ± 0.22	-2.13 ± 0.14	-1.06 ± 0.07
$\begin{array}{c ccccccccccccccccccccccccccccccccccc$	NGC 5457+166.4+86.3	8.42 ± 0.08	-0.78 ± 0.11	-1.35 ± 0.14	-2.21 ± 0.10	
$\begin{array}{cccccccccccccccccccccccccccccccccccc$	NGC 5457+177.2-42.8	8.45 ± 0.06	-0.91 ± 0.09	-1.46 ± 0.11	-2.22 ± 0.08	-0.95 ± 0.05
$\begin{array}{c ccccccccccccccccccccccccccccccccccc$	NGC 5457-159.9+89.6	8.58 ± 0.08	-0.77 ± 0.11	-1.19 ± 0.15	-2.03 ± 0.11	-0.61 ± 0.09
$\begin{array}{c ccccccccccccccccccccccccccccccccccc$	NGC 5457+133.1-126.8	8.58 ± 0.14	-0.91 ± 0.17	-1.70 ± 0.22	-2.42 ± 0.16	-0.72 ± 0.12
$\begin{array}{c ccccccccccccccccccccccccccccccccccc$	NGC 5457+177.2+76.1	8.61 ± 0.09	-0.89 ± 0.12	-1.44 ± 0.16	-2.18 ± 0.11	-0.97 ± 0.07
$\begin{array}{c ccccccccccccccccccccccccccccccccccc$	NGC 5457-120.2+146.9	8.57 ± 0.06	-0.80 ± 0.10	-1.02 ± 0.12	-2.04 ± 0.08	-0.97 ± 0.05
$\begin{array}{c ccccccccccccccccccccccccccccccccccc$	NGC 5457+130.2+157.4	8.55 ± 0.10	-0.82 ± 0.13	-1.42 ± 0.17	-2.20 ± 0.12	-0.75 ± 0.08
$\begin{array}{c ccccccccccccccccccccccccccccccccccc$	NGC 5457+129.2+161.7	8.30 ± 0.04		-1.31 ± 0.07	-2.17 ± 0.07	-1.05 ± 0.06
$\begin{array}{c ccccccccccccccccccccccccccccccccccc$	NGC 5457-145.1+146.8	8.87 ± 0.08	-1.00 ± 0.12	-1.25 ± 0.16	-2.17 ± 0.13	-0.77 ± 0.13
$\begin{array}{c ccccccccccccccccccccccccccccccccccc$	NGC 5457+103.5+192.6	8.46 ± 0.08	-0.85 ± 0.11	-1.35 ± 0.16	-2.11 ± 0.13	-0.98 ± 0.14
$\begin{array}{cccccccccccccccccccccccccccccccccccc$	NGC 5457-205.4-98.2	8.57 ± 0.09	-0.90 ± 0.13	-1.17 ± 0.17	-2.28 ± 0.11	-1.05 ± 0.08
$\begin{array}{cccccccccccccccccccccccccccccccccccc$	NGC 5457+17.3-235.4	8.62 ± 0.07	-1.02 ± 0.12	-1.32 ± 0.14	-2.26 ± 0.09	-0.97 ± 0.04
$\begin{array}{cccccccccccccccccccccccccccccccccccc$	NGC 5457+36.8-233.4	8.45 ± 0.03	-0.99 ± 0.06	-1.50 ± 0.06	-2.27 ± 0.06	-0.86 ± 0.06
$\begin{array}{cccccccccccccccccccccccccccccccccccc$	NGC 5457+139.0+200.7		-0.96 ± 0.10	-1.48 ± 0.14		-0.75 ± 0.13
$\begin{array}{cccccccccccccccccccccccccccccccccccc$	NGC 5457+189.2-136.3	8.58 ± 0.02	-0.99 ± 0.05	-1.59 ± 0.05	-2.27 ± 0.05	-0.81 ± 0.01
$\begin{array}{cccccccccccccccccccccccccccccccccccc$	NGC 5457-183.9-179.0		-1.08 ± 0.23	-1.36 ± 0.25	-2.25 ± 0.15	-0.67 ± 0.07
$\begin{array}{cccccccccccccccccccccccccccccccccccc$	NGC 5457-249.4-51.3	8.51 ± 0.06	-0.90 ± 0.08	-1.38 ± 0.11	-2.28 ± 0.09	-0.54 ± 0.08
$\begin{array}{cccccccccccccccccccccccccccccccccccc$	NGC 5457-250.8-52.0	8.59 ± 0.11	-0.94 ± 0.15	-1.45 ± 0.20	-2.46 ± 0.16	-0.28 ± 0.16
$\begin{array}{cccccccccccccccccccccccccccccccccccc$	NGC 5457+225.6-124.1	8.49 ± 0.05	-1.05 ± 0.08	-1.53 ± 0.10	-2.35 ± 0.07	-0.81 ± 0.03
$\begin{array}{cccccccccccccccccccccccccccccccccccc$	NGC 5457+117.9-235.0	8.30 ± 0.07	-1.10 ± 0.11	-1.45 ± 0.14	-2.24 ± 0.11	-0.95 ± 0.11
$\begin{array}{cccccccccccccccccccccccccccccccccccc$	NGC 5457-208.0-180.7	8.45 ± 0.10	-0.92 ± 0.17	-1.34 ± 0.19	-2.29 ± 0.11	-0.65 ± 0.05
$\begin{array}{llllllllllllllllllllllllllllllllllll$	NGC 5457-12.3-271.1	8.49 ± 0.08	-0.99 ± 0.10	-1.49 ± 0.14	-2.06 ± 0.12	-0.99 ± 0.12
$\begin{array}{llllllllllllllllllllllllllllllllllll$	NGC 5457-200.3-193.6	8.60 ± 0.06	-1.13 ± 0.11	-1.33 ± 0.12	-2.32 ± 0.10	-0.72 ± 0.10
$\begin{array}{cccccccccccccccccccccccccccccccccccc$	NGC 5457+96.7+266.9	8.49 ± 0.08	-0.96 ± 0.11		-2.32 ± 0.09	-0.70 ± 0.06
NGC 5457+254.6-107.2 8.50 ± 0.01 -0.98 ± 0.02 -1.46 ± 0.04 -2.18 ± 0.04 -0.77 ± 0.08 NGC 5457+281.4-71.8 8.42 ± 0.05 -1.15 ± 0.08 -1.48 ± 0.09 -2.28 ± 0.08 -0.89 ± 0.08	NGC 5457+67.5+277.0	8.52 ± 0.05	-1.04 ± 0.10	-1.37 ± 0.11	-2.27 ± 0.07	-0.73 ± 0.05
NGC 5457+254.6-107.2 8.50 ± 0.01 -0.98 ± 0.02 -1.46 ± 0.04 -2.18 ± 0.04 -0.77 ± 0.08 NGC 5457+281.4-71.8 8.42 ± 0.05 -1.15 ± 0.08 -1.48 ± 0.09 -2.28 ± 0.08 -0.89 ± 0.08	NGC 5457+252.2-109.8	8.53 ± 0.08	-1.01 ± 0.13	-1.52 ± 0.15	-2.48 ± 0.10	-0.77 ± 0.06
NGC 5457+281.4-71.8 8.42 \pm 0.05 -1.15 ± 0.08 -1.48 ± 0.09 -2.28 ± 0.08 $-0.89 \pm$				-1.46 ± 0.04		-0.77 ± 0.01
100 000 100 000 100 000 100 000 100 100 100 100 100 100 100 100 100 100 100 100 100 100 100 100 100 100 100 100 100 100 100 100 100 100 100 100 100 100 100 100 100 100 100 100 100 100 100 100 100 100 100 100 100 100 100 100 100 100 100 100 100 100 100 100 100 100 100 100 100 100 100 100 100 100 100 100 100 100 100 100 100 100 100 100 100 100 100 100 100 100 100 100 100 100 100 100 100 100 100 100 100 100 100 100 100 100 100 100 100 100 100 100 100 100 100 100 100 100 100 100 100 100 100 100 100 100 100 100 100 100 100 100 100 100 100 100 100 100 100 100 100 100 100 100 100 100 100 100 100 100 100 100 100 100 100 100 100 100 100 100 100 100 100 100 100 100 100 100 100 100 100 100 100 100 100 100 100 100 100 100 100 100 100 100 100 100 100 100 100 100 100 100 100 100 100 100 100 100 100 100 100 100 100 100 100 100 100 100 100 100 100 100 100 100 100 100 100 100 100 100 100 100 100 100 100 100 100 100 100 100 100 100 100 100 100 100 100 100 100 100 100 100 100 100 100 100 100 100 100 100 100 100 100 100 100 100 100 100 100 100 100 100 100 100 100 100 100 100 100 100 100 100 100 100 100 100 100 100 100 100 100 100 100 100 100 100 100 100 100 100 100 100 100 100 100 100 100 100 100 100 100 100 100 100 100 100 100 100 100 100 100 100 100 100 100 100 100 100 100 100 100 100 100 100 100 100 100 100 100 100 100 100 100 100 100 100 100 100 100 100 100 1		8.42 ± 0.05	-1.15 ± 0.08	-1.48 ± 0.09	-2.28 ± 0.08	-0.89 ± 0.07
NGC 545/-243.0+159.6 8.49 \pm 0.06 -1.00 ± 0.09 -1.23 ± 0.12 -2.20 ± 0.11 $-0.92 \pm$	NGC 5457-243.0+159.6	8.49 ± 0.06	-1.00 ± 0.09	-1.23 ± 0.12	-2.20 ± 0.11	-0.92 ± 0.12

Table B3 (Continued)

		(Continued)			
$H\alpha$ Region	$12 + \log(O/H)$	log(N/O)	log(S/O)	log(Ar/O)	log(Ne/O)
NGC 5457+249.3+201.9	8.42 ± 0.09	-1.06 ± 0.16	-1.34 ± 0.18	-2.31 ± 0.10	-0.71 ± 0.05
NGC 5457-297.7+87.1	8.45 ± 0.10	-1.04 ± 0.15	-1.38 ± 0.19	-2.25 ± 0.13	-0.93 ± 0.11
NGC 5457-309.4+56.9	8.35 ± 0.03	-0.92 ± 0.05	-1.31 ± 0.06	-2.41 ± 0.07	-0.78 ± 0.06
NGC 5457+354.1+71.2	8.51 ± 0.10	-1.23 ± 0.19	-1.17 ± 0.20	-2.18 ± 0.11	-0.70 ± 0.03
NGC 5457-164.9-333.9	8.53 ± 0.03	-1.23 ± 0.08	-1.33 ± 0.07	-2.27 ± 0.06	-0.89 ± 0.05
NGC 5457+360.9+75.3	8.51 ± 0.02	-1.22 ± 0.05	-1.11 ± 0.05	-2.16 ± 0.05	-0.69 ± 0.03
NGC 5457-377.9-64.9	8.52 ± 0.06	-1.08 ± 0.10	-1.33 ± 0.11	-2.33 ± 0.08	-0.62 ± 0.07
NGC 5457-99.6-388.0	8.39 ± 0.01	-1.12 ± 0.03	-1.29 ± 0.04	-2.08 ± 0.04	-0.71 ± 0.01
NGC 5457-397.4-71.7	8.33 ± 0.04	-1.06 ± 0.07	-1.46 ± 0.08	-2.64 ± 0.07	-0.60 ± 0.07
NGC 5457-226.9-366.4	8.28 ± 0.06	-1.20 ± 0.12	-1.28 ± 0.13	-2.22 ± 0.08	-0.93 ± 0.05
NGC 5457-405.5-157.7	8.14 ± 0.02	-1.02 ± 0.04	-1.49 ± 0.04	-2.26 ± 0.05	-0.84 ± 0.04
NGC 5457-345.5+273.8	8.35 ± 0.04	-1.17 ± 0.09	-1.33 ± 0.09	-2.44 ± 0.09	-0.53 ± 0.07
NGC 5457-410.3-206.3	8.32 ± 0.09	-1.14 ± 0.14	-1.62 ± 0.16	-2.31 ± 0.11	-0.94 ± 0.08
NGC 5457-371.1-280.0	8.33 ± 0.03	-1.11 ± 0.07	-1.48 ± 0.06	-2.36 ± 0.05	-0.67 ± 0.01
NGC 5457-368.3-285.6	8.45 ± 0.02	-1.12 ± 0.05	-1.51 ± 0.05	-2.41 ± 0.05	-0.70 ± 0.01
NGC 5457-455.7-55.8	8.18 ± 0.03	-1.37 ± 0.05	-1.47 ± 0.06	-2.43 ± 0.06	-0.61 ± 0.05
NGC 5457-392.0-270.1	8.36 ± 0.02	-1.09 ± 0.06	-1.63 ± 0.04	-2.27 ± 0.04	-0.70 ± 0.01
NGC 5457-414.1-253.6	8.28 ± 0.03	-1.15 ± 0.10	-1.60 ± 0.06	-2.15 ± 0.07	-0.67 ± 0.06
NGC 5457-464.7-131.0	8.16 ± 0.01	-1.34 ± 0.05	-1.53 ± 0.02	-2.46 ± 0.05	-0.63 ± 0.02
NGC 5457-466.1-128.2	8.01 ± 0.04	-1.34 ± 0.08	-1.50 ± 0.08	-2.39 ± 0.07	-0.69 ± 0.06
NGC 5457-479.7-3.9	8.15 ± 0.01	-0.90 ± 0.07	-1.61 ± 0.02	-2.53 ± 0.05	-0.70 ± 0.02
NGC 5457-481.4-0.5	7.95 ± 0.03	-1.30 ± 0.05	-1.46 ± 0.06	-2.47 ± 0.06	-0.57 ± 0.05
NGC 5457-453.8-191.8	8.24 ± 0.06	-1.38 ± 0.13	-1.68 ± 0.14	-2.60 ± 0.07	-0.64 ± 0.02
NGC 5457+331.9+401.0	8.23 ± 0.01	-1.33 ± 0.05	-1.56 ± 0.04	-2.38 ± 0.05	-0.69 ± 0.03
NGC 5457+324.5+415.8	8.23 ± 0.02	-1.31 ± 0.05	-1.48 ± 0.03	-2.49 ± 0.06	-0.70 ± 0.04
NGC 5457+315.3+434.4	8.33 ± 0.01	-1.29 ± 0.04	-1.37 ± 0.02	-2.42 ± 0.05	-0.62 ± 0.04
NGC 5457-540.5-149.9	7.89 ± 0.01	-1.33 ± 0.07	-1.66 ± 0.05	-2.26 ± 0.05	-0.63 ± 0.03
NGC 5457+509.5+264.1	8.29 ± 0.06	-1.34 ± 0.17	-1.43 ± 0.08	-2.27 ± 0.08	-0.64 ± 0.02
NGC 5457+266.0+534.1	8.18 ± 0.03	-1.37 ± 0.05	-1.47 ± 0.06	-2.43 ± 0.06	-0.61 ± 0.05
NGC 5457+667.9+174.1	8.16 ± 0.02	-1.34 ± 0.11	-1.43 ± 0.05	-2.17 ± 0.05	-0.72 ± 0.02
NGC 5457+650.1+270.7	8.09 ± 0.04	-1.35 ± 0.08	-1.47 ± 0.06		-0.58 ± 0.10
NGC 5457+692.1+272.9	8.10 ± 0.04	-1.45 ± 0.12	-1.35 ± 0.12	-2.33 ± 0.09	-0.67 ± 0.07
NGC 5457+1.0+885.8	7.86 ± 0.01	-1.46 ± 0.02	-1.45 ± 0.02	-2.69 ± 0.06	-0.68 ± 0.05
NGC 5457+6.6+886.3	7.92 ± 0.01	-1.40 ± 0.05	-1.40 ± 0.02	-2.65 ± 0.05	-0.67 ± 0.03
NGC 5457-8.5+886.7	7.81 ± 0.02	-1.42 ± 0.06	-1.32 ± 0.04	-2.79 ± 0.10	-0.68 ± 0.10

(This table is available in machine-readable form.)

Appendix C CHAOS Surface-density Profiles

In order to test whether the abundance gradients in CHAOS galaxies correlate with their individual disk properties, we need to determine surface-density properties that correspond to our observed H II regions. We therefore examine the surface-density profiles of the stellar mass, the gas mass, and the SFR of our CHAOS sample.

C.1. Data and Profile Determinations

Owing to the well-studied nature of the galaxies in our sample, there exists a plethora of ancillary data to aid in this task. Specifically, we use HERACLES CO(2–1) line-integrated intensity (moment–0) maps (Leroy et al. 2009) to trace the molecular gas, THINGS H I 21 cm line-integrated intensity maps (Walter et al. 2008) to trace the atomic gas, Spitzer IRAC 3.6 μ m images to trace stellar mass, and SFR surface-density maps created in the z=0 Multiwavelength Galaxy Synthesis project (Z0MGS; Leroy et al. 2019).

The CO maps were converted into molecular gas surface-density maps by assuming a standard Galactic CO-to- H_2 conversion factor of $\alpha_{\rm CO} = 4.35~M_\odot~{\rm pc}^{-2}({\rm K~km~s}^{-1})^{-1}$ (including heavy element

contribution; Bolatto et al. 2013) and a CO(2-1)/(1-0) line ratio of $R_{21} = 0.7$ (Leroy et al. 2013; Saintonge et al. 2017). For the atomic gas surface-density maps, HI intensities were converted using a standard conversion factor of 1.97 \times 10⁻² M_{\odot} pc⁻²(K km s⁻¹)⁻¹, which includes heavy element contribution. The stellar-mass surface-density distributions adopted a conversion factor of $420 M_{\odot} \text{ pc}^{-2}(\text{M Jy sr}^{-1})$, assuming a fixed mass-to-light ratio of $Y_{3.6} = 0.6 M_{\odot}/L_{\odot,3.6}$ (Querejeta et al. 2015). For all galaxies except NGC 5457, we also have dust-corrected IRAC 3.6 μm images from S⁴G (Sheth et al. 2010; Querejeta et al. 2015). The same conversion factors were used for these maps. Finally, the SFR surface-density maps were derived by combining backgroundsubtracted, astrometry-matched, and resolution-matched Galaxy Evolution Explorer FUV and Wide-field Infrared Survey Explorer (WISE) 24 µm images, and converting the measured broadband intensities to SFR surface density (Jarrett et al. 2013; Cluver et al.

Next, we built radial profiles from the mass and SFR surface-density maps. Using the galaxy parameters listed in Table 1, we determined the de-projected galactocentric radius for each pixel in each map. Pixels were then assigned to a series of radial bins each having a width of 15", where the bin size was limited by the beam size of the Z0MGS SFR maps

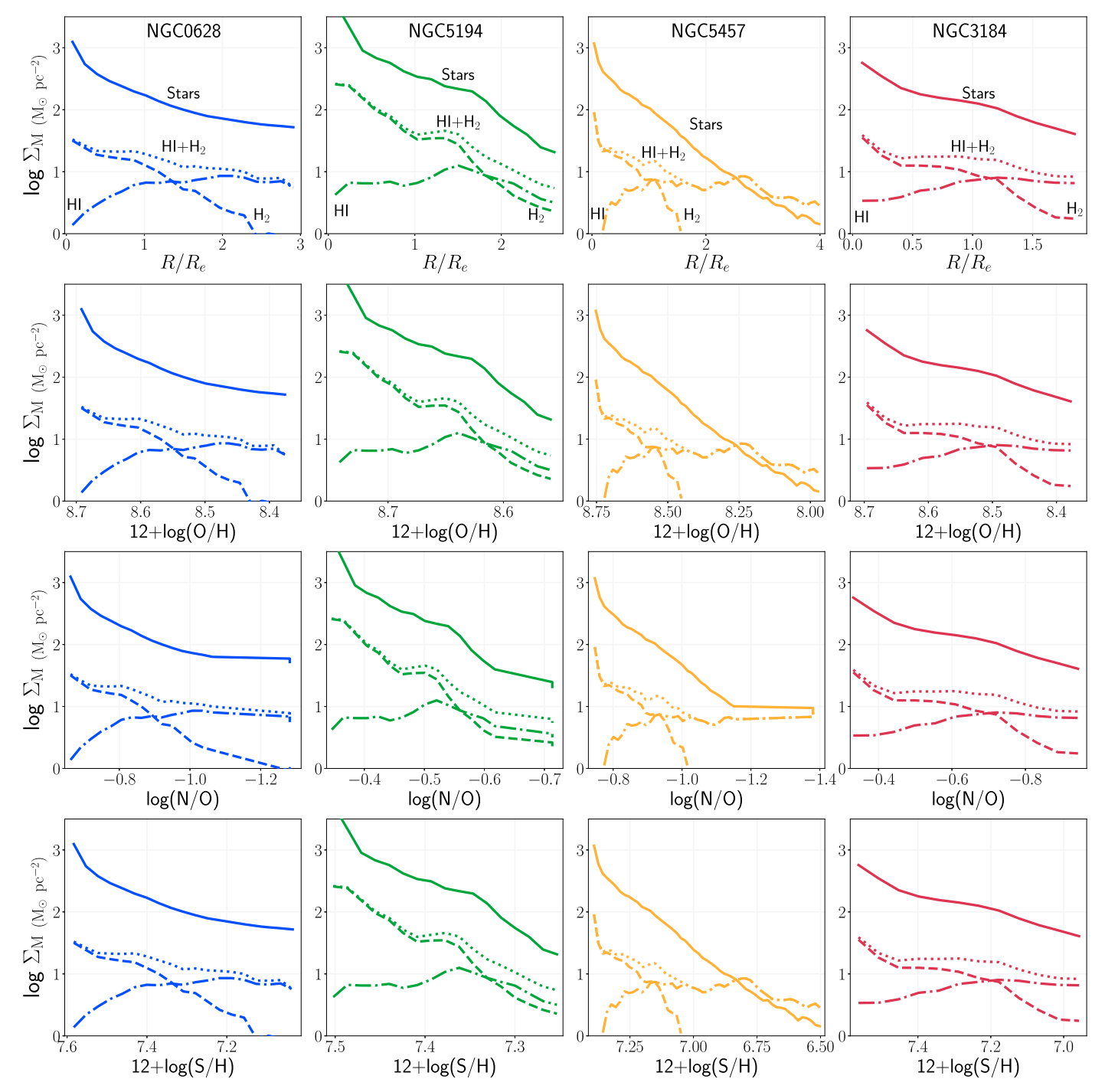


Figure C1. Mass surface-density profiles for different components of the first four CHAOS galaxies vs. galactocentric radius (top row), oxygen abundance (middle row), and N/O abundance (bottom row). Values for $12 + \log(O/H)$ and $\log(N/O)$ are from the linear fits plotted in Figures 6 and 9. Stellar-mass profiles are plotted as solid lines and decrease with increasing radius. Molecular H_2 gas profiles are plotted as dashed lines and also generally decrease outward. Atomic H I gas profiles are plotted as dotted-dashed lines, intersecting the H_2 trends at unique points in each galaxy. Total H I+H2 gas is shown by the dotted line.

(all other maps have smaller beam sizes). Within each radial bin, we derived mean, median, and 16%–84% percentiles for each surface-density tracer. For molecular gas surface density in particular, we also estimated the error of the mean value based on the published moment–zero uncertainty maps (Leroy et al. 2009). The resulting derived molecular gas surface-density profiles have a signal-to-noise ratio (S/N) \geqslant 3 in most of the bins; however, in cases with lower S/Ns, the 3σ upper limit was provided.

The Z0MGS WISE 1 maps (which trace stellar-mass distribution) were also used to derive the effective radii, R_e , used throughout this work. For this calculation, all foreground stars in the field of view were masked. All pixels were put into a series of radial bins, where masked pixels with $R_g < 0.4 \times R_{25}$ and all pixels with $R_g > 0.4 \times R_{25}$ were substituted for the median unmasked pixel value within the same radial bin. The resulting maps were then integrated out to $1.5 \times R_{25}$ to determine each galaxy's integrated flux, and the

equi-radius contour encompassing half of this integrated flux is the effective radius (see Table 1).

C.2. Profile Comparisons for CHAOS Galaxies

The derived mass surface densities for various galaxy components (i.e., stars, H I, H₂) are plotted in Figure C1 for the CHAOS sample. As expected for an interacting galaxy, the H₂ profile of NGC 5194 is different from the other three galaxies, as it both dominates the gas profile and makes up a larger fraction of the total galaxy mass. We find that the stellar-and gas-mass surface-density profiles of the other three noninteracting galaxies look similar, with H₂ more prominent in the inner $\sim 1R_e$ of the disk, H I dominating the outer disk, and the stellar mass roughly following the total gas mass $(M_{\rm gas} = M_{\rm H~I} + M_{\rm H_2})$ for $R_g/R_e < 2$.

We show the total gas-mass surface-density profiles, which are dominated by the H₂ gas for most of the disk, versus both radius and elemental abundances (O, N, and S) in the left column of Figure C2. Interestingly, while we find the stellarmass and gas-mass surface-density profiles of individual galaxies to be offset from one another when plotted versus their N/O profiles, the shift is minimal for the O/H and S/H trends. Since the decline of H₂ gas mass with radius corresponds to a decreasing SFR (as shown in the right column of Figure C2) and SFE, this could indicate that the H₂ mass surface density plays the leading role in the stellar and subsequent chemical evolution of these galaxies.

C.3. Local Scaling Relations

Rosales-Ortega et al. (2012), using IFU spectroscopy from the PINGS (Rosales-Ortega et al. 2010) and CALIFA surveys, reported the first *local* mass–metallicity (M–Z) scaling relationship of H II regions in spiral galaxies, with a secondary dependence on the equivalent width of H α (a proxy from SFR). This local M–Z–EW(H α) relationship is the logical product of inside-out disk growth and the dependence of SFR on mass. While the more widely known fundamental M–Z–SFR global relationship (Mannucci et al. 2010) has been explained by galaxy growth via the accretion of cold gas that is altered by feedback of gaseous inflows and outflows, the *local* M–Z–SFR relationship allows us to explore physical parameters that may be regulating the growth and chemical evolution *within* spiral disks.

The stellar-mass surface-density $(\Sigma_{M_{\odot}})$ radial profiles are reproduced for the four CHAOS galaxies in the first panel of Figure C3. We fit a polynomial to the $\Sigma_{M_{\odot}}$ - R_e (Figure C3) and $\Sigma_{\rm SFR}$ - R_e trend of each galaxy. These fits are then used to plot the stellar-mass surface densities corresponding to the *observed* O/H and N/O abundances of the CHAOS H II regions. The $\Sigma_{M_{\odot}}$ -O/H and $\Sigma_{M_{\odot}}$ -N/O trends are plotted in the middle and right panels of Figure C3, respectively, and color-coded by SFR surface density ($\Sigma_{\rm SFR}$). Since SFR is known to depend on stellar mass, the vertical color gradient seen for the SFR in the $\Sigma_{M_{\odot}}$ -O/H is expected. However, in the $\Sigma_{M_{\odot}}$ -N/O relationship, not only is the scatter significantly reduced relative to the O/H trend, but SFR also appears to increase *along* the N/O gradient.

The metallicity–surface-density relationship may reflect fundamental similarities in the evolution of non-barred, noninteracting spiral galaxies. For example, Ryder (1995) argues for a galaxy

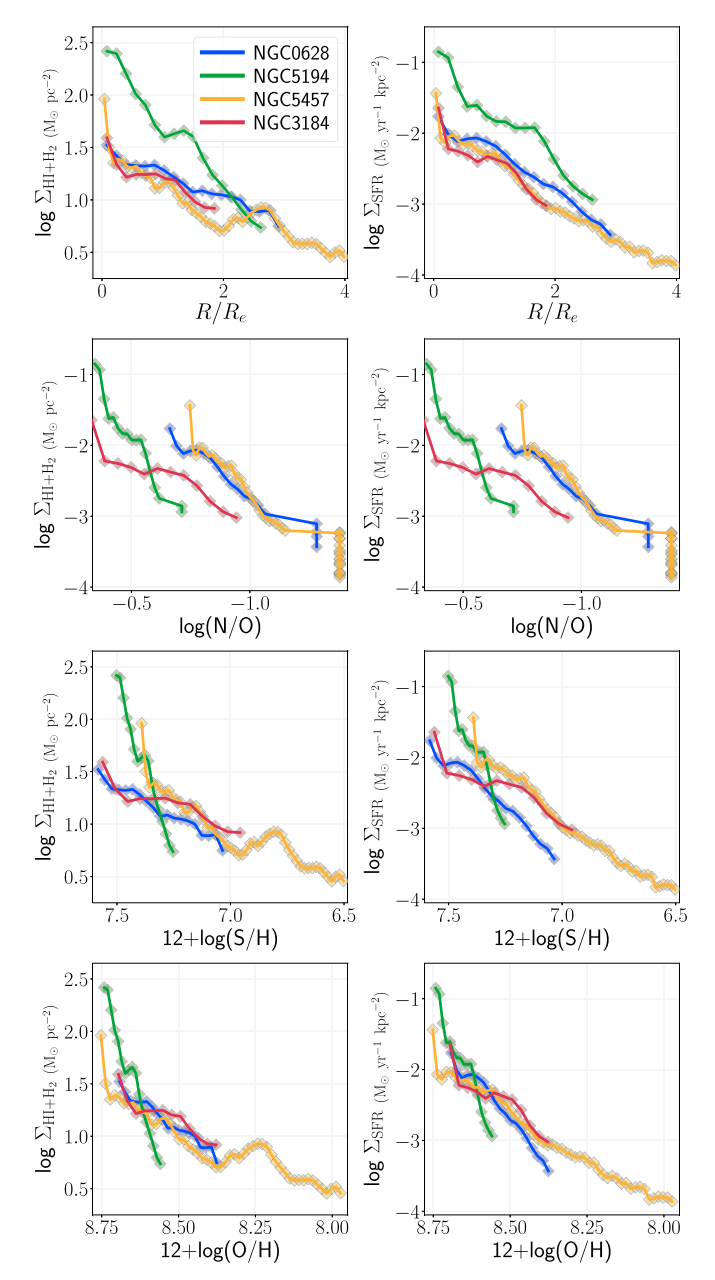


Figure C2. Left panels: total gas-mass surface-density profiles for the four CHAOS galaxies as scaled by disk effective radius (top panel), N/O abundance (second panel), sulfur abundance (third panel), and oxygen abundance (bottom panel). These profiles are dominated by H_2 gas for most of the disk. Right panels: total SFR surface-density profiles vs. radius and abundance trends. The right and left columns of panels show the observed increase in local SFR with increasing H_2 mass surface density, which drives the increasing abundance trends.

evolution model that includes self-regulating star formation, where energy injected into the ISM by newly formed stars inhibits further star formation. These models were able to successfully reproduce the observed correlations between surface brightness and SFR (Dopita & Ryder 1994) and surface mass density (e.g., Phillipps & Edmunds 1991; Ryder 1995; Garnett et al. 1997). The current work supports the idea that stellar-mass surface density is a fundamental parameter governing spiral-galaxy evolution and is particularly important for the relative timescales involved in N/O production.

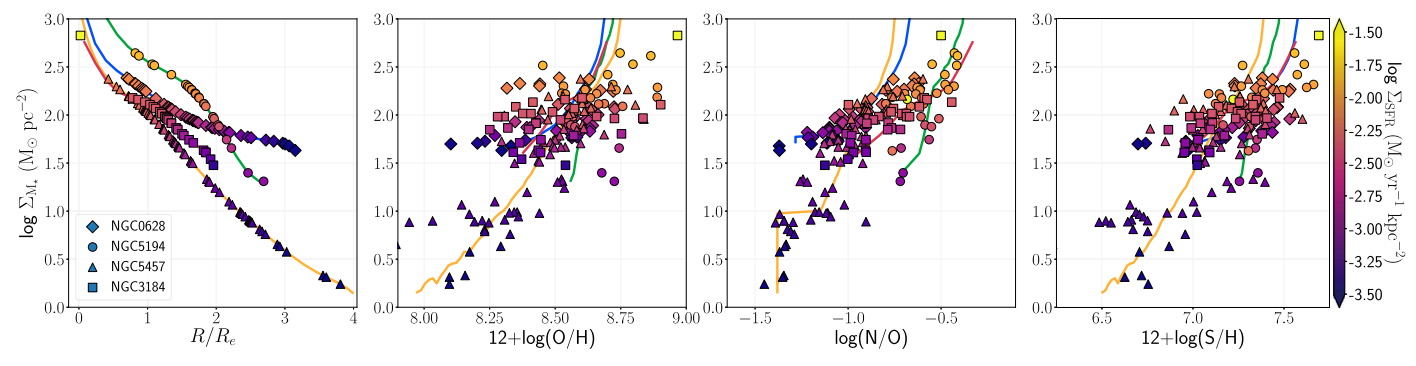


Figure C3. Left panel: stellar-mass surface densities for the CHAOS sample vs. galactocentric radius where the colored lines represent the average profile of each galaxy. Second panel: the local M–Z–SFR relationship. For each observed data point x, we plot the fit $\log \Sigma M_*(R_x)$ vs. the measured $12 + \log(O/H)_{xx}$ color-coded by the its log $\Sigma SFR(R_x)$ value. The large spread is due to the real scatter in observed O/H. Third panel: the local M-N/O-SFR relationship. This panel shows the stellarmass surface-density trend, similar to the second panel, but vs. measured N/O, forming a tight correlation. Right panel: the local M-S/H-SFR relationship.

Filippenko, A. V. 1982, PASP, 94, 715

Garnett, D. R., & Shields, G. A. 1987, ApJ, 317, 82

Garnett, D. R. 1990, ApJ, 363, 142

Garnett, D. R. 1992, AJ, 103, 1330 Garnett, D. R. 2002, ApJ, 581, 1019

García-Rojas, J., Peña, M., Morisset, C., et al. 2013, A&A, 558, A122

Garnett, D. R., Shields, G. A., Skillman, E. D., Sagan, S. P., & Dufour, R. J.

ORCID iDs

Danielle A. Berg https://orcid.org/0000-0002-4153-053X Richard W. Pogge https://orcid.org/0000-0003-1435-3053 Evan D. Skillman https://orcid.org/0000-0003-0605-8732 Kevin V. Croxall https://orcid.org/0000-0002-5258-7224 Jiayi Sun https://orcid.org/0000-0003-0378-4667

References

```
Asplund, M., Grevesse, N., Sauval, A. J., & Scott, P. 2009, ARA&A, 47, 481
Bacon, R., Accardo, M., Adjali, L., et al. 2010, Proc. SPIE, 7735, 773508
Baron, E., Branch, D., & Hauschildt, P. H. 2007, ApJ, 662, 1148
Belfiore, F., Maiolino, R., Tremonti, C., et al. 2017, MNRAS, 469, 151
Berg, D. A., Erb, D. K., Auger, M. W., Pettini, M., & Brammer, G. B. 2018,
    ApJ, 859, 164
Berg, D. A., Erb, D. K., Henry, R. B. C., Skillman, E. D., &
  McQuinn, K. B. W. 2019, ApJ, 874, 93
Berg, D. A., Skillman, E. D., Croxall, K. V., et al. 2015, ApJ, 806, 16
Berg, D. A., Skillman, E. D., Marble, A. R., et al. 2012, ApJ, 754, 98
Binette, L., Matadamas, R., Hägele, G. F., et al. 2012, A&A, 547, A29
Bohlin, R. C. 2014, AJ, 147, 127
Bolatto, A. D., Wolfire, M., & Leroy, A. K. 2013, ARA&A, 51, 207
Bose, S., & Kumar, B. 2014, ApJ, 782, 98
Bresolin, F., Kudritzki, R.-P., Urbaneja, M. A., et al. 2016, ApJ, 830, 64
Bruzual, G., & Charlot, S. 2003, MNRAS, 344, 1000
Bryant, J. J., Owers, M. S., Robotham, A. S. G., et al. 2015, MNRAS,
Bundy, K., Bershady, M. A., Law, D. R., et al. 2015, ApJ, 798, 7
Chisholm, J., Rigby, J. R., Bayliss, M., et al. 2019, ApJ, 882, 182
Cluver, M. E., Jarrett, T. H., Dale, D. A., et al. 2017, ApJ, 850, 68
Colombo, D., Meidt, S. E., Schinnerer, E., et al. 2014, ApJ, 784, 4
Coziol, R., Reyes, R. E. C., Considère, S., Davoust, E., & Contini, T. 1999,
   A&A, 345, 733
Crockett, N. R., Garnett, D. R., Massey, P., & Jacoby, G. 2006, ApJ, 637, 741
Croxall, K. V., Pogge, R. W., Berg, D. A., Skillman, E. D., & Moustakas, J.
  2015, ApJ, 808, 42
Croxall, K. V., Pogge, R. W., Berg, D. A., Skillman, E. D., & Moustakas, J.
   2016, ApJ, 830, 4
Curti, M., Cresci, G., Mannucci, F., et al. 2017, MNRAS, 465, 1384
```

Dale, D. A., Cohen, S. A., Johnson, L. C., et al. 2009, ApJ, 703, 517 De Robertis, M. M., Dufour, R. J., & Hunt, R. W. 1987, JRASC, 81, 195

Dopita, M. A., & Ryder, S. D. 1994, ApJ, 430, 163

Edmunds, M. G., & Pagel, B. E. J. 1984, MNRAS, 211, 507

Erb, D. K., Pettini, M., Shapley, A. E., et al. 2010, ApJ, 719, 1168

Esteban, C., Bresolin, F., Peimbert, M., et al. 2009, ApJ, 700, 654

Ferrarese, L., Ford, H. C., Huchra, J., et al. 2000, ApJS, 128, 431

Springer)

de Vaucouleurs, G., de Vaucouleurs, A., Corwin, H. G., Jr., et al. 1991, Third

Egusa, F., Kohno, K., Sofue, Y., Nakanishi, H., & Komugi, S. 2009, ApJ,

Fernandes, I. F., Gruenwald, R., & Viegas, S. M. 2005, MNRAS, 364, 674

Reference Catalogue of Bright Galaxies Vol. I, II, & III (New York:

```
1997, ApJ, 489, 63
Groh, J. H., Ekström, S., Georgy, C., et al. 2019, A&A, 627, 24
Hägele, G. F., Pérez-Montero, E., Díaz, Á I., Terlevich, E., & Terlevich, R.
  2006, MNRAS, 372, 293
Heger, A., Fryer, C. L., Woosley, S. E., Langer, N., & Hartmann, D. H. 2003,
    mJ. 591, 288
Henry, R. B. C., Edmunds, M. G., & Köppen, J. 2000, ApJ, 541, 660
Henry, R. B. C., Nava, A., & Prochaska, J. X. 2006, ApJ, 647, 984
Ho, I.-T., Kudritzki, R.-P., Kewley, L. J., et al. 2015, MNRAS, 448, 2030
Ho, I. T., Meidt, S. E., Kudritzki, R.-P., et al. 2018, A&A, 618, A64
Ho, I.-T., Seibert, M., Meidt, S. E., et al. 2017, ApJ, 846, 39
Hummer, D. G., & Storey, P. J. 1987, MNRAS, 224, 801
Jang, I. S., & Lee, M. G. 2017, ApJ, 836, 74
Jarrett, T. H., Masci, F., Tsai, C. W., et al. 2013, AJ, 145, 6
Jiménez-Donaire, M. J., Cormier, D., Bigiel, F., et al. 2017, ApJL, 836, L29
Kelly, B. C. 2007, ApJ, 665, 1489
Kennicutt, R. C., Jr., Armus, L., Bendo, G., et al. 2003a, PASP, 115, 928
Kennicutt, R. C., Jr., Bresolin, F., & Garnett, D. R. 2003b, ApJ, 591, 801
Kewley, L. J., & Ellison, S. L. 2008, ApJ, 681, 1183
Kreckel, K., Faesi, C., Kruijssen, J. M. D., et al. 2018, ApJL, 863, L21
Krumholz, M. R., & Ting, Y.-S. 2018, MNRAS, 475, 2236
Leroy, A. K., Sandstrom, K. M., Lang, D., et al. 2019, ApJS, 244, 24
Leroy, A. K., Walter, F., Bigiel, F., et al. 2009, AJ, 137, 4670
Leroy, A. K., Walter, F., Sandstrom, K., et al. 2013, AJ, 146, 19
Liu, X.-W., Luo, S.-G., Barlow, M. J., Danziger, I. J., & Storey, P. J. 2001,
           327, 141
Luridiana, V., Morisset, C., & Shaw, R. A. 2012, in IAU Symp. 283, Planetary
  Nebulae: An Eye to the Future, ed. M. T. V. T. Lago (Cambridge:
  Cambridge Univ. Press), 422
Luridiana, V., Morisset, C., & Shaw, R. A. 2015, A&A, 573, A42
Maiolino, R., & Mannucci, F. 2019, A&ARv, 27, 3
Mannucci, F., Cresci, G., Maiolino, R., Marconi, A., & Gnerucci, A. 2010,
          5, 408, 2115
McCall, M. L. 1982, PhD thesis, The Univ. Texas
McQuinn, K. B. W., Skillman, E. D., Dolphin, A. E., Berg, D., & Kennicutt, R.
   2017, AJ, 154, 51
Moustakas, J., Kennicutt, R. C. J., Tremonti, C. A., et al. 2010, ApJS, 190, 233
Muñoz-Mateos, J. C., Gil de Paz, A., Zamorano, J., et al. 2009, ApJ, 703, 1569
Nava, A., Casebeer, D., Henry, R. B. C., & Jevremovic, D. 2006, ApJ,
Nicholls, D. C., Sutherland, R. S., Dopita, M. A., Kewley, L. J., &
  Groves, B. A. 2017, MNRAS, 466, 4403
Oke, J. B. 1990, AJ, 99, 1621
Pagel, B. E. J., & Edmunds, M. G. 1981, ARA&A, 19, 77
Peimbert, A., & Peimbert, M. 2010, ApJ, 724, 791
Peimbert, M. 1967, ApJ, 150, 825
Peimbert, M., & Costero, R. 1969, BOTT, 5, 3
Peimbert, M., Torres-Peimbert, S., & Ruiz, M. T. 1992, RMxAA, 24, 155
```

```
Peña-Guerrero, M. A., Peimbert, A., & Peimbert, M. 2012, ApJL, 756, L14
Pérez-Montero, E., Díaz, A. I., Vílchez, J. M., & Kehrig, C. 2006, A&A,
   449, 193
Phillipps, S., & Edmunds, M. G. 1991, MNRAS, 251, 84
Pilyugin, L. S. 1999, A&A, 346, 428
Pilyugin, L. S., Grebel, E. K., Zinchenko, I. A., Nefedyev, Y. A., &
   Vílchez, J. M. 2019, A&A, 623, A122
Pilyugin, L. S., Mattsson, L., Vílchez, J. M., & Cedrés, B. 2009, MNRAS,
   398, 485
Pipino, A., & Matteucci, F. 2009, in IAU Symp. 258, The Ages of Stars, ed.
   E. E. Mamajek, D. R. Soderblom, & R. F. G. Wyse (Cambridge: Cambridge
  Univ. Press), 39
Pogge, R. W., Atwood, B., Brewer, D. F., et al. 2010, Proc. SPIE, 7735,
   77350A
Querejeta, M., Meidt, S. E., Schinnerer, E., et al. 2015, ApJS, 219, 5
Rigby, J. R., Bayliss, M. B., Gladders, M. D., et al. 2015, ApJL, 814, L6
Rosales-Ortega, F. F., Kennicutt, R. C., Sánchez, S. F., et al. 2010, MNRAS,
   405, 735
Rosales-Ortega, F. F., Sánchez, S. F., Iglesias-Páramo, J., et al. 2012, ApJL,
   756, L31
Rosolowsky, E., & Simon, J. D. 2008, ApJ, 675, 1213
Rubin, R. H. 1986, ApJ, 309, 334
Ryder, S. D. 1995, ApJ, 444, 610
```

```
Saintonge, A., Catinella, B., Tacconi, L. J., et al. 2017, ApJS, 233, 22
Sánchez, S. F., Kennicutt, R. C., Gil de Paz, A., et al. 2012, A&A, 538, A8
Sánchez, S. F., Rosales-Ortega, F. F., Iglesias-Páramo, J., et al. 2014, A&A,
  563, A49
Sánchez-Menguiano, L., Sánchez, S. F., Pérez, I., et al. 2016, A&A, 587,
Sánchez-Menguiano, L., Sánchez, S. F., Pérez, I., et al. 2018, A&A, 609, A119
Shapley, A. E., Reddy, N. A., Kriek, M., et al. 2015, ApJ, 801, 88
Sheth, K., Regan, M., Hinz, J. L., et al. 2010, PASP, 122, 1397
Shostak, G. S., & van der Kruit, P. C. 1984, A&A, 132, 20
Steidel, C. C., Rudie, G. C., Strom, A. L., et al. 2014, ApJ, 795, 165
Thuan, T. X., Izotov, Y. I., & Lipovetsky, V. A. 1995, ApJ, 445, 108
Torres-Peimbert, S., & Peimbert, M. 1977, RMxAA, 2, 181
Tremonti, C. A., Heckman, T. M., Kauffmann, G., et al. 2004, ApJ, 613, 898
Van Dyk, S. D., Li, W., & Filippenko, A. V. 2006, PASP, 118, 351
van Zee, L., & Haynes, M. 2006, ApJ, 636, 214
Vila-Costas, M. B., & Edmunds, M. G. 1993, MNRAS, 265, 199
Vincenzo, F., & Kobayashi, C. 2018, MNRAS, 478, 155
Walter, F., Brinks, E., de Blok, W. J. G., et al. 2008, AJ, 136, 2653
Woosley, S. E., & Weaver, T. A. 1995, ApJS, 101, 181
Yates, R. M., Schady, P., Chen, T.-W., Schweyer, T., & Wiseman, P. 2020,
  A&A, 634, A107
Zaritsky, D., Kennicutt, J. C. R., & Huchra, J. 1994, ApJ, 420, 87
```